Chapter IV. Mixed fluid sources in the Alberta Rocky Mountain foreland fold-thrust belt: Insights from stable isotopic studies of dated, fault-hosted clay minerals

Abstract

The source and pathways of fluids are key to the physical and chemical properties of deforming fold-thrust belts, but are challenging to constrain. Many previous fluid studies in the Canadian Cordillera have focused on quartz and/or carbonate veins and their associated fluid inclusions. This study expands the fluid proxy record through stable isotopic analyses of authigenic fault-grown illite in the Rocky Mountain foreland fold-thrust belt in Alberta. Clay hydrogen isotopic values (δD) range from –17.8 to -117.6 ± 2‰ (SMOW), with associated mineralizing fluids interpreted to range from ~-50 to -124‰ with one outlier of ~-5‰. $\delta^{18}O$ values of illite range from 7.0 to 20.3 ± 0.2‰, which corresponds to fluid values of ~-2.5 to 10.7‰. This wide range of fluid values is indicative of a spatially and temporally heterogeneous fluid history in the Rocky Mountain foreland fold-thrust belt. Fluid compositions indicate the mixing of two primary fluid sources, high latitude meteoric fluids and deeply-sourced metamorphic fluids.

Introduction

It is well known that fluids are present in active fault zones and that they play a fundamental role in faulting through both mechanical and chemical interplay with the host rocks. The pressure state of fluid, hydrostatic vs. lithostatic, has important implications regarding the dynamic evolution of the deforming crust. Fluids at lithostatic or near lithostatic pressures significantly reduce normal stress on faults, promoting slip. In order to exist at high pressures, fluids must be isolated from surface reservoirs and/or episodically expelled from reservoirs at depth. Fluids at or near hydrostatic pressure, in contrast, are in communication with the surface hydrosphere, involving the downward infiltration of surface fluids to the lower reaches of the upper crust, at least as far down to the frictional-plastic transition. Fault zones are conduits for fluids that are driven by gradients in pressure and temperature at depth, allowing the transport of heat and mass through the deforming upper crust. Migrating fluids interact chemically with the rock and commonly precipitate clay minerals at low temperature/pressure (sub-greenschist facies) conditions (Vrolijk and van der Pluijm, 1999; Haines and van der Pluijm, 2012), thus enabling us to characterize and identify the sources of fluids in regions and structural elements of contractional systems.

The main sources of fluids in contractional mountain belts are, (1) the downward infiltration of meteoric and surface-sourced fluids and (2) the expulsion of metamorphic fluids produced during prograde dehydration reactions (e.g. Walther and Wood, 1984; Fyfe and Kerrich, 1985; Bradbury and Woodwell, 1987; Ge and Garven, 1989; Koons and Craw, 1991; Dworkin, 1999; Menzies et al., 2014; Hüpers et al, 2017). Hydrocarbon maturation has also been proposed as a fluid-generating, deformation-mediating process (Mackay, 2015). Several studies have attempted to quantify the fluid volume from end-member sources throughout the protracted history of an orogenic belt (e.g. Travé et al., 2007; Cooley et al., 2011; Fitz-Diaz et al., 2014; Menzies et al., 2016). The majority of these studies have focused on the chemical and isotopic studies of quartz and carbonate veins, and their associated fluid inclusions (e.g. Evans and Battles, 1999; Bebout et al., 2001; Kirschner and Kennedy, 2001; Anastasio et al., 2004; Rygel et al., 2006; Travé et al., 2007; Cooley et al., 2011; Evans et al., 2012). Only a small number of studies have examined secondary clay mineral genesis along fault zones (Fitz-Diaz et al., 2014; Boles et al., 2015; Lynch and van der Pluijm. 2016), reflecting the challenges of fine-grained mineral characterization and quantification. The power of vein and fluid inclusion studies are many; for example, several chemical proxies can be measured from a single mineral or mineral system, and precipitation temperatures can be constrained from fluid inclusion analysis. A major advantage of studying clay minerals, however, is that newly grown illite can also be radiogenically dated. Additionally, the abundance of hydrogen bound within clay minerals is less likely to buffer with the oxygen-rich mineral populations of which the crust is comprised. Thus, this study will examine stable isotopic characterization of clay minerals in combination with previously published fault ages from the Canadian Cordillera in Alberta (see van der Pluijm et al., 2001, van der Pluijm et al, 2006, and Pană and van der Pluijm, 2015 for details regarding Canadian Cordilleran fault gouge dating).

The Canadian fold-thrust belt is an ideal location to test the hypotheses surrounding the sources of orogenic fluid input. At high latitudes, surface-derived meteoric waters are extremely isotopically light and are, therefore, distinguished from other geologic fluids by their markedly negative hydrogen (δD) and oxygen ($\delta^{18}O$) isotopic values. In addition, basinal brines in the Canadian foreland are well characterized as the result of extensive hydrocarbon exploration. Therefore, if surface-derived fluids dominate the fold-thrust system, we expect very low δ-values for both oxygen and hydrogen. Instead, with input from metamorphic and/or magmatic sources, we expect higher δ-values for both hydrogen and oxygen. If seawater/connate water dominates the system, we expect high δD values and low $\delta^{18}O$ values. This study uses both the δD and $\delta^{18}O$ values of fault-hosted authigenic illite of the Canadian fold-thrust belt in Alberta to identify the source(s) of Late Jurassic- to Early Eocene-aged, fault-channelized fluid flow.

Sample Locations and Mineralogy

Fifteen (15) samples analyzed in this study were collected from the Alberta Rocky Mountain foreland fold-thrust belt, spanning the width of the belt from approximately 50 to 54 °N latitude (Figure IV.1). Twelve (12) samples of fault gouge and one (1) footwall shale sample were previously dated using Ar geochronology (Pană and van der Pluijm, 2015); two (2) additional fault gouge ages were reported by van der Pluijm (2006). Using the combined illite ages from both studies, Pană and van der Pluijm (2015) identified four major pulses of contractional deformation between the Late Jurassic and Early Eocene, which preceded middle to late Eocene extensional collapse of the orogen. Authigenic illite shows that the growth of fault-related clay minerals occurred in the presence of ancient orogenic fluids, so their stable isotopic makeup reflects the stable isotopic composition of the syndeformational fluids. Though earlier work determined the polytypes of *illite* present in each gouge sample (required for Ar/Ar-dating), additional work was needed to fully characterize the clay mineralogy in order to extract the relevant isotopic signatures from authigenic illite.

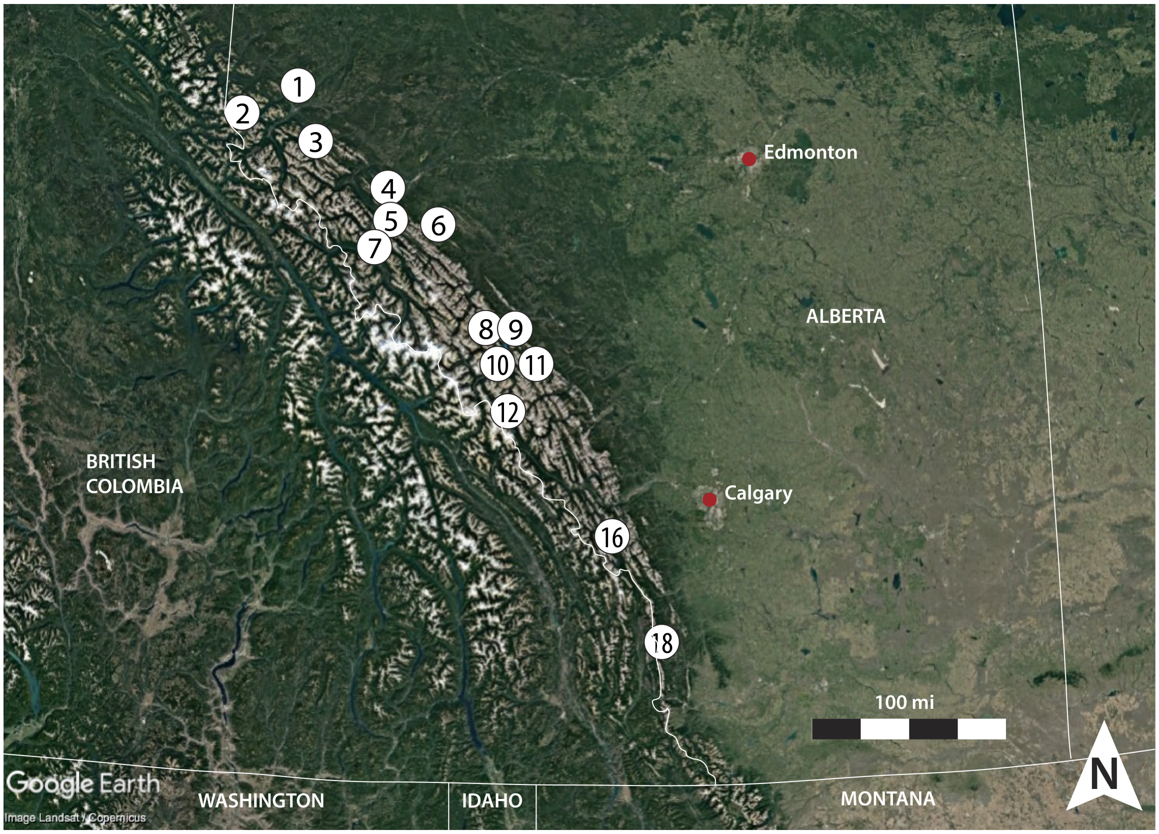

Figure IV.1: The locations of 15 samples collected from the Canadian Cordillera fold-thrust belt in Alberta are shown in this Google Earth image. Sample A (a footwall shale sample) shares the same location (within 300 m) as Sample 9.

The methods to process and characterize illitic materials are described in van der Pluijm et al. (2006) and Pană and van der Pluijm (2015). We completed additional clay mineral x-ray diffraction (XRD) characterization through low-angle (2-40 °2θ) scanning of oriented mounts, which were prepared using the suspension method (Moore and Reynolds, 1997). We used a Cu-source Rigaku Ultima IV X-Ray Diffractometer equipped with a Ni foil k-beta filter, scanning at a speed of 1°/minute and a step size of 0.02 °2θ. Though illite was the dominant clay mineralogy for all samples, we also identified the presence of minor quartz, calcite, kaolinite, and chlorite in some of the samples (Figure IV.2). DP10-1 also contained a trace amount of gypsum. Using the mineral reference intensities (MRI) method (Moore and Reynolds, 1997), we approximate the proportions of clay minerals present in each sample. Table IV.1 summarizes the results of mineral characterization.

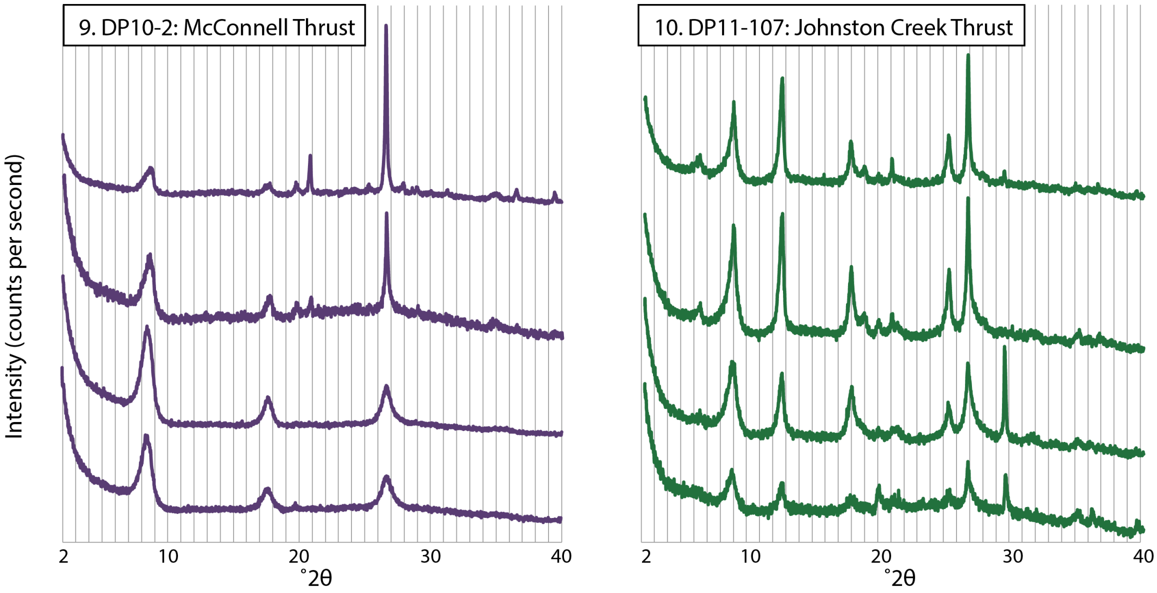

Figure IV.2: Two representative series of oriented XRD patterns. In both diagrams, the coarse fraction is on the top, the fine fraction on the bottom. The left pattern (DP10-2) is representative of the several samples whose clay mineralogy contain only illite. The right pattern (DP11-107) is more representative of the samples that have two clay minerals present, in this case, illite and chlorite. Both samples also indicate the presence of quartz, particularly in the coarser fractions (peaks at 20.8 and 26.5°2θ). The right sample also shows evidence of calcite, present in the two finer fractions (peak at 29.4 °2θ).

Table IV.1: Clay composition of samples

		MRI Quantification			Illite Polytype*			
Sample ID	Size Fraction	%Chl	%Kaol	%Ill	%2M_1	%1M_d	%1M_d/clay	non-clay minerals
1. DP10-406C	C	-	37	63	21	79	**50**	qtz
Muskeg Thrust	MC	-	23	77	16	84	**35**	qtz
	M	-	4	96	10	90	**14**	qtz
	F	-	-	100	6	94	**6**	-
2. DP11-90	C	-	10	90	19	81	**27**	qtz
Broadview (Snake Indian) Thrust	MC	-	5	95	14	86	**18**	?
	M	-	-	100	9	91	**9**	cct
	F	-	-	100	5	95	**5**	cct
3. DP11-100	C	-	-	100	36	64	**36**	qtz, cct
Rocky Pass Thrust	MC	-	-	100	26	74	**26**	cct
	M	-	-	100	17	83	**17**	cct
	F	-	-	100	13	87	**13**	cct
4. DP10-166D	C	-	-	100	24	76	**24**	qtz
Brule Thrust	MC	-	-	100	18	82	**18**	qtz
	M	-	-	100	11	89	**11**	-
	F	-	-	100	6	94	**6**	-
5. DP10-140A	C	-	-	100	32	68	**68**	qtz
Greenock Thrust	MC	-	-	100	30	70	**70**	qtz(tr)
	M	-	-	100	9	91	**91**	-
	F	-	-	100	2	98	**98**	-
6. DP10-11	C**	?	?	?	38	62	**62****	?
Nikanassin Thrust	MC***	?	?	?	19	81	**81*****	?
	M	-	-	100	11	89	**89**	-
	F	-	-	100	6	94	**94**	-
7. DP10-1	C	-	-	100	28	72	**7**	qtz
Pyramid Thrust (Jasper)	M	-	-	100	16	84	**84**	qtz
	F	-	-	100	11	89	**89**	qtz, gyp
8. DP11-104	C	23	-	77	42	58	**55**	qtz, cct
Sulphur Mt. Thrust (Abraham Lake)	MC	17	-	83	29	71	**41**	qtz, cct
	M	5	-	95	11	89	**15**	cct
	F	-	-	100	7	93	**7**	cct(tr)
9. DP10-2	C	-	-	100	20	80	**80**	qtz
McConnell Thrust (Abraham Lake)	MC	-	-	100	16	84	**84**	qtz
	M	-	-	100	8	92	**92**	-
	F	-	-	100	6	94	**94**	-
10. DP11-107	C	29	-	71	41	59	**58**	qtz
Johnston Creek Thrust	MC	24	-	76	31	69	**48**	qtz
	M	14	-	86	22	78	**33**	cct
	F	18	-	82	11	89	**27**	cct
11. DP11-114	C	-	-	100	32	68	**68**	qtz
Clearwater Thrust	MC	-	-	100	18	82	**82**	qtz
	M	-	-	100	11	89	**89**	-
	F	-	-	100	8	92	**92**	-
12. DP11-112	C	12	-	88	52	48	**58**	qtz
Simpson Pass Thrust	MC	7	-	93	33	67	**38**	-
	M	6	-	94	11	89	**16**	-
	F	-	-	100	7	93	**7**	cct

Table IV.1: Clay composition of samples (cont.)

		MRI Quantification			Illite Polytype*			
Sample ID	Size Fraction	%Chl	%Kaol	%Ill	%2M$_1$	%1M$_d$	%1M$_d$/clay	non-clay minerals
16. KKF-91-1A								
Sulphur Mt. Thrust (Kananaskis)	C	-	-	100	30	70	**70**	qtz
	M	-	-	100	5	95	**95**	-
	F	-	-	100	5	95	**95**	-
18. KKF-102E	C	-	57	43	73	27	**12**	qtz
Lewis Thrust (Gould Dome)	M	-	30	70	39	61	**43**	-
	F	-	5	95	18	82	**78**	-
A. MTF-FW2	C	-	-	100	32	68	**68**	qtz
McConnell Footwall Shale	M	-	-	100	8	92	**92**	-
	F	-	-	100	6	94	**94**	-

* From Pană and van der Pluijm (2015)
**No oriented sample available
***Clay minerals not identifiable in oriented samples
(tr) - trace

Stable Isotopic Characteristics of Clay Gouge

Isotopic measurement

Stable isotopic measurements of both hydrogen and oxygen were completed at the Institute of Earth Surface Dynamics (IDYST) at the University of Lausanne (UNIL). Approximately 1.5–2mg of sample separates were encapsulated in duplicate into silver foil packets and kept under vacuum for at least 12 hours prior to analysis. Samples were then quickly transferred to a helium-flushed zero-blank autosampler connected to a Thermo Finnigan Delta Plus XL thermochemical elemental analyzer (TC/EA). A helium carrier gas transferred the reduced hydrogen gas to a the mass spectrometer, which measured the ratios of H_2 and DH gases as well as the weight percent water for each sample. Results are reported using δ-notation relative to standard mean ocean water (SMOW) and are reproducible to ±3‰.

Oxygen gas was isolated from silicate samples for isotopic measurements using laser fluorination (e.g., Sharp, 1990). Prior to oxygen analyses, samples were loaded onto a platinum sample plate and heated in an oven at 150°C for at least 12 hours. Samples were introduced onto the laser fluorination line and pumped to a vacuum of approximately 10^{-6} mbar prior to fluorination. Extracted oxygen gas was collected on a zeolite molecular sieve and transferred to a Finnigan MAT 253 Mass Spectrometer for measurement. As with hydrogen, results are reported using δ-notation relative to standard mean ocean water (SMOW) and are reproducible to ±0.2‰. We were unable to measure one sample (16: KKF-91-1A) for oxygen isotopic composition due to its reaction with F_2 gas at room temperature, and thus it's unmeasurable oxygen loss during the pre-fluorination stages of the oxygen extraction procedure. This passive fluorination is not uncommon in very fine-grained, low-temperature clay minerals (Kirshner and Sharp, 1997).

Hydrogen Isotope Results

Two aliquots of each sample size fraction were measured for hydrogen isotopic composition. The results of each measurement and duplicate are summarized in Table IV.2. In nearly all cases, measurements are reproducible to ≤3‰ (excluding samples 6: DP10-11F, 9: DP10-2MC, and 12: DP11-112MC); the maximum error on duplicate measurements is 3.7‰ (sample 12: DP11-112MC). Internal lab standards of kaolinite and biotite have a reproducibility better than 2‰.

Table IV.2: Hydrogen isotopic results

Sample ID	Size Fraction	δD (‰)	dupl. (‰)	Sample ID	Size Fraction	δD (‰)	dupl. (‰)
1. DP10-406C	C	-83.5	-84.1	**8. DP11-104**	C	-101.7	-101.7
Muskeg Thrust	MC	-74.6	-75.6	*Sulphur Mt. Thrust (Abraham Lake)*	MC	-100.1	-100.3
	M	-94.4	-96.4		M	-86.8	-86.9
	F	-101.9	-101.0		F	-73.8	-73.9
2. DP11-90	C	-71.1	-72.7	**9. DP10-2**	C	-110.7	-111.8
Broadview (Snake Indian) Thrust	MC	-69.2	-71.1	*McConnell Thrust (Abraham Lake)*	MC	-107.6	-110.8
	M	-64	-65.6		M	-92.5	-90.6
	F	-66.4	-65.8		F	-89.4	-87.6
3. DP11-100	C	-121.4	120.5	**10. DP11-107**	C	-80.4	-79.5
Rocky Pass Thrust	MC	-118.8	-118.3	*Johnston Creek Thrust*	MC	-95.0	-94.8
	M	-102.0	-101.6		M	-97.2	-96.4
	F	-95.8	-97.0		F	-89.5	-89.0
4. DP10-166D	C	-73.6	-73.9	**11. DP11-114**	C	-116.8	-118.2
Brule Thrust	MC	-98.8	-98.1	*Clearwater Thrust*	MC	-125.9	-125.0
	M	-97.3	-97.4		M	-118.9	-116.6
	F	-42.6	-44.6		F	-108.0	-108.3
5. DP10-140A	C	-94.2	-95.0	**12. DP11-112**	C	-115.5	-114.1
Greenock Thrust	MC	-98.2	-95.6	*Simpson Pass Thrust*	MC	-112.9	-115.0
	M	-102.6	-102.4		M	-120.4	-116.7
	F	-78.4	-78.5		F	-98.2	-96.0
6. DP10-11	C	-112.2	-114.7	**16. KKF-91-1A**			
Nikanassin Thrust	MC	-114.9	-115.1	*Sulphur Mt. Thrust (Kananaskis)*	C	-119.1	-120.4
	M	-104.4	-103.9		M	-106.5	-107.1
	F	-107.0	-103.9		F	-116.3	-116.1
7. DP10-1	C	-105.7	-105.5	**18. KKF-102E**	C	-127.9	-129.8
Pyramid Thrust (Jasper)	M	-81.9	-81.8	*Lewis Thrust (Gould Dome)*	M	-124.3	-124.0
	F	-49.2	-51.1		F	-115.9	-114.1
				A. MTF-FW2	C	-117.2	-118.5
				McConnell Footwall Shale	M	-95.2	-95.4
					F	-102.7	-100.8

A York-style bivariate linear regression analyses of hydrogen isotopic compositions and authigenic ($1M_d$) illite quantifications allows the extrapolation to 100% authigenic material, and, therefore, the determination of the hydrogen isotopic composition of the end-member, deformation-related illite component of the gouge (Table IV.3) (York, 1968; Boles et al., 2015; Lynch and van der Pluijm, 2016). In one case (sample 4: DP10-166D, Brule Thrust), regression was unsuccessful, and produced errors much too large to allow for meaningful interpretation. We attribute this error to an erroneously high δD value in the finest fraction, in which organic material was concentrated by centrifugation during sample preparation. Discarding the finest fraction, we completed a regression with only the coarsest three fractions, yielding a value of -136.5 ± 22.4‰. These and other results are listed in Table IV.3 and their distributions are shown in Figure IV.3.

Table IV.3: Interpreted isotopic composition of authigenic illite

Sample ID	Fault/Description	$\delta D_{authigenic}$	δO_{fine} (±2‰)
1. DP10-406C	*Muskeg Thrust*	-105.7 ± 2.9‰	12.0‰
2. DP11-90	*Broadview (Snake Indian) Thrust*	-63.1 ± 2.0‰	19.3‰
3. DP11-100	*Rocky Pass Thrust*	-80.8 ± 6.8‰	20.3‰
4. DP10-166D	*Brule Thrust*	35.4 ± 72.1‰* -136.5 ± 22.4‰**	14.6‰
5. DP10-140A	*Greenock Thrust*	-71.9 ± 7.3‰	17.1‰
6. DP10-11	*Nikanassin Thrust*	-102.1 ± 2.3‰	14.6‰
7. DP10-1	*Pyramid Thrust (Jasper)*	-17.8 ± 19.9‰	9.4‰
8. DP11-104	*Sulphur Mt. Thrust (Abraham Lake)*	-73.1 ± 2.4‰	16.5‰
9. DP10-2	*McConnell Thrust (Abraham Lake)*	-77.3 ± 8.1‰	11.4‰
10. DP11-107	*Johnston Creek Thrust*	-117.6 ± 8.6‰	11.6‰
11. DP11-114	*Clearwater Thrust*	-96.5 ± 11.7‰	10.7‰
12. DP11-112	*Simpson Pass Thrust*	-96.9 ± 4.3‰	7.0‰
16. KKF-91-1A	*Sulphur Mt. Thrust (Kananaskis)*	-107.7 ± 2.5‰	--
18. KKF-102E	*Lewis Thrust (Gould Dome)*	-110.8 ± 2.1‰	8.3‰, 8.1‰
A. MTF-FW2	*McConnell Footwall Shale*	-92.1 ± 3.3‰	13.5‰, 13.3‰

*Using all size fractions
**Without fine fraction

Oxygen Isotope Results

Oxygen measurements were completed only for the finest fraction of each sample site. Unlike hydrogen, oxygen isotopic values are not affected by the presence of hydrocarbons that can be concentrated into the finer fractions. Instead, oxygen isotopic values are affected by the presence of other rock-forming minerals, including silicates, oxides, and carbonates. Non-clay silicate minerals are not present in any of the finest fractions, except trace amounts of quartz and gypsum in sample 7 (DP10-1). Minor (<5 wt%) calcite was removed prior to oxygen isotopic analysis by reaction with dilute HCl. Oxides are not present in any of the samples. The results of the oxygen isotopic analyses are summarized along with the hydrogen isotopic measurements in Table IV.3 and Figure IV.3.

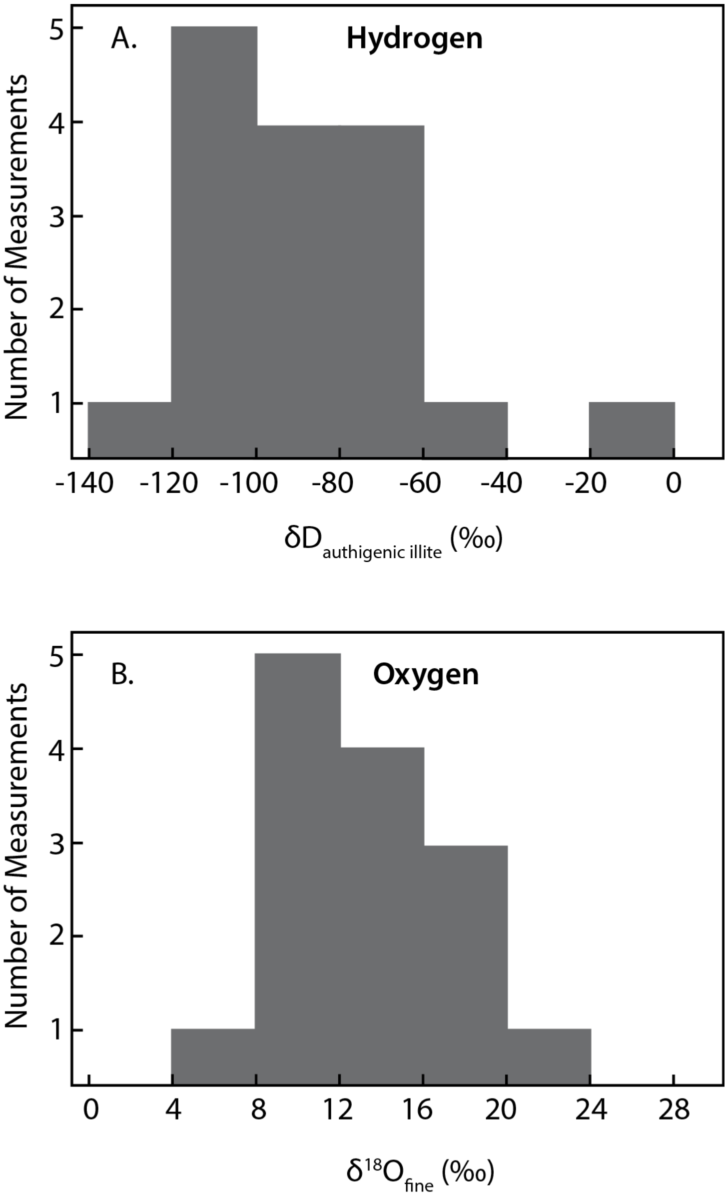

Figure IV.3: Histograms of (A) hydrogen and (B) oxygen isotopic composition of authigenic illite in δD‰ and $\delta^{18}O$‰ (permil) relative to SMOW.

Analysis and Interpretations

Fractionation Temperature Constraints

With constraints on fractionation temperature, the isotopic composition of mineralizing fluids can be calculated from the isotopic composition of fine illitic clay gouge material. Minimum fractionation temperature estimates are constrained by the minimum formation temperature of illite, ~90°C (Haines et al., 2012). Maximum fractionation temperature estimates are obtained from various lines of geologic evidence. A geothermal gradient of ~20-25°C/km has been estimated for the Canadian Rocky Mountain foreland fold-thrust belt region (e.g. England and Bustin, 1986; Hardebol et al., 2009; Osadetz et al., 2004). With a maximum thickness of ~8km for the deformed foreland wedge (Price, 1981; Pană and Elgr, 2013), this equates to temperatures less than about 160-200°C, though it is likely that much of the thrusting occurred at shallower depths. In the Lewis thrust sheet, this estimate is supported by zircon fission track ages that pre-date compressional deformation even in the deepest structural parts of the belt, confirming that temperatures in the thrust sheet did not rise above the annealing temperature of 230°C either during or after deformation (Feinstein et al., 2007). Additionally, paleomagnetic studies of the fold-thrust belt suggest that temperatures did not rise above ~250°C (Enkin et al., 2000). Using Apatite Fission Track thermochronometry, Osadetz et al. (2004) also noted a decrease in the regional geothermal gradient in the Lewis thrust sheet that they attributed to the downward infiltration of meteoric fluids into the thrust sheet. Nesbitt and Muehlenbachs (1994) recorded fluid inclusion homogenization temperatures in calcite veins of 120° to 200°C. These observations, along with maximum temperature estimates from organic maturity indicators (Kalkreuth and McMechan, 1984; England and Bustin, 1986; Hardebol et al, 2009) and conodont alteration indices (Symons and Cioppa, 2002) characterize the thermal history of the fold thrust belt and suggest that the viable temperature range of illite formation was 100° - 200°C, with a likely formation temperature around 150°C for thrusting at approximately 5-6 kilometers in depth.

We calculate the composition of the fluid isotopic values for 150 ± 50°C temperatures for each sample (Table IV.4, Figure IV.4). The results show that the mineralizing fluids largely overlap with Alberta Basin fluids (Hitchon and Friedman, 1969; Connolly et al., 1990), regardless of the precise fractionation temperatures. On the higher end of the temperature range, fluids have slightly more positive $\delta^{18}O$ values and more negative δD values. This would imply more water-rock interaction and oxygen buffering (smaller water/rock ratio and/or longer fluid travel pathways through the fold thrust belt); however, the very negative δD values still require a high latitude or high elevation meteoric fluid as the original source (Nesbitt and Muehlenbachs, 1989). One sample (DP10-1) yields a fluid composition that very closely resembles the isotopic composition of seawater.

Characteristics and Identity of Mineralizing Fluids

The range of isotopic values of mineralizing fluids indicates a heterogeneous fluid regime across and along the fold-thrust belt. Results show no systematic temporal or spatial trends in the stable isotopic composition of fault rocks, indicating that fluid regimes and flow pathways were variable both through time and along strike of the mountain belt. The fluids with the lowest δD and $\delta^{18}O$ values

Table IV.4: Fluid isotopic values

	Hydrogen (δD)			Oxygen (δ^{18}O)		
Sample ID	100°C	**150°C**	200°C	100°C	**150°C**	200°C
1. DP10-406C	-79	**-93**	-105	-1.5	**2.4**	5.1
2. DP11-90	-36	**-51**	-62	5.9	**9.7**	12.4
3. DP11-100	-51	**-68**	-80	6.9	**10.7**	13.4
4. DP10-166D	-110	**-124**	-135	1.2	**5.0**	7.7
5. DP10-140A	-45	**-60**	-71	3.7	**7.5**	10.2
6. DP10-11	-75	**-90**	-101	1.2	**5.0**	7.7
7. DP10-1	9	**-5**	-17	-4.0	**-0.2**	2.5
8. DP11-104	-46	**-61**	-72	3.1	**6.9**	9.6
9. DP10-2	-51	**-65**	-76	-2.0	**1.8**	4.5
10. DP11-107	-91	**-105**	-117	-1.9	**2.0**	4.6
11. DP11-114	-70	**-84**	-95	-2.7	**1.1**	3.4
12. DP11-112	-70	**-85**	-96	-6.4	**-2.6**	0.1
16. KKF-91-1A	-81	**-95**	-107	-	**-**	-
18. KKF-102E	-84	**-98**	-110	-5.1, -5.3	**-1.4, -1.5**	1.4, 1.2
A. MTF-FW2	-67	**-81**	-92	0.1, -0.1	**3.9, 3.7**	6.7, 6.4

strongly resemble variably-evolved, surface-sourced (meteorically-charged) basin fluids, whereas the fluids higher δD and δ^{18}O values indicate input from deeper metamorphic fluids, or in the case of sample 7 (Pyramid Fault) connate seawater (Figure IV.4). Excluding the Pyramid Fault sample from the following discussion, we use the calculated fluid δ values to make a prediction regarding the isotopic composition of the regional meteoric water. Given a fractionation temperature of 150°C ± 50 °C, we calculate the isotopic composition of orogenic fluids for each sample. Next we determine the linear best fit for those values and extrapolate to its intersection with the global meteoric water line at -19.1 (+4.5/-3.5)‰ δ^{18}O, -143 (+36/-28) ‰ δD (Figure IV.5). The projected isotopic composition is then compared to both present-day and deformation-aged surface fluids, which reportedly have about the same isotopic values (Longstaffe and Ayalon, 1990; Bowen and Revenaugh, 2003; Chamberlain et al., 2012). It is important to note that, since the illite was previously dated, we are confident that clays are tracking ancient fluid compositions and that they have not been reset by modern alteration. The correlation between the known isotopic composition of surface fluids and the projected end-member fluid composition from this study is strong evidence of the involvement of ancient surface fluids as one major fluid source in the fold-thrust belt. The other fluid end-member isotopic values fall within the range of metamorphic fluid composition (Sheppard, 1986) (Figure IV.5).

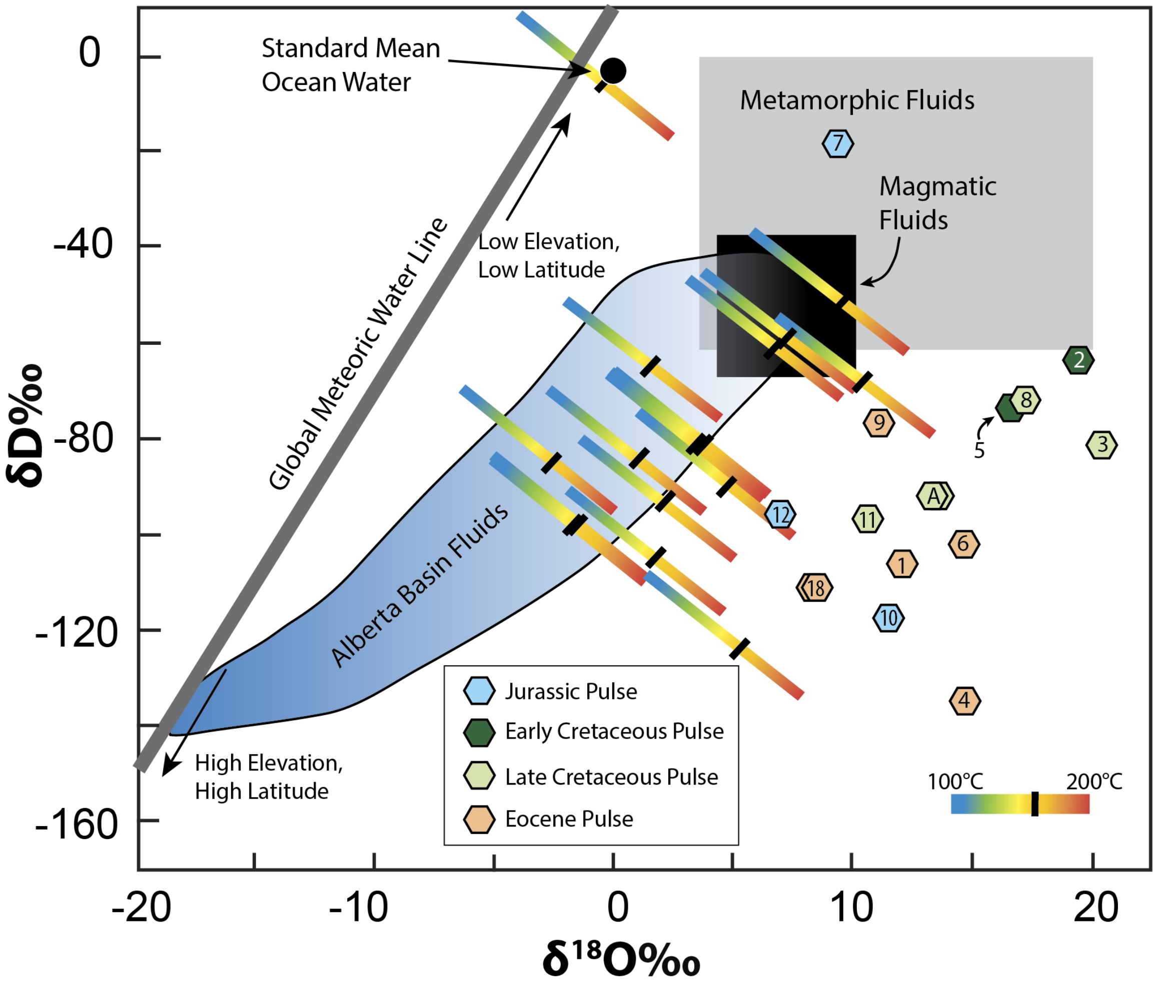

Figure IV.4: Plot of hydrogen and oxygen isotopic composition of major fluid reservoirs, authigenic illite composition, and calculated mineralizing fluid composition. Authigenic illite values are represented by hexagons, colored by illite age (Pană and van der Pluijm, 2015). Each illite measurement is paired with a rainbow colored bar representing the range of possible δD and δ^{18}O values over the 100° to 200°C fractionation temperature range, with a black tick mark representing the 150°C fractionation—cool colors represent low temperature end of the range, warm colors represent the high temperature end of the range. Major fluid reservoirs shown include metamorphic fluids (grey box), magmatic fluids (black box), Alberta basin fluids (blue shaded region), meteoric water (dark grey line) and standard mean ocean water (SMOW, black circle). Calculated fluid values largely overlap with basin fluids and partly with metamorphic/magmatic fluids. One fluid value corresponds with ocean water isotopic composition.

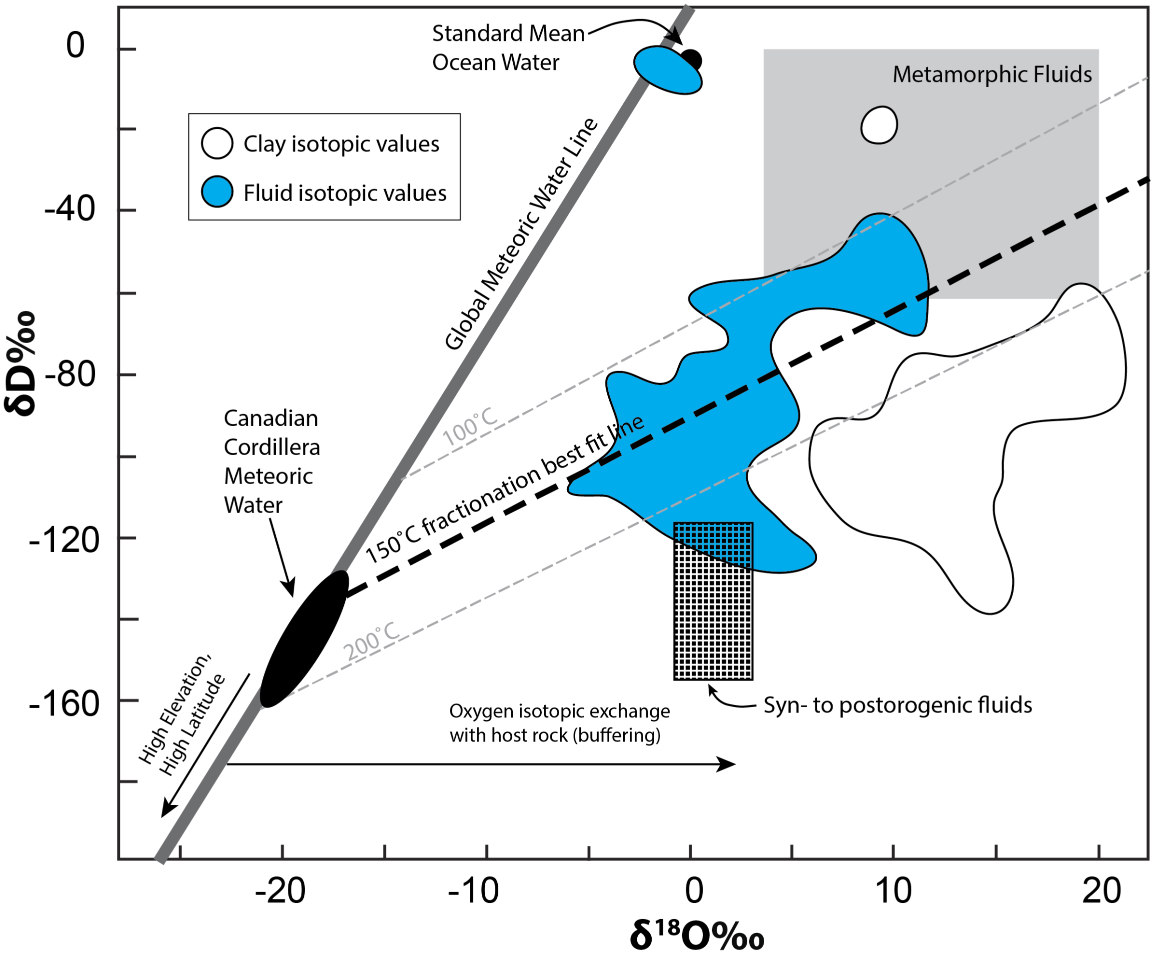

Figure IV.5: Schematic diagram showing the composition of end member mixed fluids. The range of isotopic composition of clays and the deformation fluids from which they formed are approximated by the white and blue shaded regions, respectively. The best-fit 150°C fractionation line is shown in a heavy black dash, ±50°C window is shown by grey dashed lines. This envelope overlaps with the δD and δ^{18}O values of Canadian Cordillera meteoric fluid (Longstaffe and Ayalon, 1990; Bowen and Revenaugh, 2003), which is shown as a black oval, and considered to be one of the end-member mixing fluids. The metamorphic fluids region is shown in grey (Sheppard, 1986) and is interpreted to be the other major end-member fluid. The textured grey box shows the region of syn- to postorogenic fluids (Nesbitt and Muehlenbachs, 1994) interpreted from fluids inclusions in dolomite veins, which have a slight overlap with clay mineralizing fluids, but have likely undergone extensive oxygen isotopic exchange with the host rocks at low water-rock ratios.

Previous studies identified the presence of migrating hot metamorphic fluids from hydrogen and oxygen stable isotopic composition, strontium isotope ratios in veins, and fluid inclusion chemistry and some suggest that they played a role in ore deposition in the Alberta foreland basins (Nesbitt and Muehlenbachs, 1989; Machel and Cavell, 1999; Cooley et al., 2011). Based on the hydrogen isotope composition of fluid inclusions and hydrous silicates in veins, which were as high as -20‰, Nesbitt and Muehlenbachs (1991) suggested that the majority of fluids involved in the Rocky Mountain thrusting originated as metamorphic devolatilization fluids. Considering the paired δD and $\delta^{18}O$ of each calculated fluid, most fall within the realm of mixing between the two sources—meteoric and metamorphic. However, several of the samples have more positive $\delta^{18}O$ values than would be expected based solely on mixing. This suggests a slight and variable degree of oxygen isotope exchange (buffering) with the host rocks. For this reason, we prefer to use δD values to quantify the proportions of meteoric and metamorphic fluids mixing during thrusting and deformation.

Using the end-member δD values of -20‰ ($\delta D_{metamorphic}$) and -143‰ ($\delta D_{meteoric}$), we calculate the total proportion of each fluid that mixed to create the fault-hosted fluids in this study. The average fluid δD value of -82.9‰ would have resulted from an approximately equal mixture of metamorphic and meteoric fluids (49%/51%). The minimum fluid value (δD = -125.1‰) would result from a mixture of 14% metamorphic and 86% meteoric fluids. The maximum (δD = -50.7‰) from a 75%/25% mixture of metamorphic and meteoric fluid. This range of values suggests that mixing of fluid is not constant through time and space, and that metamorphic fluids likely find preferential focused pathways of escape to the surface, rather than flowing homogeneously as planar flows along fault structures.

The calculated fluid value field also overlaps with the syn- to post-orogenic fluids reported by Nesbitt and Muehlenbachs (1994) from studies of fluid inclusions in dolomite veins. Fluid inclusion isotopic values closely resemble Canadian meteoric fluids in their hydrogen isotope composition, but were likely isotopically buffered in oxygen from fluid interaction in the Cambrian carbonate units that have $\delta^{18}O$ values of 17-22‰ (Nesbitt and Muehlenbachs, 1994). The fluid preserved in dolomite veins may have undergone extensive oxygen isotopic exchange with the host rocks due to low water-rock ratios (Bradbury and Woodwell, 1987; Nesbitt and Muehlenbachs, 1989; Machel et al., 1996; Kirshner and Kennedy, 2001). Unlike the fault zone fluids from our study, they do not seem strongly affected by input of metamorphic fluids, emphasizing the channelizing of deeply-sourced fluids along fault zones rather than through veins and deformation meshes (Sibson, 1996; Kirshner and Kennedy, 2001).

Conclusions and Summary

The study of dated clay gouges from the Canadian fold-thrust belt shows that gouge illite preserved the identity of mineralizing orogenic fluids. The major deformational fluids in the Canadian fold-thrust belt originate from a mixture of two main sources, (1) high-latitude surface fluids and (2) deeply-sourced metamorphic fluids in varying proportions across the belt. Oxygen isotopes suggest a minor degree of water-rock interaction and buffering. There is no obvious temporal or geographic control on geofluid composition within the belt. Rather, the spread of isotopic values suggests that fluid flow during deformation was heterogeneous, with metamorphic fluids likely localized along discrete structures at different times.

The robust isotopic memory of authigenic clays shown in this study shows that future work towards characterizing fault fluids using clay gouge has great potential for broad application. Improvement can be made by higher resolution analysis through increased sampling density and increased number of sample locations both along major structures and throughout the belt to better constrain the heterogeneities of fluid pathways and migration.

Acknowledgments

This project was supported by a Rackham Graduate School Predoctoral Fellowship to Lynch. Field and analytical support was provided by AER/Alberta Geological Survey. Additional support for clay research at the University of Michigan was provided by NSF. We would also like to thank Benita Putlitz for her invaluable help and guidance in the stable isotope laboratory at UNIL.

Chapter V. The identity of Alleghany deformation fluids from O-H isotopes and $^{40}Ar/^{39}Ar$-dating of authigenic clay minerals in the Central Appalachian Valley-and-Ridge Province

Abstract

Long-distance fluid migration from the Appalachian fold-thrust belt and Alleghany plateau has been long been hypothesized as the origin of the deposition of Mississippi Valley Type deposits and the remagnetization of sedimentary units that occurred around the time of the late Paleozoic Alleghany orogeny. Though the need for fluid is accepted, the original source of the mineralizing fluid is not agreed upon. We use the stable isotopic composition of authigenic illite from clay-rich sedimentary horizons in the Central Appalachian fold-thrust belt to constrain the identity of the migrating fluids. Hydrogen isotopic signatures recorded in authigenic illite indicate that downward infiltrating meteoric fluid was a significant component of the migrating fluid, making up >25% of the fluid volume. Oxygen isotopic signatures confirm that fluid-rock buffering occurred along the infiltration/migration pathway of the surface-sourced fluids. $^{40}Ar/^{39}Ar$-dating of the illitic material points to relatively young, late Permian to Triassic age for mineralization, suggesting that fluid migration and rock alteration continued for several tens of millions of years.

Introduction

The foreland fold-thrust belt of the Appalachian mountains played a central role in developing the understanding of fold-thrust belt geometry. Debate surrounding the structure of fold-thrust belts, particularly following the rise of plate tectonic theory in the

1960s and 1970s, led to considerations of thick- vs. thin-skinned deformational style (e.g. Gwinn, 1964) and forelandward vs. hinterlandward propagation and style of deformation (e.g. Milici, 1975; Perry, 1978). With hydrocarbon reservoirs and ore-deposits common in both the Appalachians and other fold-thrust belts (e.g. Rich et al., 1921; Davis et al., 1983; Oliver, 1986; de Witt and Milici, 1989; Feiss and Slack, 1989; Bethke and Marshak, 1990; Kesler and van der Pluijm, 1990; Cooper, 2007) the nature of fluid involvement and migration within these belts has been hotly debated (e.g. Engelder, 1984; Garven and Freeze, 1984; Oliver, 1986; Hearn et al., 1987; Schedl, 1993; Bethke and Marshak, 1990; Garven, 1995; Ge and Garven, 1989). In the Appalachian Basin, lead-zinc ores known as Mississippi Valley Type (MVT) deposits, have been proposed to form from due to the migration of seawater-derived basinal brines and their subsequent mixing with other fluids (Leach et al., 2010). The driving forces of the fluid migration have been proposed to be both topography-induced gravity-driven flow and compaction and burial pressure/temperature-driven flow (Leach et al., 2010). Constraining the nature and pathways of crustal fluids in fold-thrust belts not only gives insight into the origin of economic deposits, but also sheds light on fluid-driven mechanical processes during deformation.

Fluids in fold-thrust belts facilitate rock deformation by decreasing the effective magnitude of crustal stresses and thus reducing sliding resistance along fault planes and bedding planes. Hubbert and Rubey (1959) proposed that high fluid pressures along the basal décollement of a fold-thrust belt allowed fault blocks to slide en masse above a shallowly-dipping fault. Others have questioned the plausibility of this hypothesis, arguing that due to the hydraulic conductivity of the faulted upper crust, hydrostatic rather than lithostatic fluid pressure are more likely to exist down to ~12 km (Zoback and Townend, 2001). In essence, the nature of the fluids involved in thrusting depends on two primary factors: the volume of available fluids in existing source reservoirs and the driving forces that cause those fluids to migrate through the deformed and deforming rock.

In many studies of fold-thrust belts, fluid origins have been interpreted to vary in both time and space. For instance, in the Pyrenean belt, early closed-system behavior involving metamorphic and formational fluid, followed by late-stage participation of surface-derived meteoric fluids has been observed (Travé et al., 1997; Travé et al., 2007; Lacroix et al., 2014). In the Andean pre-cordillera of Argentina, Lynch and van der Pluijm (2016) observed stable isotopic signatures that indicated the dominance of surface fluids throughout the history of the belt. A similar pattern was observed in several studies in the Idaho-Montana section of the North American Cordillera (Bebout et al., 2001; Anastasio et al., 2004; Rygel et al., 2006; Lynch et al, *in review*). In contrast, the early fluid regime of the Central Appalachian belt of eastern North America has been interpreted as stratigraphic compartmentalization of fluids, with deeply sourced hot migrating brines confined to lower rock layers while surface-sourced fluids dominated the upper layers (Evans and Battles, 1999). During the latest stages of compression, however, deformation-enhanced permeability allowed these fluid reservoirs to mix and surface fluids to infiltrate into the deformed layers (Evans et al., 2012).

Previous studies of fluid signatures in the Appalachian belt have mostly relied on stable isotopic and fluid inclusion studies of secondary veins. The focus on vein and fluid inclusion studies for the characterization of deformational fluids has provided the opportunity to understand the temperature and salinity of these fluids in addition to their isotopic composition. However, veins are secondary deformation features, whereas host rock clay minerals are regionally pervasive, and thus provide the added benefit of offering paired O-H data from a single phase, for fluid fingerprinting.

Clay minerals are a major hydrogen-containing component of upper crustal rocks. They form in the presence of aqueous fluids either as weathering products or through direct precipitation at low pressure and low temperature (sub-metamorphic) conditions (De Segonzac, 1970; Savin and Hseih, 1998; Moore and Reynolds, 1997; Vrolijk and van der Pluijm, 1999; Haines and van der Pluijm, 2012). Historically, their utility as a fluid recorder has been used extensively in paleosols and soil minerals to draw conclusions on the climate and/or elevation history of a region (e.g. Lawrence and Taylor, 1971; Savin and Hseih, 1999; Chamberlain et al., 1999; Morad et al., 2003; Chamberlain et al., 2012; Mulch and Chamberlain, 2007; Feng et al., 2013; Mix and Chamberlain, 2014). The hydrogen isotopic composition of fine-grained authigenic clays can be determined in faulted (e.g. Mulch et al., 2004; Fitz-Diaz et al., 2011; Lacroix et al, 2012; Boles et al., 2015; Haines et al., 2016, Lynch and van der Pluijm, 2016; Gébelin et al., 2015; 2017) and folded (e.g. Fitz-Diaz et al., 2014; Lynch et al., *in review*) units in a range of deformational environments. Additionally, the occurrence of the potassium-rich clay mineral illite allows for the radiometric dating of clay formation and thus constrains the timing of fluid presence in the rock units (Fitz-Diaz and van der Pluijm, 2013; Wang et al., 2016). This study exploits the abundant clay-rich sedimentary units in the Central Appalachian Valley-and-Ridge province to determine the nature and timing of fluid involvement during the last pulse of regional deformation of this fold-thrust belt.

Geologic Background

The Appalachian Orogen

The Appalachian Mountains of eastern North America span nearly the entire length of the continent's margin, running approximately 3000 kilometers Northeast-Southwest from Georgia to Newfoundland. The mountain belt is narrowest in the area of the New York promontory, north of which is characterized by the presence of large accreted terranes and strike-slip faulting, and south of which is characterized by the deformation of a regionally extensive sedimentary wedge in a series of folds and thrusts (Chamberlain, 1910; Gwinn, 1970; Hatcher et al., 1989; Fiall, 1997a; 1997b; Hatcher, 2010). The growth of the Appalachian mountain belt, which occurred during the Paleozoic, was preceded by Precambrian rifting of the Neoproterozoic supercontinent Rodinia and the subsequent development of a passive margin along the Laurentian margin (Bird and Dewey, 1970; Fiall, 1997a). The opening of the ocean basin allowed for the development of extensive carbonate platforms during the Cambrian and Ordovician periods prior to the initiation of siliciclastic sedimentation in the Late Ordovician, which continued throughout the several orogenic phases (Fiall, 1997a; 1997b; Hibbard et al., 2010).

Deformation and tectonism was heterogeneous, both regionally and temporally. Several deformational events record accretions of oceanic island arcs, microcontinents, and allochthonous crustal terranes that collided with the Laurentian margin, and which were accompanied by coeval igneous activity and sedimentation (Hatcher et al., 1989; Faill, 1997a). Three main stages of Paleozoic orogeny are recognized (e.g. Bird and Dewey, 1970; Jamieson and Beaumont, 1988; Faill, 1997a; 1997b; 1998; Hatcher, 2010;

Hibbard et al., 2010). The Ordovician Taconic orogeny occurred due to the accretion of an oceanic island chain, which resulted in the creation of the Appalachian foreland basin, effectively ending carbonate deposition and beginning the massive and protracted influx of siliciclastic material (Faill, 1997a, b). The Silurian-Devonian Acadian orogeny caused extensive plutonism and deformation with the accretion of the Avalonia terrane, which occurred primarily in the central and northern portion of the orogen. The final stage of mountain building, the Alleghanian orogeny, resulted from the terminal collision of the continents Laurentia and Gondwana to form the supercontinent Pangea in the Late Mississippian to Permian time (Hatcher et al., 1989; Fiall, 1998; Hatcher, 2010). This collision occurred obliquely and diachronously, causing compression and dextral strike-slip motion in the Northern Appalachians and the clockwise rotation of Gondwana along the Laurentian margin, marking intense shortening and long distance thrust translation in the Southern Appalachians (Hatcher et al., 1989).

The characteristics of both the orogen and its foreland deformation belt vary along strike. Decollements occurred primarily in shale horizons, promoting thrusting along shallowly southeast dipping structures (Milici, 1975; Perry, 1978; Hatcher et al., 1989; Hatcher, 2010, Sak et al., 2012). In the southernmost Appalachians, these thrusts, which are exposed at the surface, place Lower Paleozoic carbonates and crystalline rocks on top of a relatively thin package of younger sediments (Gwinn, 1964; Perry; 1978; Hatcher et al., 1989; Hatcher, 2010). In contrast, in the central portion of the Appalachian belt, the thick stack of Paleozoic sediments are deformed and folded due to blind thrusts in the Lower Paleozoic carbonates at depth (Perry, 1978; Hatcher et al., 1989; Sak, 2012). The Pennsylvania Valley-and Ridge province is a striking expression of this geometry and is characterized by large (kilometer to tens of kilometer) scale folding, which is defined by the surface traces of resistant folded layers (Chamberlain, 1910; Gwinn, 1964; Perry, 1978; Mitra, 1987; Sak, 2012) (Figure V.1). The Central Appalachian Pennsylvania salient, the trend of which curves from nearly N-S to nearly E-W trending over a span of a few hundred kilometers, has been well-studied as the source of debate regarding both the origin of the mountain belt's curvature and the general structural history of this part of the mountain belt (e.g. Kent, 1988; Geiser and Engelder, 1983; Gray and Stamatakos, 1998; Cederquist et al., 2006; Ong et al., 2007).

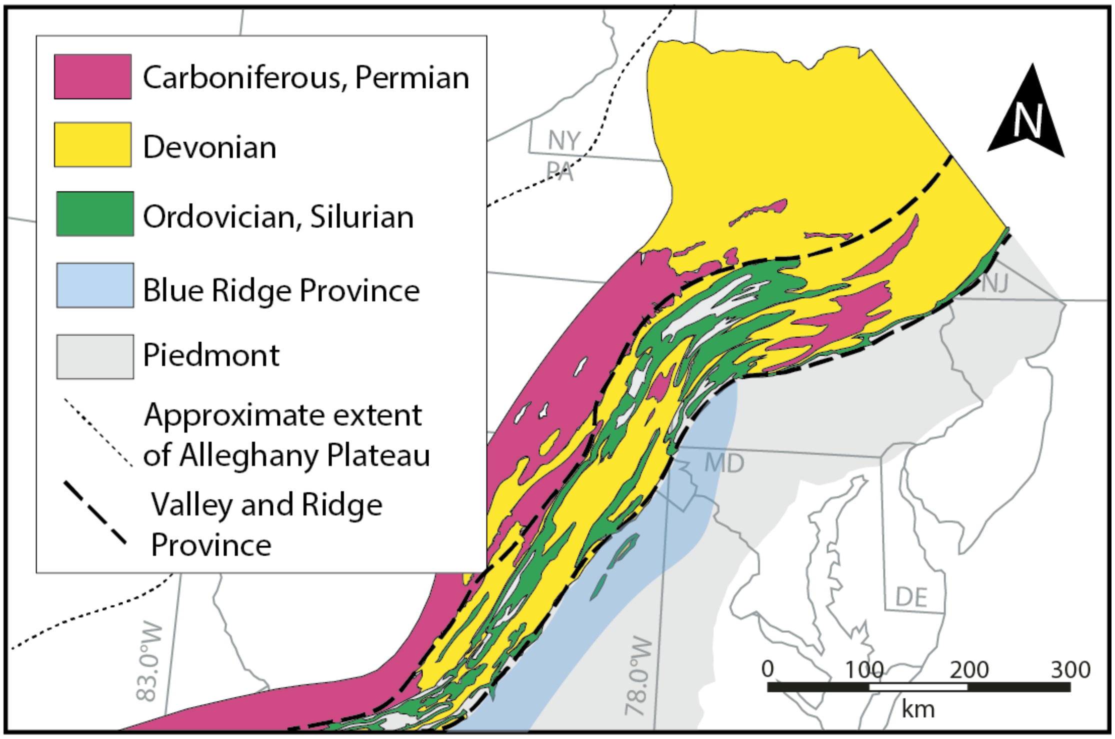

Figure V.1: Map adapted from Hibberd et al. (2010) showing the distribution of sedimentary units by age and their locations within the major tectonic regions of the Central Appalachians.

The Pennsylvania Salient

The Pennsylvania salient is divided into several geologic and structural provinces based on rock type/age and deformation style (Mitra, 1987; Hibbard, 2010) (Figure V.1). Approaching the mountains from the continental interior to the west, the first noticeable change in structural style is the gentle warping of nearly flat-lying beds, exposed in road cuts and river channels. This region is the Allegheny Plateau, an uplifted region of little-deformed, largely syntectonically deposited foreland basin sedimentary units. Crossing the structural front, the lowest (Mississippian) members of these foreland clastic wedge sediments are exposed along with the thick Lower Paleozoic passive margin sequence in large anticlines and synclines (Chamberlain, 1910; Gwinn, 1964; Perry, 1978; Mitra, 1987). Geophysical data (Perry, 1978; Wilson, 1989; Wilson and Shumaker, 1992) and structural analyses (Evans, 2010; Sak et al., 2012) have led to the interpretation that these large folds overlie duplexed Cambrian and Lower to Middle Ordovician carbonates that are bounded by major thrust faults in the Cambrian Waynesboro formation at their base and in the Ordovician Martinsburg and Reedsville Shales above (Perry, 1978; Wilson, 1989; Sak et al., 2012) (Figure V.2). Continuing further eastward reveals deeper Carbonate units of the passive margin sequence, brought up to the surface by Alleghany thrust faulting along the North Mountain Thrust (Evans, 1989). Moving further coastward, the crystalline, metamorphic interior of the belt is exposed along with slivers of the Precambrian, Grenville basement units (Faill, 1998; Hibberd et al, 2010; Sak et al., 2012). The easternmost portion of the crystalline interior is covered by younger sedimentary units of the Piedmont province, which were deposited following the Mesozoic breakup of Pangea (Hibbard et al., 2010). The presence of Mesozoic diabase dikes is also attributed to the rifting of the supercontinent and the opening of the Central Atlantic Ocean (Sutter, 1988; Roden, 1991; Faill, 1997a).

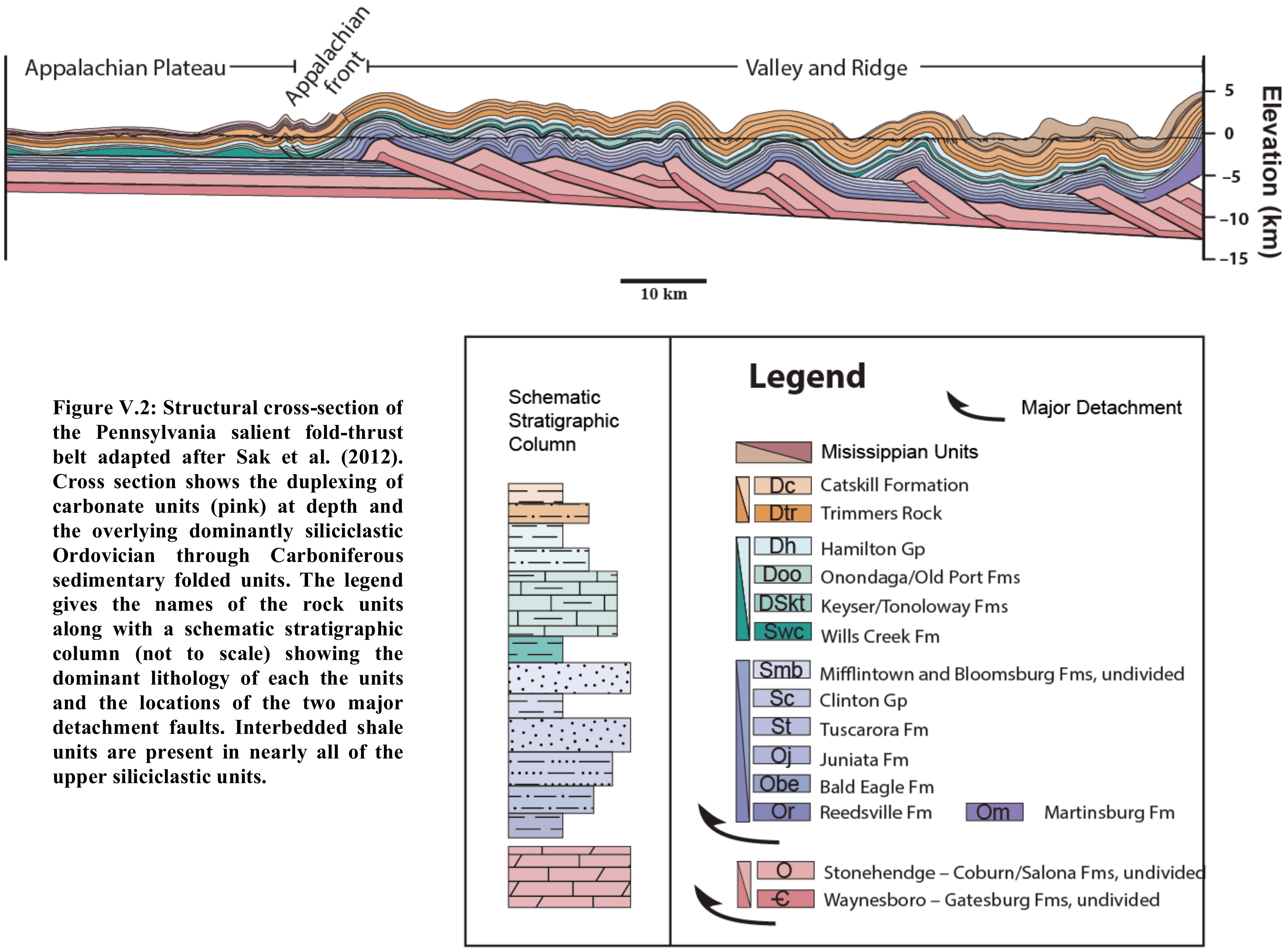

Figure V.2: Structural cross-section of the Pennsylvania salient fold-thrust belt adapted after Sak et al. (2012). Cross section shows the duplexing of carbonate units (pink) at depth and the overlying dominantly siliciclastic Ordovician through Carboniferous sedimentary folded units. The legend gives the names of the rock units along with a schematic stratigraphic column (not to scale) showing the dominant lithology of each the units and the locations of the two major detachment faults. Interbedded shale units are present in nearly all of the upper siliciclastic units.

Sample Collection and Preparation

This study's sampling campaign targeted the abundant clay-rich, clastic sedimentary units exposed in the Central Appalachian foreland fold-thrust belt. Samples of clay rich sedimentary rocks were collected along two major transects of the Pennsylvania salient: along route 322 from Harrisburg and to College, and along routes 22 and 473 from Mount Union to Hollidaysburg and Tyrone (Figure V.3). Additional samples were collected to the south in the West Virginia and Maryland sections of the fold-and-thrust belt for increased spatial coverage of the belt. Shaly samples range from Late Ordovician to Upper Devonian in age and were collected from outcrops in both the back limbs and fore limbs of major Alleghanian folds. In outcrop, these rocks ranged from nearly flat-lying to steeply dipping, and were variably mesoscopically deformed, with some outcrops displaying approximately meter(s) scale folding, whereas others displayed signs of jointing, veining, and fracturing (Figure V.4). Many beds sampled showed signs of bedding parallel shear, particularly striations and sinusoidal cleavages. Where possible, care was taken to avoid visibly altered surface weathering and plant roots by digging several tens of centimeters into the outcrop with a rock pick. Approximately 1 kilogram of material was collected for processing. Sampling locations are shown in Figure V.3 and described in Table V.1.

Rock samples were processed in the clay lab at the University of Michigan. Each sample was scrubbed with a stiff brush and rinsed in deionized water to remove any surface contaminants. Samples were then disaggregated by hand in an agate mortar and pestle. Approximately 50-60 grams of disaggregated material was then suspended in deionized water and placed in an ultrasonic bath for approximately 15 minutes in order to promote the separation of clay grains. Sample material was then organized into 6 grain size fractions by high speed centrifugation in accordance with Stokes Law. Five fractions were used for x-ray diffraction (XRD) analysis: Fine = <0.05 µm, Medium Fine = 0.05-0.1 µm, Medium = 0.1-0.2 µm, Medium Coarse = 0.2-1 µm, Coarse = 1-2 µm), the coarsest fraction (>2 µm) was excluded from analyses.

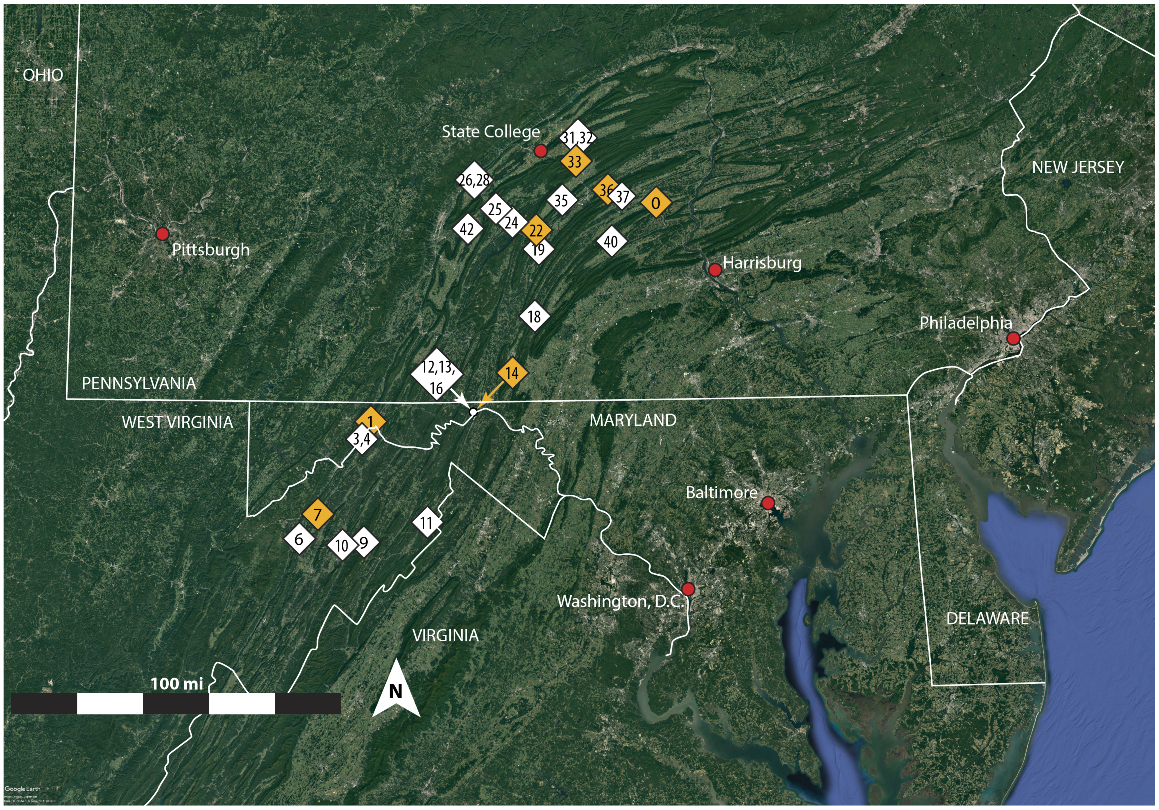

Figure V.3: Google Earth image showing the location of the samples collected from the Central Appalachian foreland fold-thrust belt. Numbers within the symbols correspond to sample names shown in Table V.1. Orange symbols denote the samples that were selected for ^{40}Ar/^{39}Ar-dating.

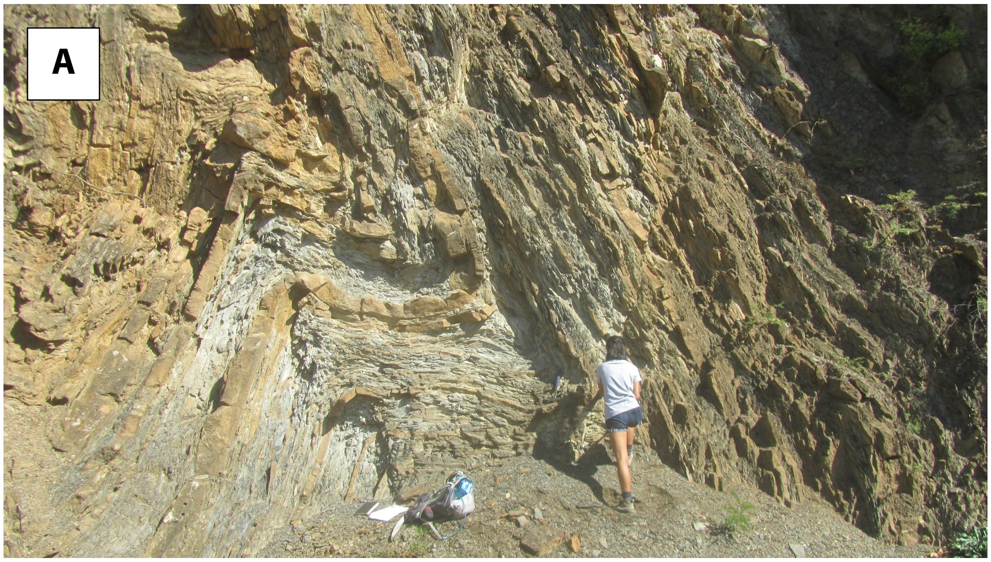
A


B


C

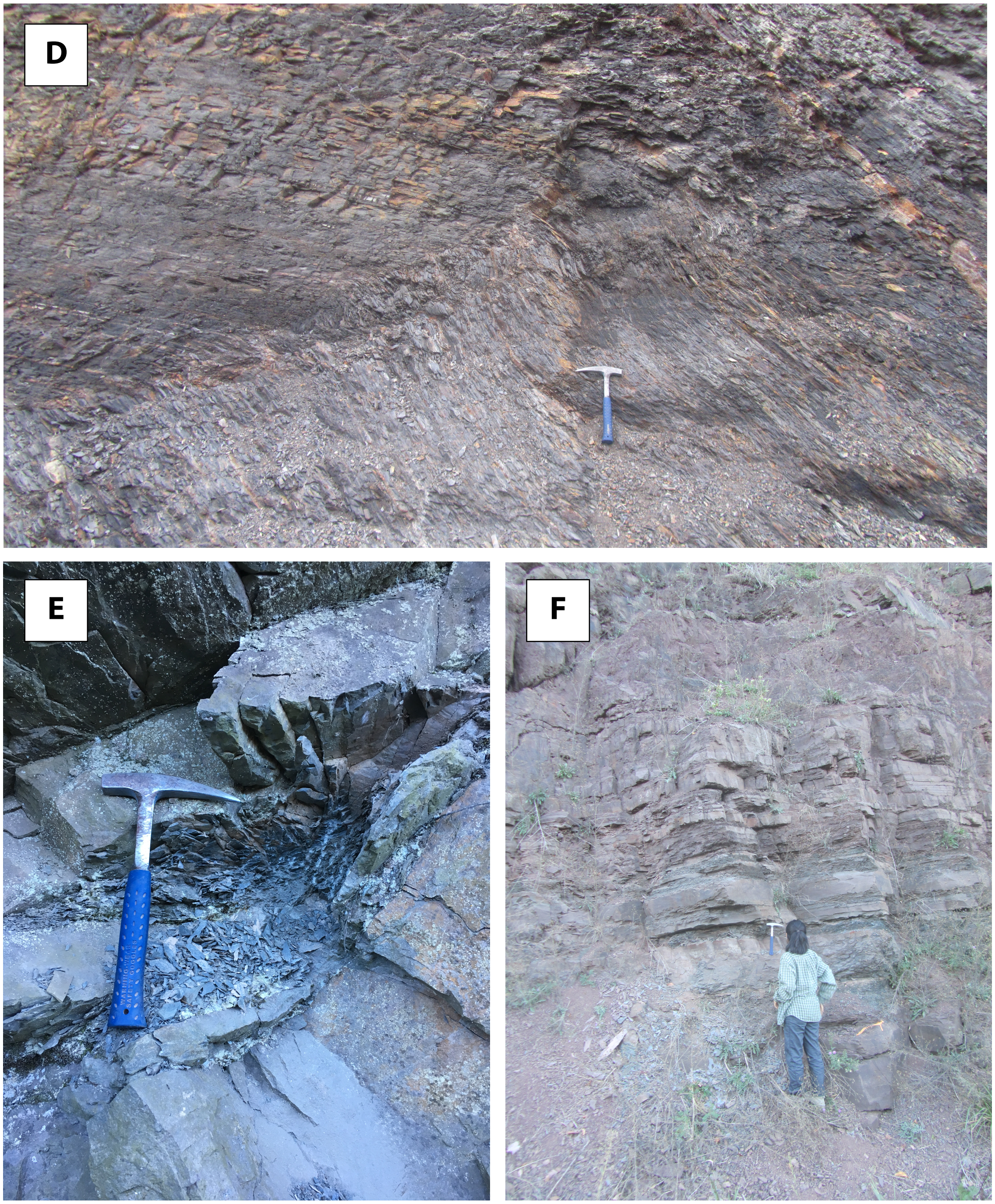

Figure V.4: Field photographs of shale outcrops and samples collected. (A) Railroad cut outcrop of folded McKenzie formation near Pinto, MD (sample MDMcK4), (B) road cut outcrop of Bloomsburg and Wills Creek formation near the intersection of routes 22 and 747 in Mt. Union, PA (samples, PABF22 and PAWC23), (C) close-up of Wills Creek cleavage at locale depicted in 4b (sample PAWC23), (D) folded Devonian shale outcrop on 522 just south of Allensport, PA (PADS19), (E) cleaved and veined clay-rich bedding plane in Will Creek formation road-cut on route 22 southeast of Alexandria, PA (sample PAWC25), (F) alternating coarse and fine-grained red beds of the Juniata formation along eastbound route 522 northwest of the Laurel Creek Reservoir (sample PAJF32).

Table V.1: Sample descriptions and locations

Sample	Age	Unit	Description	Lat (°N)	Long (°W)
1. MDMS1	Silurian	Clinton Group	Kink fold limb	39.6085	78.8076
3. MDRH3	Silurian	Clinton Group, Rose Hill Fmn	Sheared anticline core	39.6085	78.8076
4. MDMcK4	Silurian	Clinton Group, McKenzie Fmn	vertical limb of kink fold	39.5667	78.8342
6. WVOS6	Ordovician	Martinsburg Fmn	hinge zone, Will's Mt. anticline	39.1285	79.1870
7. WVMcK7a	Silurian	Clinton Group, McKenzie Fmn	eastern limb, Wills Mt. anticline	39.1265	79.1817
9. WVDS9	Devonian	Devonian Black Shale	Shale with slickenlines on bedding surfaces	39.0781	78.9304
10. WVDM10	Devonian	Devonian Mudstone	pencil cleavage in mudstone	39.1026	78.8473
11. WVDS11	Devonian	Devonian Black Shale	vegetated shale outcrop	39.1823	78.4937
12. MDWC12	Silurian	Wills Creek Fmn	slickenlines on bedding in anticline core	39.6771	78.2289
13. MDWC13	Silurian	Wills Creek Fmn	just below mesoscale fault	39.6771	78.2289
14. MDBF14	Silurian	Bloomsburg Fmn	folded shale interbedded with coarser grained units	39.6774	78.2250
16. MDMcK16	Silurian	Clinton Group, McKenzie Fmn	anticline core	39.6774	78.2250
18. PAS18	Silurian	Rose Hill Fmn	greenish, pencil cleavage shale	40.0770	77.8860
19. PADS19	Devonian	Devonian Black Shale	small kink folds	40.3574	77.8618
22. PABF22	Silurian	Bloomsburg Fmn	steeply dipping red shale	40.3947	77.8778
24. PADS24	Devonian	Devonian Black Shale	cleaved shale	40.4772	77.9974
25. PAWC25	Silurian	Wills Creek Fmn	small kink bands in mesoscale folded layer	40.5400	78.0882
26. PARS26	Ordovician	Reedsville Shale	red shale w/bed parallel slickenlines	40.6491	78.1982
28. PAF28	Ordovician	Bald Eagle Fmn	minor fault in sandstone/mudstones	40.6644	78.2252
31. PARSBE31	Ordovician	Reedsville Shale	grey shale near Bald Eagle formation contact	40.7810	77.6197
32. PAJF32	Ordovician	Juniata Fmn	red clay layer interbedded w/ sandstone	40.7605	77.6147
33. PARH33	Silurian	Clinton Group, Rose Hill Fmn	steeply dipping grey shale with	40.7346	77.6356

Table V.1: Sample descriptions and locations

Sample	Age	Unit	Description	Lat (°N)	Long (°W)
			red/orange slickenlines		
35. PARS35	Ordovician	Reedsville Shale	grey shale	40.5724	77.7315
36. PABF36	Silurian	Bloomsburg Fmn	brown-grey shale	40.6083	77.4369
37. PARH37	Silurian	Clinton Group, Rose Hill Fmn	steeply dipping reddish shale	40.5967	77.3829
40. PASS40	Silurian	Bloomsburg Fmn	red shale	40.4050	77.4370
42. PAWC42	Silurian	Wills Creek Fmn	grey shale with small folds	40.4844	78.2530
0. SNPA7	Silurian	Clinton Group, Rose Hill Fmn	greenish shale	40.5653	77.1942

X-Ray Diffraction and Mineral Quantification

Methods

For the 5 retained size fractions of each sample, multiple XRD preparations were done in order to fully characterize the mineral components and their proportions in each aliquot. First, oriented slides were created through the settling method (Moore and Reynolds, 1997) in order to determine the identities of clay minerals present in each sample. Samples were also prepared into top-loaded randomly oriented powder mounts for quantification of the mineral populations by both the end member polytype mixing method (e.g. Haines and van der Pluijm, 2008) and by Rietveld refinement method (Rietveld, 1969; Bergmann et al., 1998; Ufer and Kleeburgh, 2015; Boles et al., 2018). Samples were analyzed in the Electron Microbeam Analysis Lab at the University of Michigan on a Rigaku Ultima VI X-Ray Diffractometer with a CuKα source, which was operated at 40 mV and with an accelerating velocity of 44 mA. Oriented mounts were analyzed at a speed of 1°/minute from 2-40°2θ with a step size of 0.05°2θ. Oriented clay slides provide a qualitative assessment of the populations of clay minerals present as well as a first-order estimation of clay mineral proportions by emphasizing basal (001) peaks.

Since most polytype specific peaks are not within the (001) plane, however, oriented mounts cannot be used for quantitative polytype estimations.

For quantitative determination, high-resolution analyses of randomly oriented powders are required (e.g., Moore and Reynolds, 1997; Hillier, 2000). For the end-member matching method, samples and standards were analyzed on a 10-sample stage from 16-44°2θ, with a step size of 0.05° at a speed of 0.3°/minute. The end-member matching method provides an estimate of the proportion of high-temperature 2M1 illite to low-temperature 1Md illite that produces errors of approximately 2-3% under conditions in which illite is the dominant mineral present. (See Haines and van der Pluijm, 2008 and Lynch et al., 2016 for specifics on the standards and methods used.) In the common case in which the mineralogy of the sample is more complex, for instance samples comprised of multiple populations of clay minerals or other non-clay minerals, Rietveld refinement offers a better estimation of total mineral proportions. For Rietveld analysis, as for the end-member matching technique, samples were analyzed at a speed of 0.3°/min and a step size of 0.05°. Importantly, nearly the complete range of x-ray diffraction angles from 2-80°2θ was measured in order to precisely quantify mineral proportions. The Rietveld refinement was done using the BGMN software package (Bergmann et al., 1998) and the Profex user interface (Doebelin and Kleeburg, 2015); see Boles et al., (2018) for details.

The BGMN program uses least-squares regression analyses to minimize the mismatch between a sample XRD spectra and a modeled pattern (R, Equation 1)

Eq. 1
$$R = \left[\frac{\sum_{i=1}^{M} w_i (y_i - y_{ic})^2}{\sum_{i=1}^{M} w_i {y_i}^2}\right]^{\frac{1}{2}}$$

in which M is the length of the XRD pattern, y_i is the measured intensity at point i, y_{ic} is the computed intensity at point i, and w_i is the weight at point i, which is proportional to the counting time at point *i* (Bergmann, 2005). The software comes with a library of mineral structure files, which is regularly updated by community input. The analysis relies on the qualitative identification of minerals present prior to refinement (Kleeburg, 2009), which we completed using oriented clay mounts. Then, from the structure file library, the user selects the identified mineral components of each sample to be used in the refinement procedure, and through several iterations with various mixtures of input mineral structure files, the refinement algorithm converges on the optimal proportion of each mineral to closely match the sample pattern indicated by small R-vales. With highly crystalline and chemically homogenous samples, misfit values can be low ($R \leq 2\%$). Expected mineral quantification errors in such cases are on the order of 1-2% (Bergmann, 2005). In the case of clays, there is often a non-negligible degree of disorder and cation substitutions even within a single mineral population, making precise quantifications more challenging (Ufer et al., 2012; Ufer and Kleeburg, 2015). Generally, if background parameters are realistic and the model is chemically and mineralogically plausible, a misfit measurement R-value ~≤5% is considered a good fit for clay mineral quantification (Toby, 2006). In the case of these samples, quantification errors are likely ≤3% (Kleeburg, 2009).

Results

Results of the Rietveld refinement reveal the presence of many common siliciclastic minerals, including quartz, calcite, hematite, titanium oxides, and high-temperature micas that coexist with low-temperature clay minerals, including illite, chlorite, and occasionally kaolinite. The proportion of high-temperature ($2M_1$) and low-temperature ($1M_d$) polytypes of illite are reported in Table V.2.

Table V.2a: Illite quantification results					
		Rietveld*		End-Member Matching	
Sample	Fraction	%1M_d	%other clay	%1M_d	%2M_1
MDMS1	C	57	43	28	72
	MC	68	32	48	52
	M	86	14	62	38
	MF	92	8	87	13
	F	97	3	98	2
MDRH3	C	59	41	20	80
	MC	68	32	30	70
	M	88	12	35	65
	MF	94	6	82	18
	F	97	3	100	0
MDMcK4	C	26	74	15	85
	MC	52	48	38	62
	M	83	17	49	51
	MF	93	7	80	20
	F	97	3	92	8
WVOS6	C	87	13	40	60
	MC	91	9	45	55
	M	95	5	50	50
	MF	96	4	88	12
	F	99	1	97	3
WVMcK7a	C	56	44	25	75
	MC	87	13	40	60
	M	90	10	70	30
	MF	94	6	83	17
	F	97	3	95	5
WVDS9	C	52	48	10	90
	MC	70	30	25	75
	M	64	36	45	55
	MF	91	9	85	15
	F	96	4	98	2
WVDM10	C	77	23	0	100
	MC	68	32	10	90
	M	90	10	61	39
	MF	94	6	83	17
	F	95	5	100	0
WVDS11	C	54	46	0	100
	MC	58	42	42	58
	M	93	7	62	38
	MF	99	1	92	8
	F	99	1	100	0
MDWC12	C	46	54	10	90
	MC	66	34	15	85
	M	56	44	45	55
	MF	93	7	65	35
	F	79	21	100	0

Table V.2a: Illite quantification results

		Rietveld*		End-Member Matching	
Sample	Fraction	%1M_d	%other clay	%1M_d	%2M_1
MDWC13	C	91	9	30	70
	MC	30	70	35	65
	M	86	14	40	60
	MF	95	5	75	25
	F	95	5	90	10
MDBF14	C	32	68	15	85
	MC	48	52	15	85
	M	50	50	52	48
	MF	90	10	80	20
	F	94	6	92	8
MDMcK16	C	50	50	15	85
	MC	42	58	35	65
	M	46	54	40	60
	MF	93	7	65	35
	F	96	4	87	13
PAS18	C	58	42	18	82
	MC	44	56	27	73
	M	93	7	55	45
	MF	96	4	85	15
	F	97	3	93	7
PADS19	C	80	20	10	90
	MC	91	9	60	40
	M	95	5	90	10
	MF	96	4	100	0
	F	-	-	-	-
PABF22	C	56	44	15	85
	MC	63	37	46	54
	M	97	3	52	48
	MF	92	8	90	10
	F	97	3	100	0
PADS24	C	70	30	22	78
	MC	57	43	30	70
	M	68	32	40	60
	MF	95	5	75	25
	F	-	-	-	-
PAWC25	C	79	21	35	65
	MC	92	8	51	49
	M	86	14	58	42
	MF	92	8	75	25
	F	95	5	80	20
PARS26	C	82	18	30	70
	MC	86	14	47	53
	M	93	7	62	38
	MF	95	5	88	12
	F	99	1	97	3

Table V.2a: Illite quantification results

		Rietveld*		End-Member Matching	
Sample	Fraction	%$1M_d$	%other clay	%$1M_d$	%$2M_1$
PAF28	C	83	17	40	60
	MC	76	24	48	52
	M	50	50	62	38
	MF	95	5	85	15
	F	97	3	95	5
PARSBE31	C	54	46	28	72
	MC	83	17	38	62
	M	87	13	55	45
	MF	93	7	85	15
	F	97	3	93	7
PAJF32	C	61	39	42	58
	MC	66	34	58	42
	M	88	12	62	38
	MF	95	5	81	19
	F	96	4	97	3
PARH33	C	70	30	30	70
	MC	68	32	38	62
	M	88	12	40	60
	MF	96	4	85	15
	F	98	2	95	5
PARS35	C	89	11	35	65
	MC	92	8	45	55
	M	93	7	52	48
	MF	95	5	80	20
	F	96	4	92	8
PABF36	C	74	26	15	85
	MC	83	17	20	80
	M	90	10	45	55
	MF	97	3	75	25
	F	97	3	90	10
PARH37	C	31	69	18	82
	MC	53	47	60	40
	M	35	65	40	60
	MF	96	4	88	12
	F	95	5	95	5
PASS40	C	41	59	35	65
	MC	64	36	45	55
	M	88	12	63	37
	MF	93	7	82	18
	F	94	6	90	10
PAWC42	C	46	54	15	85
	MC	26	74	45	55
	M	66	34	70	30
	MF	**	**	82	18
	F	**	**	96	4

Table V.2a: Illite quantification results

		Rietveld*		End-Member Matching	
Sample	Fraction	%1M$_d$	%other clay	%1M$_d$	%2M$_1$
SNPA7	C	22	78	-	-
	MC	22	78	-	-
	M	34	66	-	-
	MF	57	43	-	-
	F	44	56	-	-

*Normalized to 100% clay
**Rietveld Refinement was not successful

Table V.2b: Illite quantification results

Sample	Fraction	%1M$_d$	%2M$_1$
SNPA7	C	77	23
	MC	74	26
	M	83	17
	MF	93	7
	F	95	5

The quality of Rietveld analysis breaks down at small grain sizes, evidenced by large (~5-10%) R-values and unrealistic modeled background intensities. However, at grain sizes <0.1μm, illite tends to be the dominant mineral (with the rare exception of other clay minerals or calcite) and in most cases can be modeled well using the end-member standards method. End-member matching results are also included in Table V.2 so that comparison between the two methods quantification can be made. Despite the difficulties involved in using Rietveld refinement to model fine-grained samples, in most cases the end-member standards method and the Rietveld refinement method give similar clay proportions in the finer fractions, but are notably different in the coarser fractions, with the Rietveld method reporting higher percentages of 1M$_d$ illite than the end member standards method. This is likely due to the fact that an abundance of crystalline grains in coarser fractions (e.g. quartz, calcite, etc.) can lower the overall XRD baseline, causing the end-member method to overestimate 2M$_1$ proportions and underestimate 1M$_d$

proportions. An example of the XRD patterns quantifications are shown for sample MDMS1 in Figure V.5.

$^{40}Ar/^{39}Ar$ Geochronology

Methods

Seven samples were selected for dating based on their favorable mineralogy (i.e. abundant illitic components, no other K-bearing phases, relative simplicity of mineral assemblages) and their spatial distribution in the fold-and-thrust belt. Several size fractions of each sample were prepared for irradiation by vacuum encapsulation within quartz vials. Encapsulation is important for fine-grained samples because it allows the significant proportion of recoiled ^{39}Ar to be trapped and measured along with the retained Ar (e.g., Dong et al., 1995; 1997; Hall, 2014; van der Pluijm and Hall., 2015). Samples were irradiated at the McMaster Nuclear Reactor and measured on a VGS1200s mass spectrometer in the Argon Geochronology Laboratory at the University of Michigan in August of 2017. In October of 2017, a systematic laboratory error due to a leak in a section of the vacuum line was discovered. This error caused the calculated total gas $^{40}Ar/^{39}Ar$-ages to be erroneously young. After the mechanical problem was rectified, we re-dated the majority of the samples to determine the true age. However, some samples were not re-run. For these samples we use a correction procedure based on the error age (see Appendix B for details) to determine the true age of the samples. In this study, we use 10 re-run ages and 10 corrected ages, reported in Table V.3.

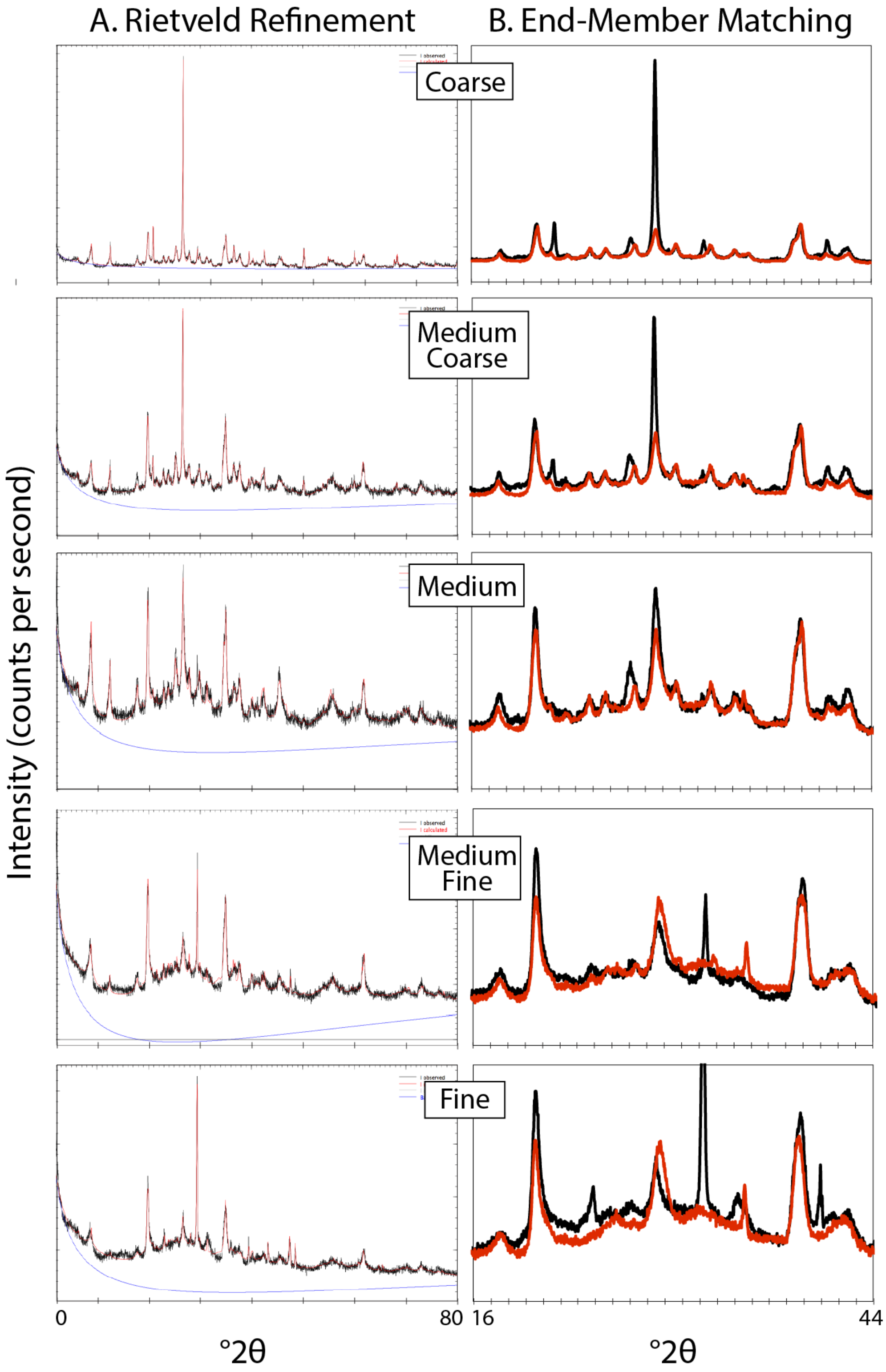

Figure V.5: XRD quantifications for sample MD-MS-1. In both A and B, the black line shows the actual scanned XRD pattern, while the red line shows the modeled result. The major difference between the two methods arises from the fact that the Rietveld method models the whole pattern, whereas the end-member method models only the illite patterns. Quartz peaks (20.8, 26.5) and calcite peaks (23, 29.5, 36) can be seen in the end-member method where the red line does not match the black line.

Table V.3: ^{40}Ar/^{39}Ar-dating results

Sample	Fraction	Age (Ma)	Error (Ma)	Age of Authigenic Illite	Age of Detrital Illite
SNPA7	C	460	1.43	273 ± 31.8 Ma	890 ± 144.2 Ma
	M	376*	8		
	F	334.38	1.33		
MDMS1	M	383	1.12	271 ± 8.6 Ma	563 ± 39.5 Ma
	MF	332*	7		
	F	271	1.24		
WVMcK7a	MC	436*	9	258 ± 8.9 Ma	567 ± 31.7 Ma
	MF	329	0.66		
	F	261	1.06		
MDBF14	MC	365*	7	239 ± 6.3 Ma	398 ± 18.7 Ma
	M	346*	7		
	MF	276*	6		
	F	244*	5		
PABF22	M	386	0.96	250 ± 8.0 Ma	531 ± 30.0 Ma
	MF	318*	6		
	F	245	1.16		
PARH33	MC	392	1.63	242 ± 7.2 Ma	492 ± 23.6 Ma
	MF	302*	6		
	F	246	0.93		
PABF36	F	266*	5	266 ± 5 Ma	-

*Corrected age (See Appendix B)

Age of Authigenic Illite

Regression analyses using a York-style regression were completed to determine the age of the authigenic and detrital illitic components of the samples (York, 1968). Re-measured or corrected total gas ages for each sample size fraction aliquot are used to calculate end-member ages (Table V.3) along with the results of the regression analysis and the interpreted absolute age of the authigenic and detrital illitic components at each sample location.

The three samples along the Harrisburg to State College transect are younger from east to west: 273 ± 31.8 Ma, 266 ± 5 Ma, and 242 ± 7.2 Ma. One other PA sample taken along the more southern transect matches the projection along the section, falling between the two younger ages as predicted by its position: 250 ± 8.0 Ma. In Pennsylvania, the easternmost and oldest sample SNPA7 yields a Permian age for deformation-mediated illite growth, whereas the westernmost and youngest sample records a Triassic age for illite growth. Thus, we see a >40 million year (278-236 Ma) systematically younger ages from east to west in the belt. Three dated samples from Maryland and West Virginia are aged between the oldest and youngest Pennsylvania samples, but do not appear follow a geographic pattern in their age distribution. The oldest samples coincide with the timing of peak Alleghany orogeny; others are younger, including ages in the youngest deformed unit (the Dunkard group, 266Ma) in the Pennsylvania salient (Hatcher et al., 1989).

Whereas deformation peaked in the Early Permian, there is evidence that burial metamorphic conditions continued well past the peak of the orogeny. Following peak metamorphic temperatures in the Permian, coinciding with peak deformation, ambient temperatures in the region stayed relatively high (>300°C) into the early Triassic (~250Ma) (e.g., Farrar, 1985). Similarly prolonged metamorphic temperatures were observed from biotite Ar-ages in the Avalonian basement terrane in the Northern Appalachian of Rhode Island (Dallmeyer, 1982; Wintsch et al., 1992).

Our Permian-Triassic ^{40}Ar/^{39}Ar-ages show that illite growth continued for tens of millions of years following the peak of orogenic activity, reflecting burial metamorphic conditions or fluid migration, or both. Notably, this age range coincides with estimates of the age of remagnetization that occurred across the Appalachian belt during and following the main phases of deformation, which was hypothesized to originate from the passage of fluids (Miller and Kent, 1988; Lu et al., 1990; Stamatakos et al, 1996; Cederquist et al., 2006).

Stable Isotopic Analysis

Methods

All stable isotopic analyses were completed in the Stable Isotope Laboratory at the University of Lausanne's Institute for Surface Dynamics. Prior to oxygen analyses, ~1.5-2.0 mg of sample was loaded onto a platinum holder and dried in a 110°C oven for at least 6 hours. Samples were transferred to a vacuum line and pumped to a vacuum of approximately 10^{-6} mbar. The sample chamber was then pre-fluorinated overnight in order to react with and remove any atmospheric water that adsorbed to the clay particles. Samples were heated with a CO_2 laser in the presence of F_2 gas to liberate the mineral bound oxygen. Excess F_2 was then separated from the produced O_2 gas by reaction with KCl at 150°C to produce KF and Cl_2 gas. Cl_2 gas was removed by liquid N_2 traps as O_2 gas was collected on a molecular sieve. O_2 gas samples were then expanded into a Thermo Finnigan MAT 253 IRMS for measurement. Oxygen isotope values are reported using δ-notation relative to VSMOW and errors are smaller than ±0.2‰ for all samples analyzed.

Hydrogen isotopic measurements were done on a TC/EA using methods adapted after Sharp et al. (2001). For each aliquot, approximately ~1.5-2.0 mg of sample material as measured and folded into a silver foil cup. Encapsulated samples were held overnight in a vacuum desiccator to remove adsorbed atmospheric water. Samples were then transferred to a helium-flushed, zero-blank autosampler attached to the TC/EA. Samples were introduced into a furnace at 1450°C to reduce H_2O to H_2 and CO for the gases to be transferred via a He-carrier gas through a gas chromatographic column and into a Thermo Delta Plus XL mass spectrometer. Hydrogen isotope values are also reported using δ-notation relative to VSMOW and errors are >3‰ for most samples and ≥5‰ for all samples (see details in Table V.4).

Isotopic Composition of End-Member Authigenic Illite

To determine the composition of the authigenic illite component in shale samples, we completed a sequence of York-style regressions (example shown in Figure V.6) between the δD composition of each size fraction and the $\%1M_d$ calculated using both the Rietveld refinement and end-member matching methods (York, 1968). Despite the variation in proportion of clay mineral populations determined by each of these two quantification methods (Table V.2), regression analyses yield similar value δD estimates for the authigenic illite end member component (Table V.5), with all but one of the samples (PAS18) well within error (Figure V.7). Correlation coefficients of the fit of regressions are reported in Table V.5. There is no observable geographic or lithologic trend to explain the primary variation observed in δD values. In the following section, we determine the isotopic composition of the fluids from which the clay minerals grew and the degree of fluid source mixing.

Table V.4: Stable hydrogen isotope measurements

Sample	Fraction	Wt% H_2O	δD (‰)	Sample	Fraction	Wt% H_2O	δD (‰)
MDMS1	C	5.58	-67	**PABF22**	C	4.39	-65
	C	5.60	-67		C	4.39	-66
	MC	6.41	-71		MC	5.08	-64
	MC	6.40	-70		MC	5.10	-64
	M	6.91	-72		M	5.45	-65
	M	6.94	-71		M	5.42	-66
	MF	7.35	-75		MF	6.50	-74
	MF	7.35	-75		MF	6.47	-75
	F	8.08	-77		F	6.93	-74
	F	8.21	-77		F	7.00	-73
MDRH3	C	4.92	-68	**PADS24**	C	5.53	-72
	C	4.93	-68		C	5.55	-71
	MC	5.87	-65		MC	6.68	-66
	MC	5.87	-64		MC	6.63	-66
	M	7.12	-67		M	7.11	-71
	M	7.17	-67		M	7.21	-69
	MF	8.14	-73*		MF	9.11	-78
	MF	8.08	-68*		MF	9.12	-78
	F	9.25	-71		F	-	-
	F	9.29	-72		F	-	-
MDMcK4	C	5.32	-62	**PAWC25**	C	4.25	-68
	C	5.32	-64		C	4.22	-68
	MC	6.39	-62		MC	5.38	-72
	MC	6.41	-63		MC	5.44	-70
	M	7.30	-65		M	6.58	-72
	M	7.40	-64		M	6.55	-72
	MF	8.68	-70		MF	7.71	-76
	MF	8.64	-67		MF	7.70	-76
	F	9.11	-70		F	8.74	-66
	F	9.04	-67		F	8.93	-68
WVOS6	C	5.59	-66	**PARS26**	C	4.08	-63
	C	5.69	-66		C	4.09	-62
	MC	6.00	-65		MC	4.89	-67
	MC	6.02	-65		MC	4.79	-67
	M	6.45	-64		M	5.89	-67
	M	6.46	-65		M	5.77	-67
	MF	7.64	-68		MF	6.95	-79
	MF	7.69	-70		MF	6.92	-78
	F	8.47	-75		F	7.90	-79
	F	8.58	-72		F	7.80	-80
WVMcK7a	C	5.11	-64	**PAF28**	C	5.72	-62
	C	5.11	-64		C	5.71	-63
	MC	5.94	-66		MC	6.32	-62
	MC	5.76	-65		MC	6.31	-62
	M	6.83	-69		M	6.67	-65
	M	6.76	-68		M	6.60	-64
	MF	7.89	-74		MF	6.92	-70
	MF	7.82	-72		MF	6.95	-70
	F	7.95	-85		F	7.79	-72
	F	7.83	-83		F	7.77	-71

Table V.4: Stable hydrogen isotope measurements

Sample	Fraction	Wt% H_2O	δD (‰)	Sample	Fraction	Wt% H_2O	δD (‰)
WVDS9	C	5.60	-62	**PARSBE31**	C	4.65	-68
	C	5.60	-62		C	4.64	-70
	MC	6.49	-61		MC	5.72	-70
	MC	6.50	-62		MC	5.70	-70
	M	7.59	-66		M	7.21	-73
	M	7.60	-66		M	7.19	-72
	MF	8.62	-75		MF	8.32	-81
	MF	8.62	-73		MF	8.39	-82
	F	9.86	-77		F	9.12	-91
	F	9.94	-76		F	9.29	-92
WVDM10	C	5.48	-66	**PAJF32**	C	4.83	-67
	C	5.49	-64		C	4.81	-65
	MC	6.19	-65		MC	5.76	-64
	MC	6.23	-62		MC	5.77	-66
	M	6.64	-61		M	6.35	-71
	M	6.55	-62		M	6.40	-71
	MF	7.35	-59		MF	7.12	-79
	MF	7.38	-60		MF	7.13	-79
	F	8.97	-58		F	7.59	-82
	F	8.99	-61		F	7.58	-84
WVDS11	C	5.58	-67	**PARH33**	C	5.49	-81
	C	5.67	-69		C	5.54	-83
	MC	7.01	-64		MC	6.52	-77
	MC	7.06	-67		MC	6.52	-76
	M	8.88	-64		M	7.55	-76
	M	8.86	-62		M	7.50	-76
	MF	10.65	-62		MF	9.08	-79
	MF	10.68	-59		MF	9.10	-80
	F	12.12	-65*		F	10.11	-77
	F	12.03	-60*		F	10.37	-76
MDWC12	C	5.26	-72	**PARS35**	C	4.56	-57*
	C	5.27	-72		C	4.53	-62*
	MC	5.89	-74*		MC	5.55	-62
	MC	5.88	-70*		MC	5.48	-62
	M	6.27	-67		M	6.94	-65
	M	6.20	-66		M	6.96	-63
	MF	7.81	-87		MF	7.56	-66*
	MF	7.71	-85		MF	7.64	-70*
	F	9.04	-93		F	7.28	-60
	F	9.02	-91		F	7.27	-59
MDWC13	C	4.07	-69	**PABF36**	C	4.83	-81
	C	4.07	-68		C	4.91	-80
	MC	5.23	-68		MC	6.03	-83
	MC	5.25	-67		MC	6.03	-83
	M	6.38	-71		M	7.51	-86
	M	6.41	-69		M	7.52	-85
	MF	7.47	-77		MF	8.76	-90
	MF	7.43	-77		MF	8.80	-90
	F	7.52	-70		F	9.26	-90
	F	7.66	-72		F	9.29	-90

Table V.4: Stable hydrogen isotope measurements

Sample	Fraction	Wt% H_2O	δD (‰)	Sample	Fraction	Wt% H_2O	δD (‰)
MDBF14	C	5.40	-59	**PARH37**	C	5.26	-63
	C	5.45	-60		C	5.30	-63
	MC	5.72	-59		MC	5.99	-62
	MC	5.73	-59		MC	5.96	-62
	M	6.14	-62		M	6.82	-63
	M	6.10	-62		M	6.83	-63
	MF	7.53	-76		MF	8.04	-75
	MF	7.54	-78		MF	8.04	-74
	F	10.27	-87		F	8.33	-67
	F	10.36	-86		F	8.43	-68
MDMcK16	C	4.71	-62	**PASS40**	C	4.48	-66
	C	4.74	-63		C	4.53	-68
	MC	5.68	-59		MC	5.46	-66
	MC	5.63	-61		MC	5.46	-66
	M	6.44	-64		M	6.50	-70
	M	6.46	-64		M	6.44	-70
	MF	7.27	-70*		MF	7.91	-78
	MF	7.36	-74*		MF	7.80	-78
	F	9.79	-79		F	8.84	-75
	F	9.68	-78		F	8.94	-77
PAS18	C	5.37	-72	**PAWC42**	C	3.80	-56
	C	5.35	-71		C	3.75	-54
	MC	6.09	-72		MC	4.92	-59
	MC	6.24	-71		MC	4.91	-59
	M	7.22	-80*		M	6.19	-64
	M	7.16	-76*		M	6.15	-65
	MF	8.75	-90*		MF	7.80	-76
	MF	8.57	-85*		MF	7.79	-78
	F	9.76	-93		F	9.50	-85
	F	9.72	-93		F	9.64	-85
PADS19	C	5.64	-69				
	C	5.60	-71				
	MC	8.91	-54*				
	MC	8.86	-58*				
	M	10.12	-57				
	M	10.11	-59				
	MF	14.49	-58				
	MF	14.52	-58				
	F	~~33.39~~	~~-213~~				
	F	~~35.48~~	~~-364~~				

*Error between duplicates is >3‰
~~xx~~ measurements not used due to high water content

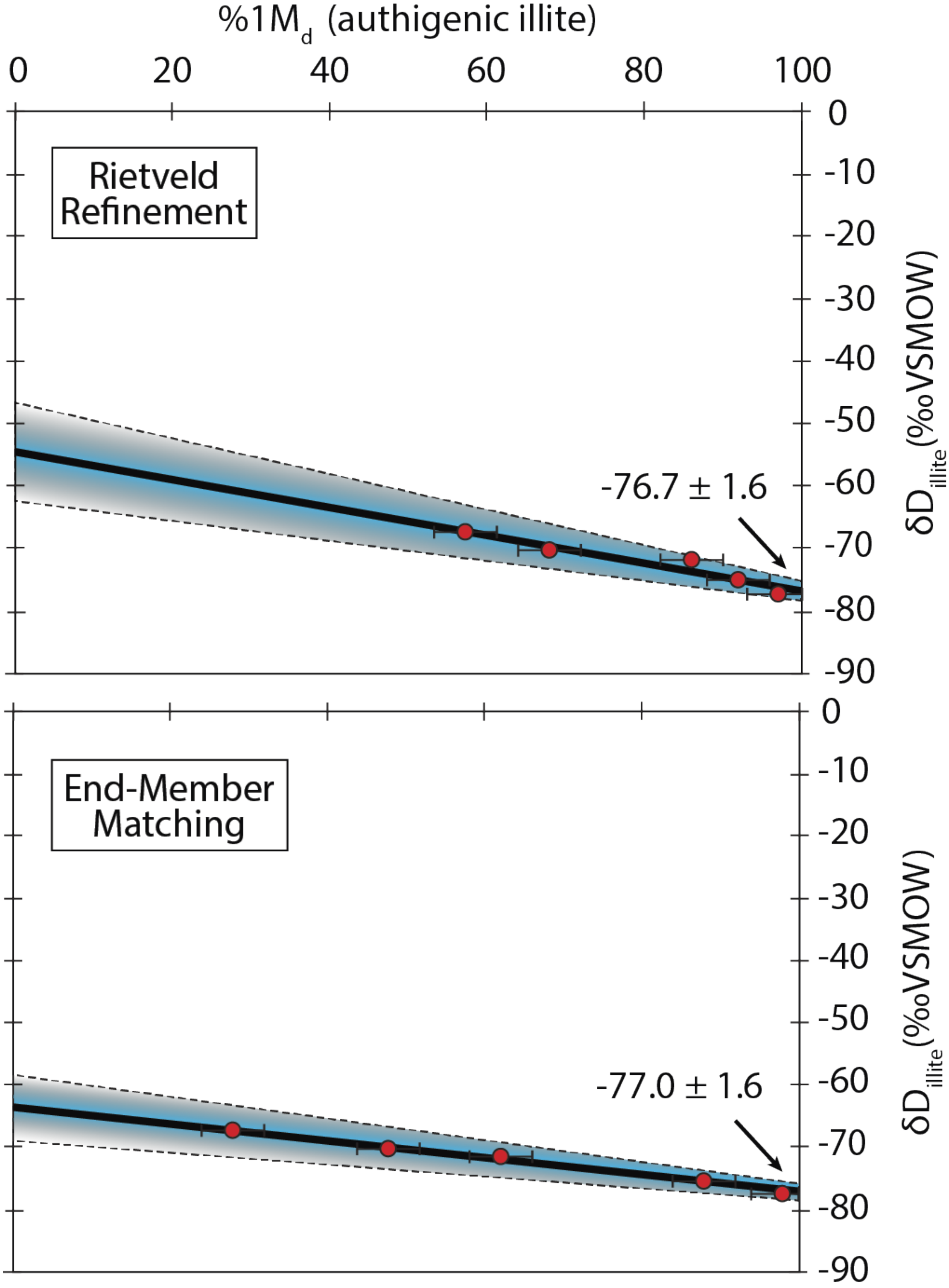

Figure V.6: York-regression results for sample MDMS1 showing the δD intercept and error window at 100% authigenic illite for each method. Though there are differences in the %1M$_d$ estimates with each quantification method, the finest samples are nearly always 95% 1M$_d$ or greater, providing a strong constraint on the composition of 100% 1M$_d$ by essentially 'anchoring' the intercept values.

Table V.5: Stable isotopic composition of authigenic illite end-member

Sample	δD intercept Rietveld Refinement (‰ VSMOW)	R^2	δD intercept End-Member Matching (‰ VSMOW)	R^2	δ^{18}O fine (±0.2‰ VSMOW)
MDMS1	-76.7 ± 1.6	0.902	-77.0 ± 1.6	0.991	16.8
MDRH3	-70.5 ± 1.5	0.455	-71.4 ± 1.6	0.718	-
MDMcK4	-67.8 ± 1.3	0.719	-69.4 ± 1.7	0.877	-
WVOS6	-73.1 ± 3.7	0.478	-72.3 ± 1.7	0.829	-
WVMcK7a	-77.3 ± 1.8	0.428	-80.4 ± 1.7	0.778	15.7, 15.6
WVDS9	-77.1 ± 1.9	0.839	-76.6 ± 1.6	0.954	14.5
WVDM10	-59.0 ± 1.7	0.762	-59.1 ± 1.4	0.964	-
WVDS11	-61.6 ± 1.3	0.875	-61.2 ± 1.4	0.881	-
MDWC12	-95.6 ± 3.0	0.643	-91.0 ± 1.9	0.680	16.9
MDWC13	-72.3 ± 1.2	0.274	-75.4 ± 2.0	0.465	-
MDBF14	-85.1 ± 2.0	0.897	-85.4 ± 1.8	0.937	16.8
MDMcK16	-77.0 ± 1.7	0.907	-80.8 ± 2.3	0.857	17.5
PAS18	-88.2 ± 1.5	0.714	-92.8 ± 1.7	0.964	14.4, 13.9
PADS19	-52.0 ± 3.0	0.814	-55.8 ± 1.5	0.759	-
PABF22	-70.6 ± 1.5	0.206	-73.1 ± 1.5	0.659	16.2
PADS24	-79.5 ± 2.4	0.970	-81.2 ± 3.3	0.619	-
PAWC25	-75.2 ± 6.7	0.055	-73.4 ± 2.7	0.084	17.1
PARS26	-65.6 ± 2.3	0.006	-65.3 ± 1.6	0.001	15.3
PAF28	-69.3 ± 1.5	0.373	-72.4 ± 1.8	0.958	15.0
PARSBE31	-81.2 ± 1.6	0.758	-83.6 ± 1.8	0.807	14.1
PAJF32	-67.0 ± 1.5	0.042	-65.8 ± 1.8	0.023	13.4
PARH33	-76.9 ± 1.5	0.125	-77.2 ± 1.7	0.052	14.4
PARS35	-83.7 ± 40.6**	0.105	-63.6 ± 2.0	0.105	17.5
PABF36	-90.8 ± 1.8	0.981	-92.0 ± 1.8	0.924	13.6
PARH37	-71.3 ± 1.6	0.723	-70.7 ± 1.6	0.534	15.4
PASS40	-76.1 ± 1.5	0.644	-79.4 ± 1.9	0.872	16.1
PAWC42	-83.0 ± 2.2*	0.837	-82.3 ± 1.8	0.858	-
SNPA7	-96.6 ± 2.0	0.947	-	-	14.5

*Used C, MC, M from Rietveld, and MF, F from end-member matching quantifications.
**Not used for fractionation calculations (see Discussion section).

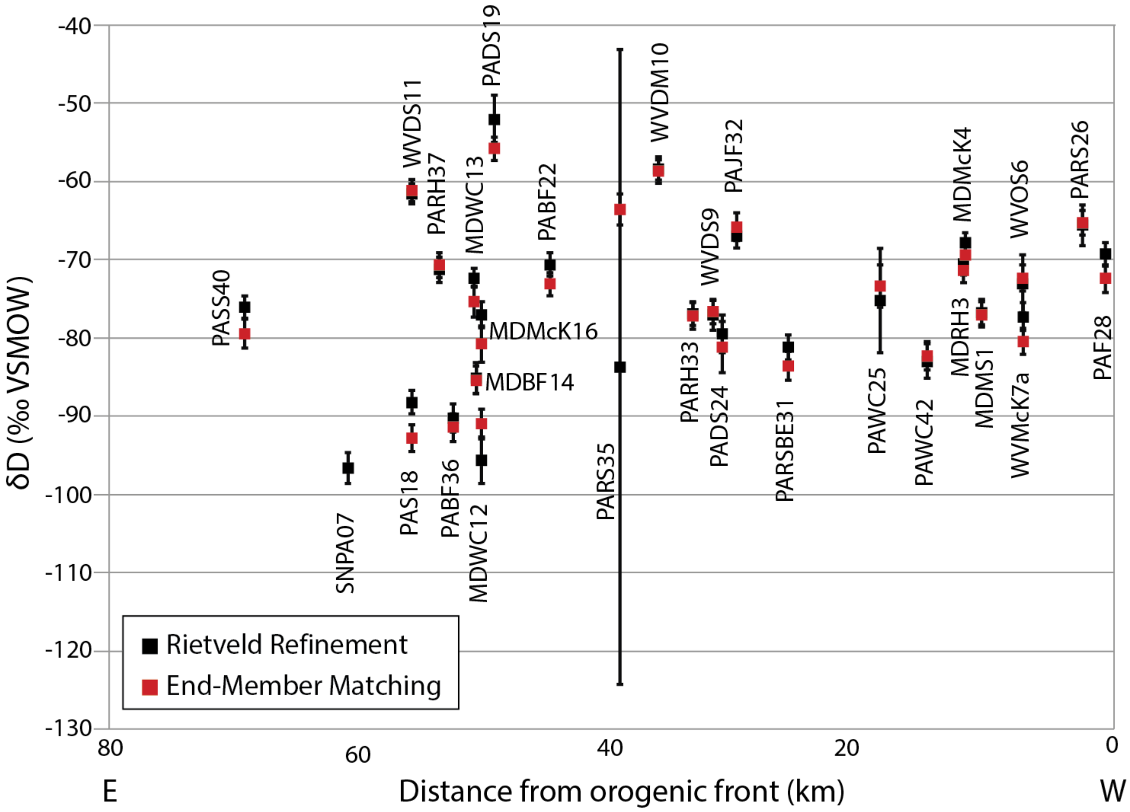

Figure V.7: Results of the regression analyses showing the δD distribution of authigenic illite plotted in order of their relative positions in the fold-thrust belt., with 100% representing the orogenic front. All samples except PAS18 overlap within error. The Rietveld regression results for PARS35 give unreasonably large errors (±40.6‰); this result is disregarded for future analyses in favor of the End-Member matching result.

Discussion

Temperature of Clay Growth

The stable isotopic composition of authigenic clay minerals depends both on the stable isotopic composition of the mineralizing fluids and the temperature at which the clays grow. Published temperature constraints indicate a possible range of mineral growth temperatures for the Valley and Ridge province. Conodont Alteration Indices (CAI) indicate maximum burial temperatures of ~190-230°C for the Central Appalachian Paleozoic section, suggesting a geothermal gradient of ~20-30°C/km and a burial depth of ~8 kilometers (Epstein et al., 1977; Harris et al., 1994; Repetski et al., 2008). Similar estimates of the paleo-geotherm (20-25°C) have been made from vein and fluid inclusion studies (e.g. Hearn et al., 1987; Evans and Battles, 1999; Evans et al., 2012), though they often point to maximum burial temperatures on the lower end of the CAI range. Evans and Battles (1999) completed a detailed study of veins and fluid inclusions in the Central Appalachians and identified three stratigraphically-separated fluid regimes. Based on salinity and homogenization temperatures of fluid inclusions, they documented trapping temperatures of 90°C-127°C in the Late Devonian Chemung and stratigraphically higher formations, 160-217°C in the Early Devonian Oriskany to lower Chemung formation, and 80-160°C, Late Ordovician Trenton to Oriskany. They also identified a high T fluid event (170-225°C) contained in the Late Ordovician Martinsburg formation. Additionally, Mesozoic apatite fission track ages in the upper stratigraphic units show that Paleozoic deformation temperatures in Devonian and stratigraphically lower units were likely >120°C (Roden and Miller, 1989; Roden, 1991; Blackner et al., 1994).

For fractionation calculations, we therefore use 120°C as a lower temperature bound for all samples. Upper bounds are interpreted based on fluid inclusion temperatures reported by Evans and Battles (1999). Using the average of the two regression results for each sample (except in the case of PARS35 where we use only the end-member method result), we calculate both upper and lower temperature fractionation for both hydrogen and (where available) oxygen using the fractionation equations of Capuano et al. (1992) and Sheppard and Gilg (1996), respectively (Table V.6). Our results (colored boxes, Figure V.8) overlap in their $\delta^{18}O$ values with the calculated fluid $\delta^{18}O$ values of Evans and Battles (1999) (yellow box, Figure V.8). Their study does not offer matching H data, which we are able to obtain from clays.

Identity of Mineralizing Fluid and Implications for Fluid Source Hypotheses

There are two main hypotheses regarding the nature of the mineralizing fluid in the Appalachian belt. Oliver (1986) proposed a long-distance migration of hot, deeply-sourced fluids toward the foreland, whereas Garven and Freeze (1984) suggested that the downward, topography-driven infiltration of meteoric fluids dominated fluid migration. These two end-member sources have observably different isotopic signatures. Appalachian metamorphic fluid is enriched in heavy isotopes relative to meteoric fluid and falls in the $\delta^{18}O$ range of 3 to 15‰ and the δD range of -20 to 10‰ (grey box, Figure V.8) (e.g., Schedl, 1993). In contrast, meteoric fluids in late Paleozoic times were much more negative in both hydrogen and oxygen isotopic composition. This is particularly true for the topography-driven infiltration hypothesis, which would have involved very light (negative) fluids, due to the altitude effect on orographic precipitation that depletes precipitation of heavy isotopes in precipitation at high elevations (Daansgard, 1964).

Based on climate simulation models, Poulsen et al. (2007) provide an estimate of $\delta^{18}O$ values in the range of -4 to -8‰ in low-elevation, low- to mid-latitudes during the late Paleozoic, with values as low as -17‰ at highest elevations and in the rainshadow of the Appalachian mountain core. Using the global meteoric water line ($\delta D = 8*\delta^{18}O + 10$) as an approximation to determine the corresponding δD component of paleo-precipitation, we get a wide range of possible δD values: ~-126 to -22‰.

Table V.6: Calculated stable istotopic compositional range of mineralizing fluid for each sample

Sample	Unit	Upper T bound (°C)	Min fluid (upper T)		Max fluid (120°C)	
			δD	$\delta^{18}O$	δD	$\delta^{18}O$
MDMS1	Clinton Group	160	-67	7.8	-56	5.1
MDRH3	Rose Hill Fmn	160	-61	-	-50	-
MDMcK4	McKenzie Fmn	160	-59	-	-48	-
WVOS6	Martinsburg Fmn	225	-76	-	-52	-
WVMcK7a	McKenzie Fmn	160	-69	6.7	-58	4.0
WVDS9	Devonian Black Shale	160	-79	5.5	-56	2.8
WVDM10	Devonian Mudstone	217	-61	-	-38	-
WVDS11	Devonian Black Shale	217	-64	-	-41	-
MDWC12	Wills Creek Fmn	160	-83	7.9	-73	5.2
MDWC13	Wills Creek Fmn	160	-64	-	-53	-
MDBF14	Bloomsburg Fmn	160	-75	7.8	-65	5.1
MDMcK16	McKenzie Fmn	160	-69	8.5	-58	5.8
PAS18	Rose Hill Fmn	160	-81	5.4	-70	2.7
PADS19	Devonian Black Shale	217	-56	-	-33	-
PABF22	Bloomsburg Fmn	160	-62	7.2	-51	4.5
PADS24	Devonian Black Shale	217	-83	-	-60	-
PAWC25	Wills Creek Fmn	160	-64	8.1	-54	5.4
PARS26	Reedsville Shale	160	-56	6.3	-45	3.6
PAF28	Bald Eagle Fmn	160	-61	6.0	-50	3.3
PARSBE31	Reedsville Shale	160	-72	5.1	-62	2.4
PAJF32	Juniata Fmn	160	-56	4.4	-46	1.7
PARH33	Rose Hill Fmn	160	-67	5.4	-56	2.7
PARS35*	Reedsville Shale	160	-54	8.5	-43	5.8
PABF36	Bloomsburg Fmn	160	-81	4.6	-71	1.9
PARH37	Rose Hill Fmn	160	-61	6.4	-50	3.7
PASS40	Bloomsburg Fmn	160	-68	-	-57	-
PAWC42	Wills Creek Fmn	160	-73	-	-62	-
SNPA7	Rose Hill Fmn	160	-87	5.5	-76	2.8

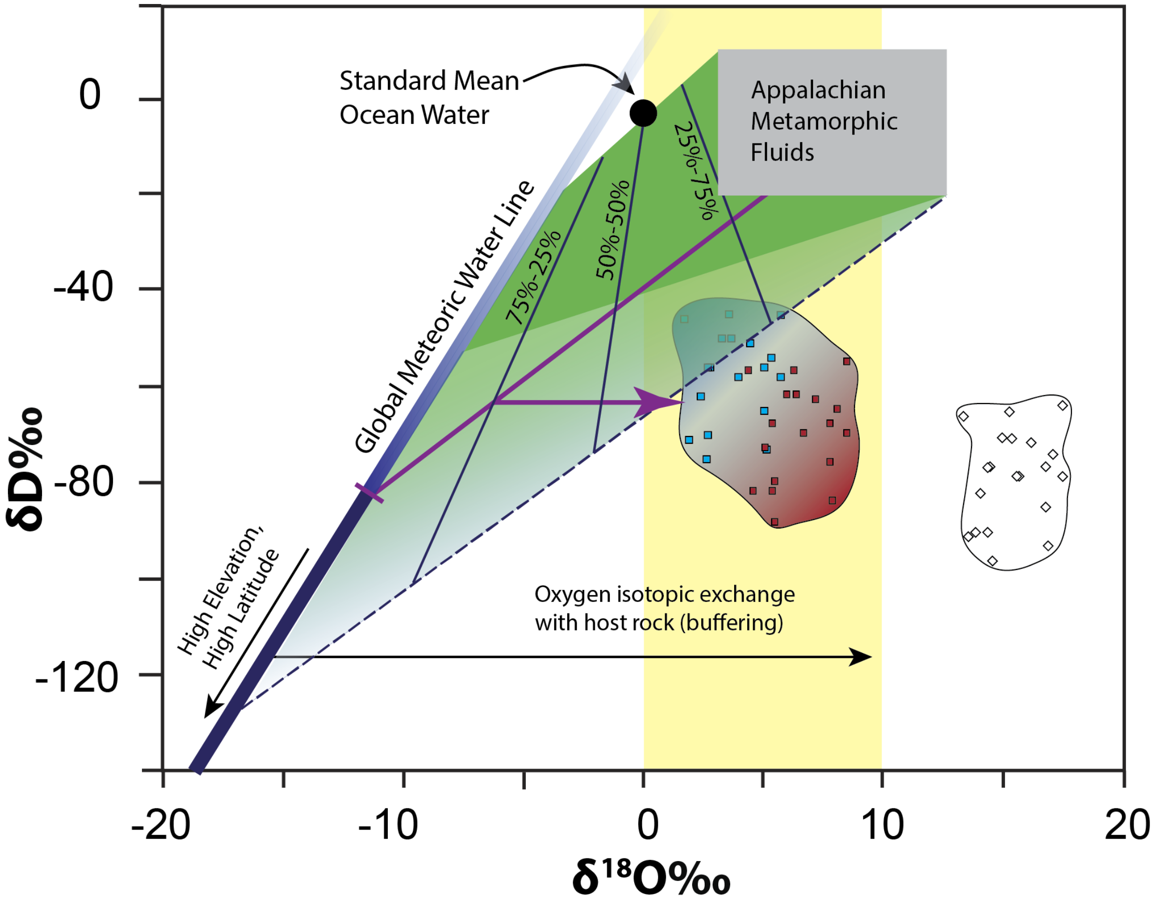

Figure V.8: Schematic diagram showing the isotopic composition of major fluid fields involved in Appalachian deformation along with our clay data. Clay data are shown in the white outlined field with specific samples shown in white diamonds. High T (red squares) and Low T (blue squares) fluid fractionation calculations from clay data are shown and outlined in a red-to-blue shaded field. This field is overlapped by a yellow bar, which represents the oxygen isotopic composition of vein-mineralizing fluids reported by Evans and Battles (1999). The green polygon shows the region of mixing between Appalachian metamorphic fluids (grey box) and meteoric water (indigo line)—the darker green shows a region of mixing with primarily low-elevation meteoric fluid, whereas the shaded green box shows a region of mixing with mid- to high-elevation meteoric fluid. Approximate mixing lines are illustrated within that polygon to show the relative proportion of each fluid required to create a fluid of a specific composition. Though the low temperature end of our fluid field does overlap slightly with the mid-to-high-elevation meteoric water/metamorphic fluid mixing polygon, much of it does not, suggesting that oxygen buffering with the host rock occurred prior to illite growth. The purple lines show one possible scenario in which the mineralizing fluid could have been made: Mixing of metamorphic fluid with mid-elevation meteoric fluid in a 25%-75% ratio, paired with a degree of buffering of the resulting fluid (right-pointing arrow).

The low δD values of the mineralizing fluid we determine necessitates the input of moderate to high-elevation meteoric or surface-sourced fluid as one component. However, it is difficult to ascribe a narrow set of δD values to the end-member meteoric fluid from the wide range of possible mixing ratios. For instance, beginning with the mixing of the two end-member components—Appalachian metamorphic fluid and unevolved meteoric fluid—we would expect the resultant mineralizing fluid to have an isotopic composition that falls within the range of isotopic values shown by the green polygon (Figure V.8). If low-elevation fluids dominated the meteoric source, we would expect the isotopic values to fall in the dark green portion of the wedge, whereas if higher elevation or orographic precipitation was a major component, we would expect fluid value to fall in the lighter shaded portion of the polygon. Though a small portion of our fluid estimates based on lowest temperature fractionation (blue boxes) do fall within the latter region, the majority do not, and none of the high temperature fractionation derived estimates (red boxes) fall within this region. This indicates that processes other than mixing of fluid sources occurred to modify the isotopic composition of the mineralizing fluid.

Using the δD signatures of the calculated fluid and their mixing sources we can approximate the proportion of each end member fluid necessary to contribute to create the isotopic composition of the fluids involved in illite precipitation. In order to determine the minimum amount of meteoric fluid necessary to create the deformation fluid, we consider the minimum boundary of the δD composition of the metamorphic fluids ($\delta D_{metamorphic}$ ~-20‰ VSMOW) and an extreme end member for high-elevation meteoric fluids ($\delta D_{meteoric}$ ~-120‰ VSMOW). Mathematical mixing these two end-members (Formula 2) reveals the required mixing of the two end member fluids where x equals the proportion of meteoric fluid required and δD_{hdf} represents the hydrogen isotopic composition of the hypothetical deformation fluid.

Eq. 2. $$\delta D_{hdf} = \delta D_{meteoric} * x + \delta D_{metamorphic} * (1 - x)$$

Calculations reveal that 19% or 56% input from high elevation meteoric fluids are required to create the δD composition of the maximum (-43‰) and minimum (-87‰) calculated fluid δD compositions, respectively. Three of the Devonian strata samples for which we do not have $\delta^{18}O$ measurements had maximum δD values of between -33 and -41‰, suggesting less input from meteoric fluids, but at very minimum still necessitating 10% high elevation meteoric fluids. Using a higher value for the meteoric source (for example -80‰) to complete the same calculations would suggest a larger input from meteoric fluid sources than the -120‰ estimate (with necessary input of meteoric fluid in that case being 29 to 84%). So, we expect at the very minimum ≥10% and likely ≥20% meteoric fluid input from moderate to high elevation sources (or a larger proportion from lower elevation sources). This also implies that there is the possibility that large amounts (up to 80%) of metamorphic fluids make up proportions of the deformational fluids in some Central Appalachian structures. The mixing of fluids sources is similar to what was described for the Canadian Cordillera in Chapter IV. However, in contrast to that study, the fluids here do not fall on the mixing line (or mixing region) between the two end member fluid sources, indicating that other processes in the crust have modified the isotopic composition of the mineralizing fluid.

Since the mineralizing fluid isotopic composition in general has more positive $\delta^{18}O$ values, we conclude that any involved meteoric fluids must have undergone a degree of oxygen exchange with the host rock prior to their incorporation into the fold-thrust belt. Whole rock host rock $\delta^{18}O$ compositions from the Central Appalachian fold-thrust belt range from ~15 to 25‰VSMOW (Evans and Battles, 1999). Therefore, if meteoric fluid was a dominant source ($\delta^{18}O < 0$‰), those fluids would have had to undergo significant oxygen isotopic buffering during their migration through the fold-thrust belt in order to reach the calculated orogenic fluid composition. Based on the extreme elevation and regionally extensive nature of the Paleozoic orogenic belt, we find it more plausible that moderate to high-elevation meteoric fluids, rather than low-elevation fluids, comprised an important component of the deformational fluids. This suggests that high-elevation fluids ($\delta^{18}O < -10$‰) traveled through rock units of the orogenic system as they infiltrating to depth (higher T), before being expelled through the foreland fold-thrust belt. If the original meteoric fluids were low to mid-elevation fluids the same is true; however, less isotopic exchange would be required for the fluids to reach their final oxygen isotopic composition. Unfortunately, because we are unable to firmly constrain the original composition or volume of the meteoric fluid or the amount of mixing of meteoric and metamorphic fluids, and because cannot trace the exact migration pathway of the high-elevation fluids or know the isotopic composition of the rock units the fluid was in contact with, we are unable to quantify the amount of buffering required to reach the final composition of the fluid.

The purple lines in Figure V.8 show one possible example of how the orogenic fluid could have been derived. Beginning from a 75%-25% mixture of moderate- to high-elevation meteoric fluid (~δD=-86‰, $\delta^{18}O$=-12‰) and an average metamorphic fluid

(~δD=-2‰, $\delta^{18}O$=9‰), a horizontal arrow shows the direction and magnitude of isotopic buffering required to reach the field of orogenic fluids.

Conclusions

Based on the O-H isotope composition of authigenic clays we argue that meteoric input was at least ~25% in fluids of the central Appalachians in latest Paleozoic times. This involvement of meteoric fluids implies that topography/gravity driven infiltration of meteoric fluids occurred prior to their involvement in fold-thrust belt deformation, supporting the hypothesis by Garven and Freeze (1984). Thus, even in compressional environments, the bulk permeability of the crust is high enough to allow the downward infiltration of fluids at hydrostatic pressures. The oxygen buffering of the fluid implies it interacted with a large volume of rock during its migration history, perhaps originating as high-elevation precipitation.

Metamorphic fluid signatures in the rock record suggest that gravity-driven fluid migration was not the only process acting on Alleghanian fluids. Metamorphic fluid release from the orogenic core likely continued through the late Permian and into the Early Triassic, as indicated by various thermochronometers along the orogenic belt (Dallmeyer, 1982; Farrar, 1985; Wintsch et al., 1992). High temperatures in the orogenic core would have promoted continued down-temperature fluid flow towards the foreland belt and basin well into the Early to Middle Triassic period.

The $^{40}Ar/^{39}Ar$-ages of authigenic illitic material indicate a prolonged period of clay growth that occurred both during and after the peak Alleghanian deformation. Because these clays grew in part from metamorphic fluids, we conclude that the orogen experienced an extended period of metamorphism for several tens of millions of years following peak orogenic conditions. The combination of two fluid sources implies that both temperature-driven metamorphic fluid migration and topography-driven, meteoric fluid infiltration were contributing processes to the movement of fluids from the orogenic core toward the foreland fold-thrust belt and foreland basin.

Acknowledgements

The authors would like to acknowledge several individuals and funding agencies who contributed to this project. First, thanks to Lindsay Abdale for her help in collecting and preparing samples for this study. Additionally, we would like to thank Chris Hall for his work involving dating and re-dating of our samples, as well as helpful discussion determining the required correction factor for total gas ages. Austin Boles and Jasmaria Wojtschke are acknowledged along with Zhongrui Li for their work in setting up and calibrating the EMAL Rigaku Diffractometer for Rietveld analyses. Thanks also Benita Putlitz and Selena Galdini for their help and guidance in the stable isotope lab at UNIL. Analytical funding for this project was provided by student research grants to Lynch from the Geological Society of America, and Rackham Graduate School, the International Institute, and the Turner Fund at the University of Michigan. Clay research at the University of Michigan is funded by the NSF, most recently under grant EAR-1629805.

Chapter VI. Conclusions

Geofluids play a central role in meditating deformation and transporting chemical species in crustal rocks, allowing slip on otherwise unfavorably oriented fault surfaces and the deposition of secondary minerals, including economic deposits. Isotopic studies of radiometrically dated, secondary clay minerals in fold-thrust belts offer a powerful technique for constraining the origins and history of these fluids. As this dissertation shows, clay minerals are robust recorders of past fluid characteristics in low-temperature settings, allowing us to determine both the primary sources of geofluids and the processes that occur during mountain building.

Clay minerals as stable isotope recorders

Integrated isotopic studies of clay minerals offers opportunity to delve into the ancient fluid histories of upper crustal rocks. With the ability to measure hydrogen isotopic composition, as well as oxygen isotopic composition, clay minerals make a particularly powerful complement to most methods used to study fluid in the crust that focus oxygen only. As we consider only the oxygen isotopic composition of the various crustal reservoirs (Figure VI.1a), we identify two challenges: first, there is significant overlap between reservoirs, and, second, only *very* negative $\delta^{18}O$-values indicate domination by meteoric fluids. As we showed, a major issue with this fact is that interaction of the fluids with the rock reservoir buffers their oxygen isotopic composition, shifting their $\delta^{18}O$-values towards more positive values. This causes the fluids to lose their original isotopic signature such that even if highly negative meteoric fluids dominated the fluid system, the secondary minerals no longer preserve information regarding the characteristics of the source, but rather they record the oxygen isotope signatures of the rock with which they interacted.

Clays are among the few mineral species that are formed at low-temperature in response to fluid activity. Studies of hydrogen isotopes of clays allows us to address the O-buffering issue, since hydrogen rock reservoir is not as extensive as that of oxygen and, therefore, isotopic buffering is not an important process. Though hydrogen isotope space also have overlapping source fields (Figure VI.1b), hydrogen fluid signatures that are less than ~-60‰ VSMOW require input from some meteoric, or surface-originating fluid source. Thus, when we add H analysis to the isotopic proxies of a mineral, we are much better able to characterize the fluid sources involved in their formation and associated geologic processes. Furthermore, the ability to date illitic (K-rich) clay mineral growth using the $^{40}Ar/^{39}Ar$ methods, also determines the timing of fluid activity.

Geofluids in fold-thrust belts

As we have shown in this dissertation, clays are reliable recorders of their fluid history, documenting both the isotopic composition and the timing of fluid involvement in crustal processes. Their low-temperature formation and stability makes them especially useful for studying shallow crustal fluids in evolving crust. This utility makes them ideal for studies of fold-thrust belt fluids and the continuing debate of their origin. One important outcome of the dissertation research is that, contrary to the widely held opinion that fold-thrust belt fluid regimes are dominated by deep-sourced metamorphic fluids, meteoric fluids play a major, sometimes even dominating role in the fluid history of fold-thrust belts. In **Chapter II**, clay analysis based solely on hydrogen isotopes showed that

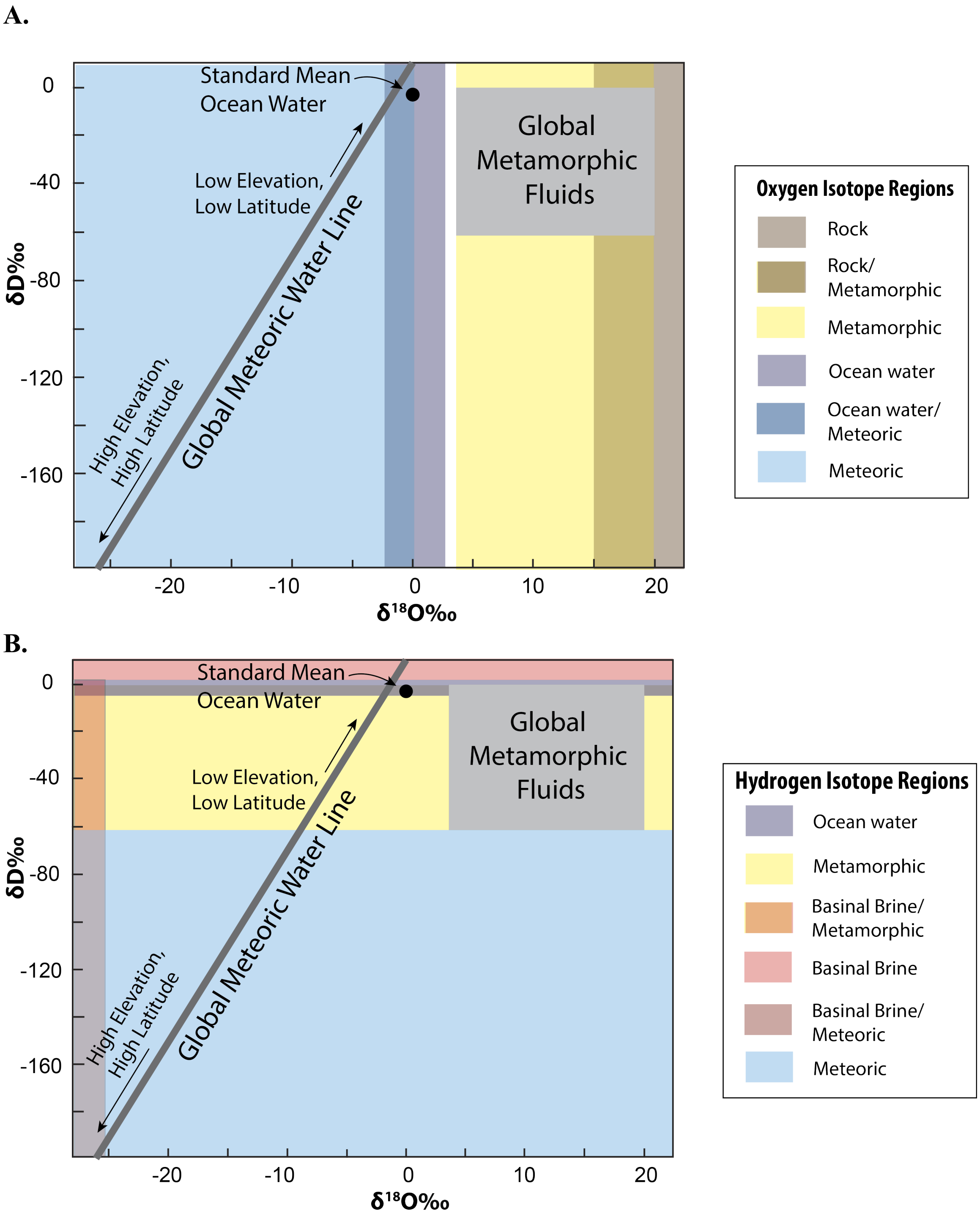

Figure VI.1: Stable isotope plots showing the distribution of regions dominated by different geofluids. (A) shows the overlap of fluid fields if only oxygen isotopes are considered, (B) shows the overlap of fluid fields if only hydrogen isotopes are considered. When two fluid fields overlap, there is uncertainty as to which fluid is the main fluid source.

fault rock fluids in the Argentinian Andes foreland belt included surface-sourced fluids. In **Chapter III**, hydrogen analyses on secondary clay minerals in the US Rockies also show significant involvement of surface-sourced fluid. In this chapter, isotopic signatures were directly correlated with ancient meteoric proxy records, further supporting the role of surface sourced fluids in fold-thrust belts.

The research in this dissertation also shows that in other cases there is considerable degree of mixing of fluids (Figure VI.2). Using paired hydrogen and oxygen isotopic analysis on clays allows us to quantify the amount of mixing of these fluid sources. As shown in the last two chapters, surface-sourced fluids are dominant in this mixture in some regions, whereas elsewhere they are equal or subsidiary mixtures. In **Chapter IV**, the spread of isotopic values of Canadian Cordilleran fluids indicate a mixing between high-latitude surface fluids and deeply-sourced metamorphic fluids in an approximate 50%/50% mix, with some fault structures hosting more meteoric (up to ~75%) and some hosting less (as low as ~25%). This shows that the hydraulic regime of a fold thrust belt is not laterally homogeneous, and that fluids find preferential pathways from source(s) to zones of mineralization. Insights from Appalachian rocks in **Chapter V**, reflecting a much older deformation environment, also support this observation.

Fluid source mixing is a variable contributor to the final isotopic composition of mineralizing fluids, but oxygen isotopic signatures reveal that there was an important amount of fluid-rock interaction that caused buffering of the oxygen isotopes. This buffering occurred along the fluid migration pathways, indicating that fluids were far-travelled from their source.

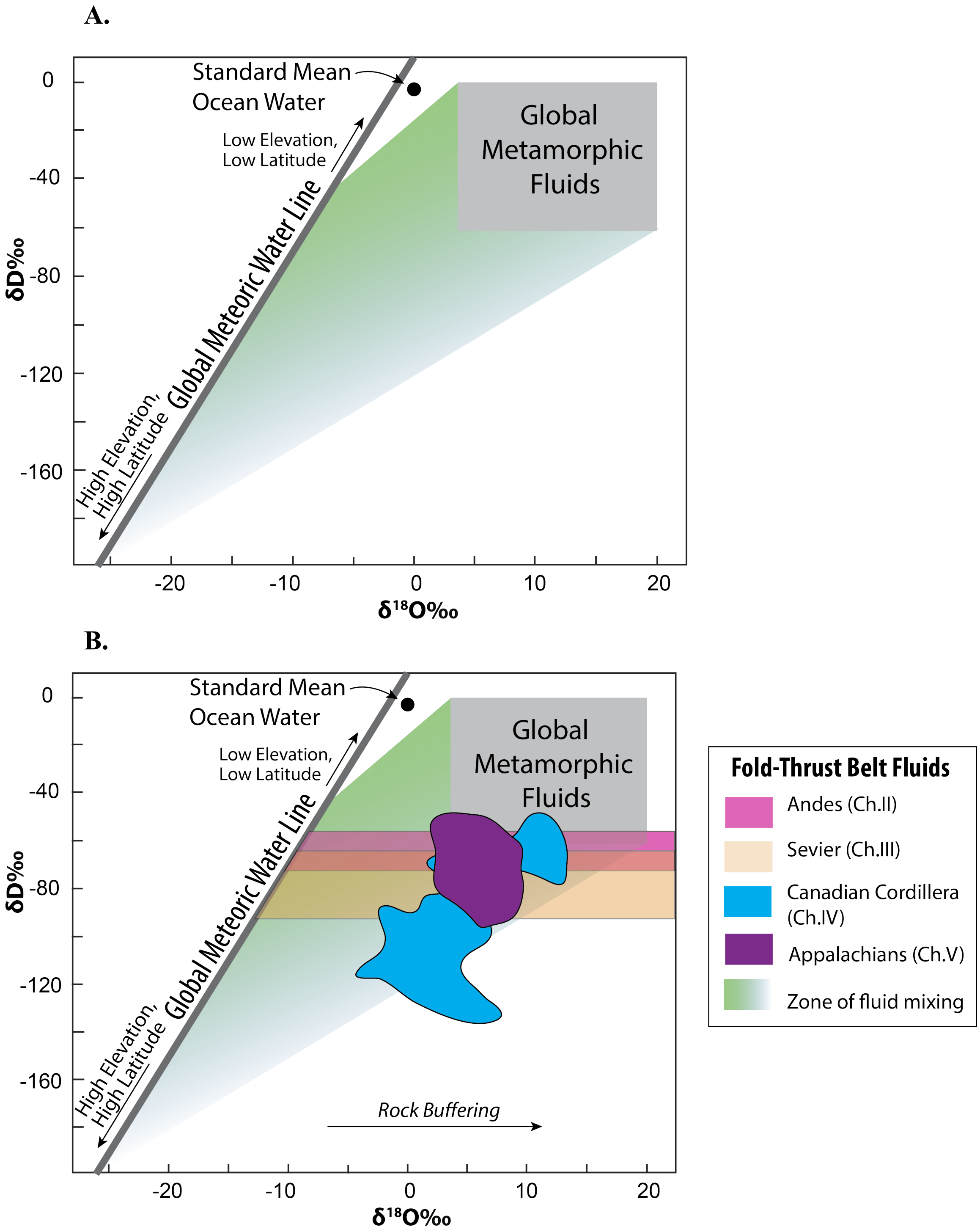

Figure VI.2: Schematic diagrams showing the isotopic composition of fold-thrust belt fluids studied in this dissertation. (A) shows the theoretical field of mixing between metamorphic and meteoric fluids in green. (B) shows the fluid compositions of study areas in Chapters II-V overlain on the zone of fluid source mixing, showing variable input from metamorphic and meteoric fluids. Note that studies in the Andean and Sevier foreland fold-thrust belts do not include O analysis, reflected by the horizontal bars. The horizontal arrow indicates the complication from rock buffering.

Fluid driving forces and their implications

The presences of *both* metamorphic and meteoric fluids in fold-thrust belts allows us to speculate about the relative roles of fluid driving forces in contractional orogens. As has long been argued, foreland fold-thrust belts represent a pathway for deeply-sourced metamorphic fluid escape to the surface; however, the distribution of metamorphic fluids is heterogeneous. This implies that fluids originating in the deep interior of mountain belts are likely to channelize along preferred pathways rather than distributing themselves evenly across all structures. Because of this, it is likely that channelized fluids effectively transport heat and dissolved chemical species over extended distances with only local effects on the host rock.

Due to the prevalence of meteoric/surface-sourced fluids in fold-thrust belts, we surmise that gravity is a major fluid diving force. Penetration of surface-sourced fluids to depth (suggested by oxygen isotope signatures in the Appalachian clays, for example: Chapter V) implies that fracture permeability of the high elevation mountain core and fold-thrust belt is high enough to allow downward infiltration of fluids. This also suggests that in orogenic cores, gravitational forces on surface-sourced fluids are sufficiently large to create source mixing. Thus, the fluid regime of an orogenic system is an open system, allowing the movement and mixing of different fluids throughout ongoing deformation. This is in contrast to the idea that fluids are locally sourced and compartmentalized, as is proposed for relatively undeformed, flat-lying sediments in foreland basins.

Considering the open-system behavior and multiple driving forces yields insights on the mechanical and chemical regimes of a fold-thrust belt system. The balance of two drivers (gravity infiltration and pressure-temperature gradient flow) and the two fluid volumes (surface-sourced and deeply-sourced) suggests that there may be a neutral zone of mixing between the fluids somewhere at depth within an orogenic system. Connolly and Podladchikov (2004) modeled such a zone of neutral buoyancy and fluid mixing to explain observed mid-crustal seismic reflectors in an approximately 1 km thick zone at a depth of 2-4 km below brittle-plastic transition. Such a zone would act as a barrier both for upward and downward fluid flow, allowing only lateral motion of fluids. In the case contractional fold-thrust systems, this lateral motion would be toward the lower temperature/lower pressure foreland section of the belt and associated foreland basin. Continued contraction and crustal thickening in the orogenic core may cause the dynamic uplift of this neutral buoyancy zone, allowing not only temperature/pressure driven lateral fluid flow, but also inducing gravity driven flow in these deeper crustal fluids, mimicking gravity driven flow of groundwater in the shallowest crustal reservoirs.

Other Directions

The ubiquitous involvement of surface fluids in fold-thrust belt stimulates interest for using clay mineral studies for extracting additional information about the nature of surface fluids. In **Chapter II**, hydrogen isotopic signatures in the Andes tracked regional aridification, suggested that geofluids that involve meteoric components may be used to track long-term climate changes within mountain belts. In **Chapter IV**, the very negative stable isotopic signatures of some of the fluids from the high-latitude region of the Canadian Cordillera indicate that clay stable isotopes may reflect predicted trends in meteoric precipitation with latitude—low latitudes yielding less negative isotopic signatures and high latitudes exhibiting more negative isotopic signatures. One difficulty with attempting to extract this secondary signal from the clay isotopic signatures is in quantifying the input from various sources over time. For instance, how can we determine if and how the ratio of metamorphic to meteoric fluid input into a single fault or in an orogenic system changes through time? And, how does the mixing of chemically and physically distinct fluid sources influence the timing of mineral growth? Regardless, clay mineral studies provide a powerful approach for probing the fluid history and conditions of the upper crust, broadening the already diverse fluid proxy toolbox that further characterizes ancient geofluid systems.

Appendices

Appendix A. Meteoric fluid infiltration in crustal-scale normal fault systems as indicated by $\delta^{18}O$ and $\delta^{2}H$ geochemistry and $^{40}Ar/^{39}Ar$ dating of neoformed clays in brittle fault rocks

Abstract

Both the sources and pathways of fluid circulation are key factors to understanding the evolution of low-angle normal fault (LANF) systems and the distribution of mineral deposits in the upper crust. In recent years, several reports have shown the presence of meteoric waters in mylonitic LANF systems at mid-crustal conditions. However, a mechanism for meteoric water infiltration to these mid-crustal depths is not well understood. Here we report paired $\delta^{18}O$ and $\delta^{2}H$ isotopic values from dated, neoformed clays in fault gouge in major detachments of the southwest United States. These isotopic values demonstrate that brittle fault rocks formed from exchange with pristine to weakly evolved meteoric waters at multiple depths along the detachment. $^{40}Ar/^{39}Ar$ dating of these same neoformed clays constrains the Pliocene ages of fault-gouge formation in the Death Valley area. The infiltration of ancient meteoric fluids to multiple depths in LANFs indicates that crustal-scale normal fault systems are highly permeable on geologic timescales and that they are conduits for efficient, coupled flow of surface fluids to depths of the brittle-plastic transition.

Introduction

Fluid flow in both individual faults and sets of faults in a given tectonic regime has been the subject of considerable interest for the past 30 years (e.g., Kerrich et al.,1984; McCaig, 1997; Gébelin et al., 2012; Menzies et al., 2014). Fluids in middle- and upper-crustal normal faults show a strong influence of variably evolved, meteoric-derived fluids (e.g., Fricke et al., 1992; Mulch et al., 2004; Swanson et al., 2012; Hetzel et al., 2015). These observations would require downward circulation of surface waters into the mid-crust, a physiomechanical process that is poorly understood (Connolly and Podladchikov, 2004; Person et al., 2007; Lyubetskaya and Ague, 2009). In addition to fluid pathways, fault zone minerals with a meteoric fluid origin can be used to make inferences about regional paleoelevations (e.g., Mulch et al., 2004; Gébelin et al., 2012, 2013). By contrast with normal fault systems, it is thought that fluids in thrust faults are dominated by upward circulation of deep basinal fluids, with minor contributions from evolved meteoric fluids in late stages of orogeny (e.g., McCaig et al., 1995; Trave et al., 2007; Sample, 2010).

Fluid-flow models have outlined a set of narrow permeability and topography conditions by which downward flow of meteoric-water–dominated waters might still occur (Person et al., 2007). Key to testing the feasibility of these fluid-flow models for LANFs is isotopic data from the upper and middle reaches of LANF systems. Isotopic studies of the upper and middle reaches of LANF systems, which extend from the surface to the middle crust, are few relative to the now data-rich mylonitic rocks. Stable isotopes have been employed in faults in carbonate-dominated sequences (e.g., Losh, 1997; Losh et al., 2005; Swanson et al., 2012), but relatively few LANFs occur in carbonate-dominated sequences relative to those in silicate-dominated upper-crustal sections.

Neoformed clay-rich fault gouges are a common feature of LANFs (e.g., Haines and van der Pluijm, 2012) and have been recognized to both dramatically reduce the frictional strength of fault zones (e.g., Carpenter et al., 2011; Haines et al., 2014) and document the age at which fault gouge formation occurred (Solum et al., 2005; Haines and van der Pluijm, 2008). The clay minerals that are neoformed in LANF gouge thus have a major influence on fault behavior, but their potential as recorders of upper-crustal fluid circulation in LANFs has not been broadly examined to date. Phyllosilicates are unusual silicate minerals in that they contain structural hydrogen in addition to the oxygen that is found in all silicates and thus permit analysis of both $\delta^{18}O$ and $\delta^{2}H$ on a single mineral phase, allowing for a more complete characterization of the exchanging fluid. The $\delta^{2}H$ value of the clay minerals preserves the initial source of the fluid until water-rock ratios become very low (water/rock <0.001; Menzies et al., 2014). By contrast, because all silicate minerals contain oxygen, the $\delta^{18}O$ value is strongly sensitive to the degree of wall-rock–fluid interaction (Sharp, 2005). An analysis of both isotopic ratios from the same mineral separate allows for an evaluation of both the initial source and any degree of wall-rock–fluid interaction of fluids exchanging with that mineral phase. Fluids with $\delta^{2}H$ <-80‰ and $\delta^{18}O$ <0‰ are generally interpreted to be of meteoric origin, while fluids with $\delta^{18}O$ >+5‰ and $\delta^{2}H$ >-80‰ are interpreted to be of metamorphic or igneous origin (Sheppard, 1986).

Illitic clays are common to many clay-rich gouges; they contain K, and retain Ar, permitting dating of clay growth in gouge by $^{40}Ar/^{39}Ar$ methods. We use the illite age analysis method, which utilizes $^{40}Ar/^{39}Ar$ dating in conjunction with quantitative X-ray diffraction (XRD) to determine the age of authigenic and detrital (cataclastically derived) clay mineral populations.

To investigate the fluid-flow system of LANFs in the U.S. Basin and Range province as a class of fault, we utilized a suite of samples that were characterized as part of a companion study of clay gouge mineralogy (Haines and van der Pluijm, 2012), which identified systematic patterns of clay mineral transformations in clay-rich fault gouges. These faults range from shallow-rooted structures (such as the Panamint Range–Front detachment) to LANFs that reached mid-crustal depths (e.g., the Ruby Mountains detachment). We isolated authigenic phyllosilicate minerals from both upper-crustal clay-rich fault gouges and mid-crustal metasomatic, chlorite-rich breccias from a suite of faults (Figure A.1) and analyzed $\delta^{18}O$ and $\delta^{2}H$ values of neoformed phases in order to investigate the composition of fluids from which they grew. A subset of these samples was analyzed to determine the age of neoformed clays, and thus, the timing of fluid infiltration.

Low-Angle Normal Faults and Faults Sampled

Low-angle normal faults (LANFs) are a special class of normal fault, first noted in the American Cordillera (Anderson, 1971; Wernicke, 1981) and now recognized globally (e.g., Collettini, 2011). These faults are unusual in that they have accommodated normal displacements of tens of kilometers and many slipped at dips below those predicted from conventional rock friction arguments (Axen, 2004; Haines and van der Pluijm, 2010). Many exposures of exhumed shallow-crustal LANFs have well-developed cm-thick to m-thick, clay-rich fault gouges that are dominated by neoformed clay minerals, predominantly illite, illite-smectite, and smectite. These neomineralized clays in fault gouge comprise the uppermost part of a suite of distinctive fault-related rocks in metamorphic core complexes (MCCs) that record progressive exhumation of footwall lithologies, often from pre-faulting mid-crustal depths. Many (but not all) LANF footwall exposures have clay gouges in direct contact with a distinctive greenschist-facies epidote + chlorite alteration of footwall metamorphic or igneous lithologies (Figure A.2A). This distinctive epidote + chlorite alteration can extend for tens of meters into the footwall, and, where brecciated, these rocks are lithified cataclasites, sometimes called "chlorite microbreccias" (Phillips, 1982; Selverstone et al., 2012). The fault rocks that are inferred to form at greatest depths are commonly quartzofeldspathic mylonites (formed at temperatures from 400 to 550 °C; Anderson, 1988; Mulch et al., 2007).

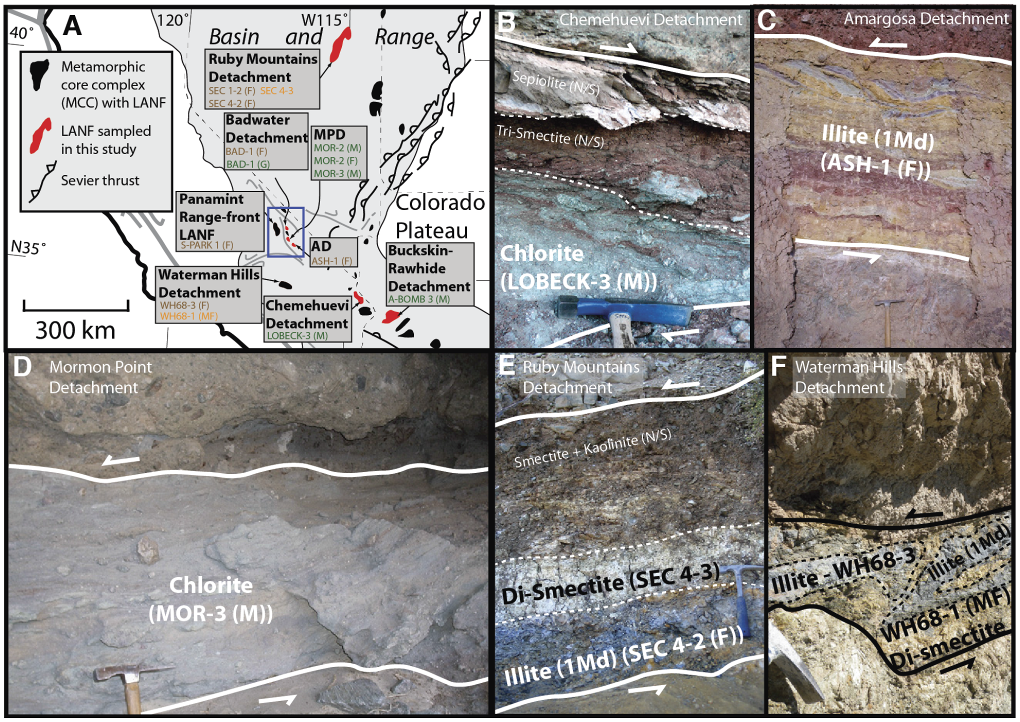

Figure A.1: (A) Map showing sampled low-angle normal faults (LANFs) together with principal tectonic elements in the southwestern United States. LANFs in the Death Valley area are abbreviated; MPD—Mormon Point detachment; AD—Amargosa detachment. Sample names are color coded by mineralogy to indicate the authigenic clay mineral in sampled gouge; brown—illite; orange—smectite; green—chlorite. Blue box shows area of Figure A.2. (B)–(F) Outcrop photos of selected LANF exposures sampled in this study. Dashed lines delineate mineralogically distinct layers within the gouge as identified by X-ray diffraction analysis (Haines and van der Pluijm, 2012). Dominant authigenic clay in gouge layer is shown in bold. N/S—layer not sampled. Solid lines show contact of gouge with hanging wall and footwall; arrows show sense of slip. (E) and (F) show outcrops where two mineralogically distinct layers from the same outcrop were analyzed. (E) is same exposure as "Secret-4" of Haines and van der Pluijm (2010). Please note: (F) in sample name indicates size fraction <0.05 mm (Stokes equivalent); (M) represents 0.2–0.05 mm size fraction.

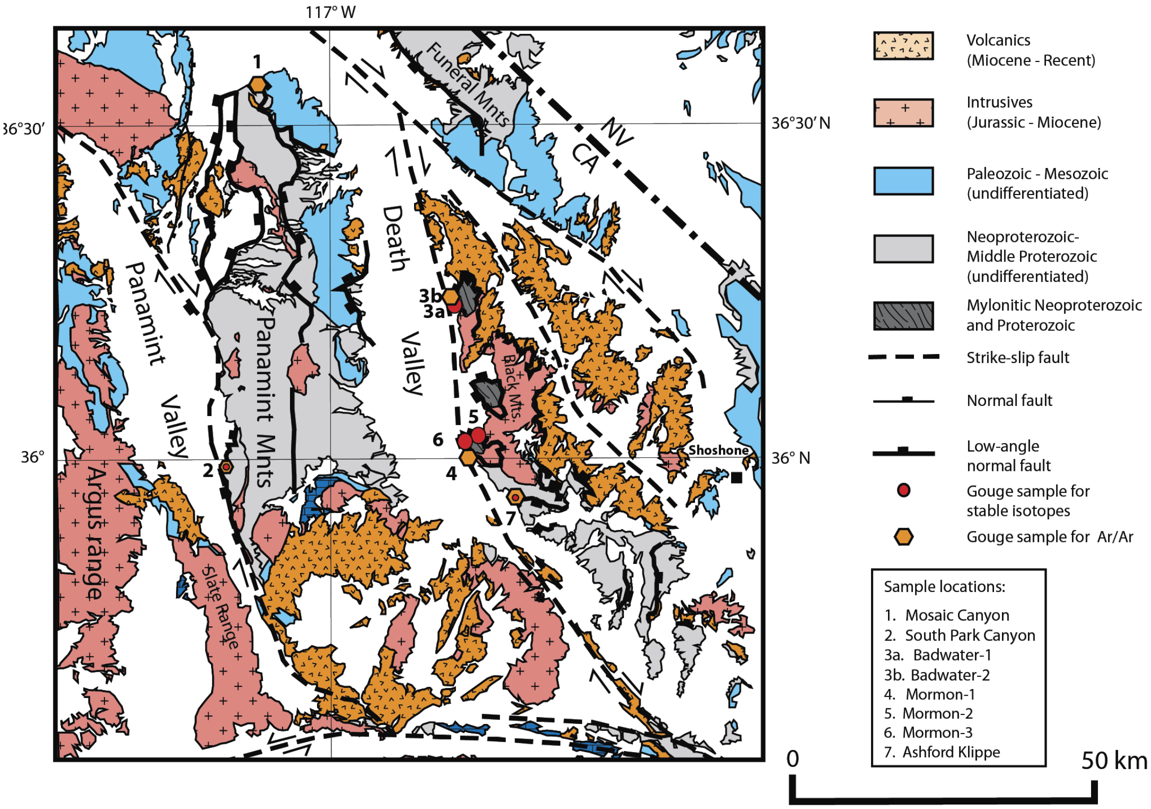

Figure A.2: Sketch geologic map of the Death Valley and Panamint Valley region of California, USA, showing regional geology and localities sampled. Redrawn after Sweetkind et al. (2001).

Fluid flow in LANF systems has been examined with numerous isotopic studies of the mid-crustal mylonitic fault rocks using both d18O and d2H on minerals and fluid inclusions (Lee et al., 1984; Wickham and Peters, 1990; Fricke et al., 1992; Wickham et al., 1993; Peters and Wickham, 1995; Mulch et al., 2004, 2007; Gébelin et al., 2011, 2012, 2015; Gottardi et al., 2011). The greenschist-facies microbreccias have also been studied, often in conjunction with the higher-temperature mylonites (Kerrich and Hyndman, 1986; Kerrich and Rehrig, 1987; Kerrich, 1988; Smith et al., 1991; Morrison, 1994; Nesbitt and Muehlenbachs, 1995; Morrison and Anderson, 1998). While many of these studies used d18O and d2H analyses, few performed both analyses on the same phase. Fluid circulation in LANFs in carbonate-dominated successions has been studied using carbonate veins formed in lower-temperature (30–300 °C) fault rocks (Losh, 1997; Losh et al., 2005; Swanson et al., 2012). The majority of these studies have documented low-d2H/low-d18O fluids, inferred to be of meteoric origin, although some (Smith et al., 1991) have documented predominantly igneous-dominated fluids, or the interaction of two (metamorphic and meteoric) fluid sources (Kerrich, 1988).

In recent years, d2H isotopic studies of neoformed micas in LANF mylonites have yielded very depleted (d2H <-100‰) values, interpreted to be indicative of (1) high-altitude meteoric fluid, (2) high-latitude meteoric fluid, or (3) a paleo-rain shadow (Mulch et al., 2004, 2007; Gottardi et al., 2011; Gébelin et al., 2011, 2012, 2015). The processes and pathways by which meteoric fluids of surface origin reach the mid-crust are controversial. Fluids migrating down a fault system will encounter unfavorable thermal and density gradients, and the buoyancy of hot waters at higher pressures is greater than that of colder waters, inhibiting downward flow (Connolly and Podladchikov, 2004; Lyubetskaya and Ague, 2009). In addition, mid-crustal rocks are widely assumed to lack the porosity and permeability to permit fluid flow at rates sufficient to prevent the very low water-rock ratios that would obscure the initial source of the fluid. Some studies, therefore, have suggested that isotopic evidence for meteoric fluids in mid-crustal lithologies is instead evidence of burial of pre-metamorphic fault rocks to mid-crustal depths and not actual incursion of meteoric fluids to mid-crustal shear zones (Clark et al., 2006; Raimondo et al., 2011, 2013). Person et al. (2007) presented a numerical model that suggested that a metamorphic core complex with a fracture-dominated flow system with a relatively narrow range of effective fault zone permeabilities (10-15 to 10-16 m2) and a crystalline basement wall-rock permeability

<10-17 m2 could explain the observed isotopic depletion of micas in fault zone mylonites at the Sushwap metamorphic core complex. Our data test the hypothesis that upper-crustal, brittle faults in LANF systems act as pathways by which 2H- and 18O-depleted meteoric fluids can reach the middle crust. To test this hypothesis, we obtained paired stable isotope measurements of oxygen and hydrogen from authigenic clay minerals (illite and smectite) and authigenic chlorite from a suite of eight LANFs (Figure A.1). A subset of clay gouges from the Death Valley region and the Ruby Mountains of Nevada was also dated to test the ancient origin of fluids that were responsible for clay neomineralization.

Neoformed Clay-Rich Gouges

Fault gouges and breccias, which are common in Cordilleran LANFs, form in the brittle regime (<300 °C), and are commonly assumed to be predominantly the result of physical processes, such as cataclasis (e.g., Sibson, 1977; Holland et al., 2006). In recent years, it has been recognized that many "brittle" fault zones are also chemically very reactive environments (Vrolijk and van der Pluijm, 1999; Solum et al., 2005) and that significant mineral transformations occur in fault gouge (Haines and van der Pluijm, 2012), affecting the frictional strength and permeability structure of these rocks. Neoformed clay minerals form in fault gouges at a temperature range of 50–180 °C and in faults with a variety of wall-rock compositions. The common clays forming in gouges are illite, formed from the alteration of fragmental mica or feldspar in gouge, and smectite. Smectite in fault gouge mostly forms by two discrete pathways—tri-octahedral smectite (saponite) forms by the alteration of cataclastically derived chlorite in gouge, whereas di-octahedral smectite (montmorillonite) forms from the alteration of fragmental acid volcanics and tuffs in wall rocks. A predictable relationship has been observed between wall-rock lithology, temperature, and clay mineral formation in clay-rich gouge (Haines and van der Pluijm, 2012). Because these clays are authigenic hydrous phyllosilicates, they exchange with both the oxygen and hydrogen in the infiltrating fluids, providing information on fluid sources and pathways.

Chlorite "Microbreccias"

Chlorite metasomatic alteration and brecciation of the footwall extending for meters to tens to hundreds of meters below the detachment fault surface are common features of low-angle normal faults associated with metamorphic core complexes (Crittenden et al., 1980; Kerrich, 1988). Chlorite alteration is found at all of the detachments sampled in this study that are thought to have evolved from mid-crustal shear zones (Badwater and Mormon Point turtlebacks, Buckskin-Rawhide detachment, Chemehuevi detachment; Figure A.1). The chlorite metasomatic alteration is nearly always developed in footwall rocks that are dioritic to granitic in composition. Mylonitic marbles that are locally present in the footwalls of the Black Mountains and that are intercalated with extensively chloritized gneisses are visually unaltered. The breccias contain a distinctive assemblage of chlorite ± epidote ± (titanite or rutile) ± feldspar ± calcite ± Fe-oxide that overprints mylonitic fabrics and imparts a distinctive greenish color to the rocks (Selverstone et al., 2012). Isotopic and fluid inclusion studies indicate the alteration results from the breakdown of biotite, amphibole, or anorthitic feldspar at greenschist-facies metamorphic conditions (300–350 °C, Kerrich, 1988; 350–520 °C, Morrison and Anderson, 1998; and 380–420 °C, Selverstone et al., 2012) by an influx of Fe-, Mg-, and Mn-rich meteoric (Morrison, 1994; Morrison and Anderson, 1998) or igneous fluids (Smith et al., 1991). The “microbreccias” are commonly cataclastically reworked as brittle, unconsolidated fault gouges. While at some exposures of LANFs, alteration of the metasomatic chlorite to lower-temperature tri-octahedral clays is significant, other outcrops locally preserve a cataclastically derived, chlorite-dominated gouge without evidence of significant alteration (e.g., Figures A.1B and A.1D; Haines and van der Pluijm, 2012). These unconsolidated gouges contain abundant chlorite cataclastically separated from the wall rock, permitting the chlorite to be separated by centrifugation and then analyzed.

Detachments Sampled

We sampled gouges from five suites of Cordilleran LANFs, comprising eight separate detachments: (1) The Ruby Mountains detachment in northern Nevada; (2) three detachments in Death Valley, California (Badwater detachment, Mormon Point detachment, and Amargosa detachment); (3) two detachments in the Panamint Mountains, west of Death Valley (Panamint Range–Front LANF and Mosaic Canyon detachment); (4) the Buckskin-Rawhide detachment in NW Arizona; and (5) the Waterman Hills detachment in southern California (Figures A.1 and A.2). Further description of sampled outcrops is given in Data Repository File DR1; geospatial data in .kmz format are found in Data Repository File DR2. Gouges from these faults were all mineralogically characterized as part of a previous study that identified systematic patterns of clay mineral neomineralization in clay-rich fault gouges (Haines and van der Pluijm, 2012), and the samples analyzed in this study are all a subsample of samples from that study.

Sample Preparation and Characterization

Fault gouges are mixtures of fragmental wall-rock material derived from one or both sides of a fault zone and authigenic (neoformed) clay minerals growing in the gouge. Isolating the neoformed clay component of clay-rich gouges is therefore a challenging process, because the clay crystallites are very small (<<2.0 mm). Gouges can also contain fragmental phyllosilicates that are superficially similar to the authigenic phases but would contaminate the isotopic value without careful characterization. Our sampling approach is shown in Figure A.3. We use gravity settling in water to isolate the <2.0 mm (Stokes equivalent diameter) size fraction, followed by high-speed centrifugation to separate the clay-size fraction into three or four size fractions, coarse (2.0–0.2 mm), medium (0.02–0.05 mm), and fine (<0.05 mm). Each fraction is then characterized by XRD, using both oriented mounts (with and without ethylene glycol solvation) to identify principal clay phases and random powder mounts to accentuate the non-(00l) peaks characteristic of clay polytypes (which can be used to identify authigenic clay minerals in gouges). Additional site information and mineralogical description of these samples are found in Data Repository Files DR1 and DR2 and Haines and van der Pluijm (2012).

Sampling Clay-Rich Gouges

We analyzed only gouge clay samples that were well characterized in previous studies (Haines and van der Pluijm, 2010, 2012) for this study with >90% authigenic material based on XRD. X-ray diffraction patterns of all analyzed materials are given in Figure A.4. Isotopic measurements were made on splits from the same material described in Haines and van der Pluijm (2010, 2012). We note that three of the 14 samples contain near–detection-limit quantities of one or two other mineral phases: quartz in ASH-1, a 10-A phase (illite, muscovite, or biotite/phlogopite) in MOR-3 and A-BOMB-3, and calcite in MOR-3. Although all illitic material contained some interlayered smectite as discernable by XRD, for this study we only used illitic clays that were >80% illite in illite/smectite, and most were >90% illite in illite/smectite.

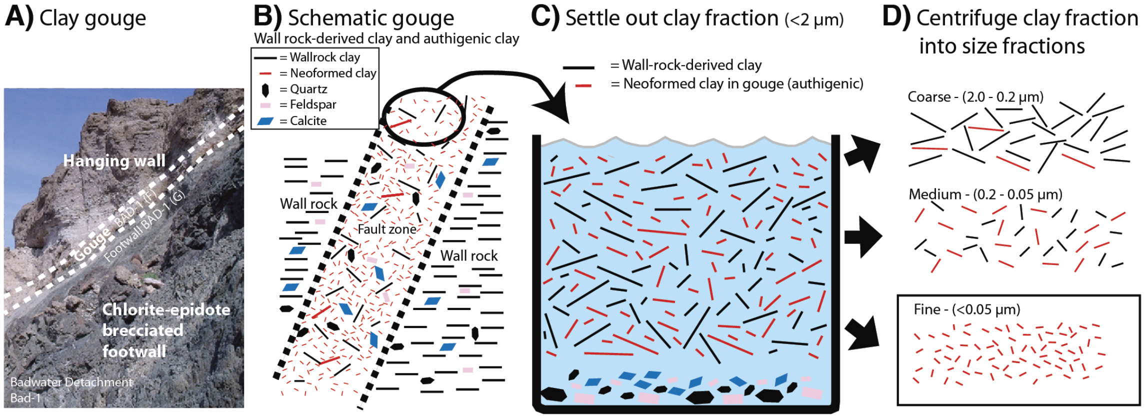

Figure A.3: Illustration of sample preparation process. (A) Field photograph of gouge sampling locality (Badwater-1). Sample Bad-1 (F) is illitic gouge from the pictured gouge layer. Sample Bad-1 (G) is the <0.05 mm fraction from disaggregated footwall. (B) Schematic representation of fault gouge in situ, highlighting neoformed clays in fault gouge and fragmental minerals, originating from the wall rock. (C) Separation of the clay fraction (<2 mm) by settling in water. (D) Centrifugation of the clay fraction into coarse (2.0–0.2 mm), medium (0.2–0.05 mm, abbreviated "M"), and fine (<0.05 mm, abbreviated "F") size fractions. All size fractions are then characterized by X-ray diffraction (XRD). Only medium- and fine-size fractions of clays that were nearly monomineralic to the level of XRD detection limits (<5%–10% other phase) were analyzed for O and H isotopes in this study.

Sampling Gouges Derived from Epidote/Chlorite Microbreccias

For this study, we only sampled chlorite-rich gouges where no other Mg-rich phyllosilicates (tri-octahedral clays such as saponite, chlorite/smectite, corrensite, talc/stevonsonite, or vermiculite-like phases, or other phyllosilicates such as sepiolite or palygorskite) were detectable by XRD. These samples also are free of other phases (e.g., epidote, feldspar, and calcite) to the level of XRD detection (Figure A.4C). In these gouges, chlorite in the fault gouge is structurally and compositionally indistinguishable from that found in chlorite-epidote alteration zones in the fault footwall as determined by

XRD (Haines and van der Pluijm, 2012). These purely cataclastic gouges have effectively disaggregated the footwall lithologies, allowing footwall-derived chlorite grains to be efficiently separated by settling in water and subsequent centrifugation, similar to the authigenic clays in clay-rich gouge (see above).

Analytical Methods

δ^{18}O Isotopic and δ^{2}H Measurements

Oxygen isotopic analysis of clay separates was completed in the University of Wisconsin Stable Isotope Laboratory by laser fluorination using BrF5 (Valley et al., 1995) and an airlock sample chamber that prevented pre-fluorination (Spicuzza et al., 1998). Hydrogen isotope measurements were made by continuous-flow mass spectrometry at the Stable Isotope Laboratory at Leibniz Universität Hannover, except for samples WH68-1 (F) and WH68-3 (MF) that were analyzed at the U.S. Geological Survey in Denver. All isotopic ratios are reported relative to Vienna standard mean ocean water (VSMOW), and methods are detailed in Data Repository File DR3.

Figure A.4: X-ray diffraction analyses of gouges sampled in this study. A) Illite-rich separate from gouges where illite is the neoformed mineral. Patterns are collected from random-mounted samples to highlight polytype-specific peaks. Characteristic (*hkl*) peaks of illite are shown at top. Grey boxes highlight broad humps centered at 24.9° and 29.1° 2q and are characteristic of the low-temperature $1M_d$ polytype of illite. Note that the intensities of $1M_d$ peaks are variable, depending on if the illite is cis-vacant or trans-vacant, and that samples lacking clear 24.9° and 29.1° peaks are still the $1M_d$. polytype. Q = quartz (present in the ASH-1 sample at near-detection limits). B) Smectites separated from gouges where smectite is the authigenic clay phase. Patterns are collected from oriented ethelyne glycol air-saturated samples to swell smectite interlayers. Characteristic (hkl) peaks of smectite are shown at top. K = kaolinite, present at near detection limits in WH68-3 (MF). C) Gouges where chlorite is the dominant clay mineral in the gouge. The chlorite is fragmental, derived from chlorite-epidote microbreccia footwall lithologies, and is not neoformed in the gouge. Patterns are collected from random-mounted patterns to highlight higher-order (hkl) reflections and polytype-specific peaks. Characteristic (hkl) peaks for chlorite are shown at top. I = 10 Å mica (illite, muscovite, or biotite) present in near-detection limit quantities in samples A-BOMB 3 (M) and MOR-3 (M). C = calcite, present in near-detection limit amounts in sample MOR-3 (M). Note that for all samples, (F) in sample name indicates size fraction <0.05 µm (Stokes equivalent). (M) = 0.2 – 0.05 µm size fraction. (MF) = <0.2 µm size fraction. Note that by contrast, (G) in a sample name refers to the green color from chlorite and does not connote a size fraction. BAD-1 (G) is a <0.2 µm size fraction.

A) Gouge illites

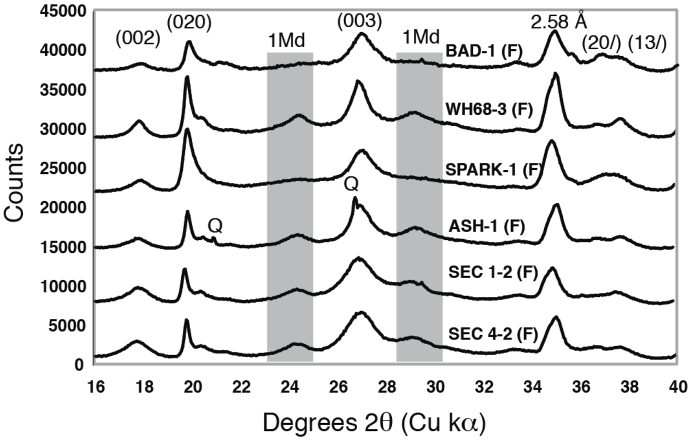

B) Gouge smectites

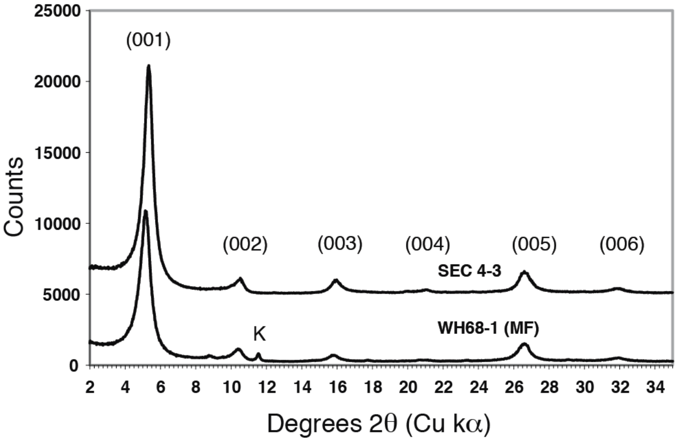

C) Gouge chlorites

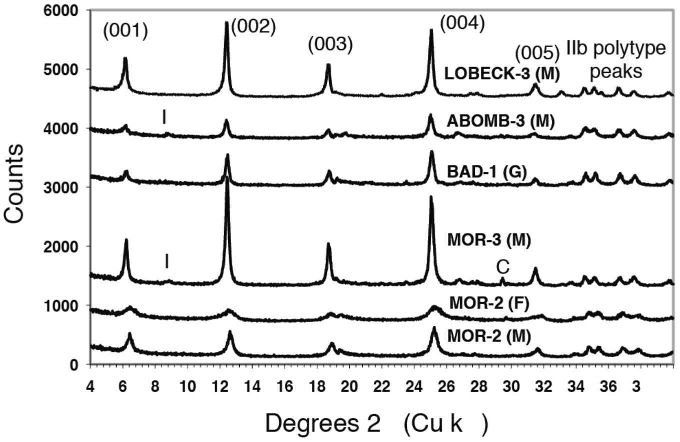

Illite Age Analysis (IAA)

^{40}Ar/^{39}Ar ages of samples were obtained by vacuum encapsulation (Dong et al., 1995) to address Ar loss during sample irradiation ("Ar recoil"). Samples were packaged into fused silica vials and sealed prior to irradiation (van der Pluijm et al., 2001). Thus, the ^{39}Ar expelled from the crystallites during irradiation is retained for analysis (see van der Pluijm and Hall, 2015, for a full description of the method). The sample vials were broken open, the initial gas was analyzed, and the vials were then step-heated under a defocused laser until sample fusion occurred. Note that the total gas age obtained from the vacuum-encapsulated sample is functionally equivalent to a conventional K-Ar age (Dong et al., 1995).

Results

Stable isotope values for LANF neoformed illite, smectite, and chlorite are shown in Table A.1 and Figures A.5A, A.5C, and A.5E. Individual illite δ^{18}O isotope values range from -2.0‰ SMOW (Ruby Mountains, SEC 4-2) to +11.5‰ (Badwater), and illite δ^{2}H values range from -142‰ (Ruby Mountains, SEC 1-2 and SEC 4-2) to -107‰ (ASH-1 [F]). Smectite δ^{18}O isotope values are +3.6‰ (Ruby Mountains, SEC 4-3) and +17.9‰ (Waterman Hills, WH68 [<2 mm]), while smectite δ^{2}H values are -147‰ (Ruby Mountains) and -95‰ (Waterman Hills WH-68-1 [F]). Both the Ruby Mountains main detachment illite (SEC 4-2) and illite from a hanging-wall normal fault (SEC 1-2) that formed coevally with the main detachment at 11–13 Ma (Haines and van der Pluijm, 2010) have isotopic values for δ^{18}O of -1.8‰ and -2.0‰, respectively, and δ^{2}H of -142‰ for both.

Values of $\delta^{18}O$ chlorite range from +0.58‰ to +8.1‰, and $\delta^{2}H$ values fall in a relatively narrow range from -97‰ to -113‰. The Mormon Point detachment samples—MOR-2 (M), MOR-2 (F), and MOR-3 (M)—all have relatively low $\delta^{18}O$ values ranging from +0.58‰ to +3.1‰ and $\delta^{2}H$ values from -99‰ to -108‰. The Chemehuevi detachment (LOBECK-3 [M]) and Badwater detachment (BAD-1 [G] [M]) samples have $\delta^{18}O$ values of +2.5‰ and +4.84‰, respectively, and $\delta^{2}H$ values of -106‰ and -113‰, respectively. The Buckskin-Rawhide detachment chlorite sample (A-BOMB-3) shows the highest δ-values, with $\delta^{18}O$ of +8.1‰ and $\delta^{2}H$ of -97‰.

Ages of neoformed clay in selected gouge samples are listed in Table A.2, and Ar degassing spectra for each grain-size fraction are included in Data Repository File DR4. We illustrate our results with a sample from the Badwater detachment (Figure A.6). Four size fractions show decreasing percentages of detrital illite with smaller grain sizes (Figure A.6A). Corresponding Ar ages for these samples are systematically younger with decreasing detrital illite, which we analyze in an IAA plot (van der Pluijm et al., 2001; Figure A.6B). Using linear York regression (Mahon, 1996) of percentage detrital illite versus e(l.t) - 1 (where l is decay constant and t is age) produces extrapolated authigenic and detrital intercept ages of 3.3 ± 0.4 Ma and 12.2 ± 1.9 Ma, respectively. Note that this particular regression analysis treats both parameters as independent, resulting in age errors that primarily reflect the 2%–3% error in mineralogic quantification, while individual Ar ages have much smaller errors, on the order of 0.2–0.5 Ma.

Table A.1: Sample locations and measured isotopic values of samples in this study

Detachment fault	Range	Gouge sample	Size fraction* (μm)	Sample mineralogy	δ^{18}O (‰ SMOW)	δ^{2}H (‰ SMOW)
Amargosa detachment	Black Mountains, CA	Ash-1 (F)	<0.05	Illite (1M$_d$)	10.6	-107
Badwater turtleback	Black Mountains, CA	Bad-1 (F)	<0.05	Illite (1M$_d$)	11.5	-140
Badwater turtleback	Black Mountains, CA	Bad-1 (G)	<0.2	Chlorite (IIb)	4.8	-113
Mormon point turtleback	Black Mountains, CA	MOR-2 (M)	0.2-0.05	Chlorite (IIb)	0.58	-99
Mormon point turtleback	Black Mountains, CA	MOR-2 (F)	<0.05	Chlorite (IIb)	3.1	-108
Mormon point turtleback	Black Mountains, CA	MOR-3 (M)	0.2-0.05	Chlorite (IIb)	0.75	-108
Buckskin-Rawhide detachment	Buckskin Mountains, AZ	A-Bomb 3 (M)	0.2-0.05	Chlorite (IIb)	8.1	-97
Waterman Hills detachment	Waterman Hills, CA	WH-68-1 (MF)	<2	Smectite	17.9	-95
Waterman Hills detachment	Waterman Hills, CA	WH-68-3 (F)	<0.05	Illite (1M$_d$)	10.9	-92
Chemehuevi detachment	Chemehuevi Mountains, CA	Lobeck-3 (M)	0.2-0.05	Chlorite (IIb)	2.5	-106
Panamint range front LANF	Panamint Mountains, CA	S-Park-1 (F)	<0.05	Illite (1M$_d$)	7	-138
Ruby Mountains core complex	Ruby Mountains, NV	SEC 1-2 (F)	<0.05	Illite (1M$_d$)	-1.8	-142
Ruby Mountains core complex	Ruby Mountains, NV	SEC 4-2 (F)	<0.05	Illite (1M$_d$)	-2	-142
Ruby Mountains core complex	Ruby Mountains, NV	SEC 4-3	<2	Smectite	3.6	-147

Note: All analyses are reported relative to standard meteoric ocean water (SMOW). LANF—low-angle normal fault; IIb—IIb polytype of chlorite as ascertained by XRD; 1Md—the 1Md polytype of illite as ascertained by XRD.

*Stokes equivalent diameter.

Table A.2: Illite age analysis results for samples from this study

Detachment fault	Gouge Sample	Size fraction*	%2M$_1$	±	TGA (Ma)	±	Age (Ma), 0% 2M$_1$	Age (Ma), 100% 2M$_1$	R^2
Amargosa detachment	Ash-1	2.0-0.2	80	2.5	139.7	0.2	3.2±3.9	170.4±108	0.998
		0.02-0.05	30	2.5	49.5	0.17			
		<0.05	3	2.5	11.5	0.18			
Badwater Turtleback	BW-2c	2.0-0.2	40	2.5	7.0	0.21	3.3±0.4	12.2±1.9	0.998
		0.02-0.05	30	2.5	5.6	0.2			
		>0.02	15	2.5	4.9	0.17			
		<0.05	2	2.5	3.3	0.55			
Mormon Point Turtleback	Mormon-1	<0.05	0	2	2.8	0.45	2.8±0.5	-	-
Mosaic Canyon fault	Mosaic-1	2.0-0.2	90	2	104.2	0.33	16.9±2.4	113.4±5.8	0.999
		0.02-0.05	60	2	75.1	0.17			
		<0.05	15	2	31.9	0.15			
Panamint Front Range fault	S-Park-1	<0.05	0	2	3.6	0.17	3.6±0.2	-	-

Note: TGA-total gas ^{40}Ar/^{39}Ar age. Raw Ar release spectra are available in GSA Data Repositor item 4 (see text footnote 1). 2M$_1$—the 2M$_1$ polytype of Illite, as ascertained by XRD.
*Stokes equivalent diameter.

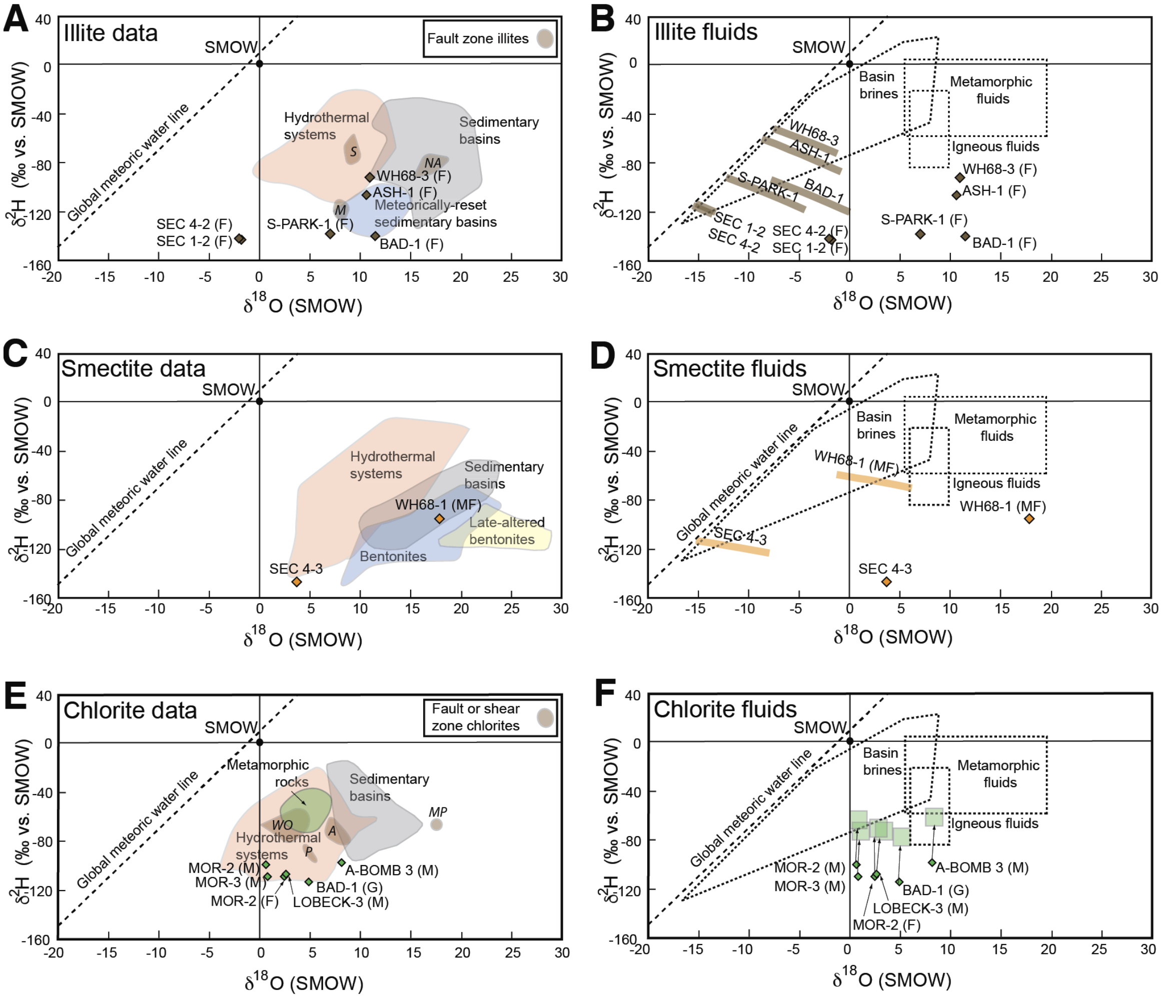

Figure A.5: δ^{18}O and δ^{2}H values of neoformed low-angle normal fault (LANF) gouge illite, smectite, and chlorite, together with calculated fluid compositions exchanging with each phase. (A) Fault-gouge illite isotopic values plotted together with isotopic data from illites from other geological environments for reference. Illite geological environment data are compiled from references in Data Repository Files DR5 and DR6. Uncertainties for all δ^{18}O and δ^{2}H measurements are within sample marker point size. Fault-gouge illite results: *S*—Savcili fault, Turkey (Isik et al., 2014); *NA*—North Anatolian fault zone, Turkey (Tonguç Uysal et al., 2006); *M*—Moab fault, Utah, USA (Solum, 2005). (B) Range of calculated fluid compositions of exchanging fluid for illites. Fluid compositions are calculated using fractionation equations of Sheppard and Gilg (1996) and Capuano (1992).Temperatures are bounded on the lower limit by 50 °C or the meteoric water line and on the upper end at 120 °C by the observed upper temperature limit for illite-rich illite-smectite in sedimentary basins. (C) Fault-gouge smectite isotopic values plotted together with isotopic data from smectites from other geological environments. Smectite geological environment data are compiled from references in Data Repository Files DR5 and DR6. (MF) indicates <0.2 mm size fraction. (D) Calculated fluid compositions of exchanging fluid for smectites. Fluid compositions are calculated using fractionation equations of Sheppard and Gilg (1996) and Capuano (1992).Temperatures are bounded on the lower limit by 50 °C or the meteoric water line and on the upper end at 120 °C. (E) Fault- gouge chlorite isotopic values plotted together with isotopic data from other geological environments for reference. Chlorite geological environment data are compiled from references in Data Repository Files DR5 and DR6. Fault or shear zone chlorite results: WO—Walter-Outalpa shear zone, Australia, Alice Springs orogen, Australia, and Argentera massif, France (Clark et al., 2006; Raimondo et al., 2011; Leclere et al., 2014); *A*—Alpine fault (Menzies et al., 2014); *P*—Picacho

metamorphic core complex (Kerrich and Rehrig, 1987); *MP*—Monte Perdido thrust, Spain (Lacroix et al., 2012). (F) Calculated fluid compositions of exchanging fluid for chlorites. Fluid compositions are calculated using fractionation equations of Cole and Ripley (1998) and Graham et al. (1987). Because significant uncertainties exist for the magnitude of chlorite-fluid exchange, likely fluid compositions are shown with boxes covering range of uncertainty. Please note: (F) in sample name indicates size fraction <0.05 mm (Stokes equivalent); (M) represents 0.2–0.05 mm size fraction. BAD-1 (G) is a <0.2 mm size fraction.

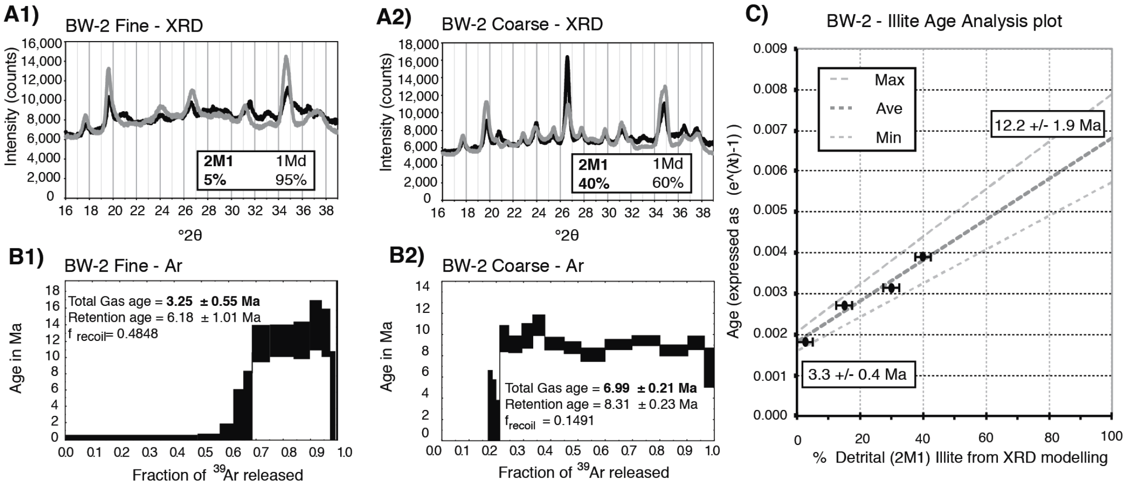

Figure A.6: Illite age analysis plot and supporting data illustrating clay dating approach. Samples from Badwater detachment are used to illustrate the method. (A1 and A2) Measured (black) and modeled (gray) XRD patterns from fine (<0.05 mm) and coarse (2.0–0.5mm) fractions respectively. The modeled (gray) XRD spectra quantify the ratio of authigenic (1Md) and detrital (2M1) illite in each grain size fraction. (B1 and B2) Ar release spectra from vacuum-encapsulated material analyzed in A1 and A2. All samples are vacuum encapsulated prior to irradiation to avoid complications associated with Ar recoil during irradiation; total gas ages incorporate both the Ar lost due to recoil (but trapped in the evacuated vial) and retained Ar (see van der Pluijm and Hall, 2014). (C) Illite age analysis plot comparing Ar encapsulation age (total gas age) and % detrital 2M1 polytype of illite in sample. Lower and upper intercepts of York regression on these data constrain the authigenic (3.3 ± 04 Ma) and detrital (12.2 ± 1.9 ma) ages of illite in this gouge sample.

Discussion

Our results from LANF gouge illites show that they are significantly depleted in both ^{18}O and ^{2}H compared to previously published results from illite formed in three fault gouges from strike-slip and normal fault environments (Figure A.5A; Solum, 2005; Tonguç Uysal et al., 2006; Isik et al., 2014). Because paired oxygen and hydrogen isotopic data from either illite or smectite taken from within fault zones are rare, we compiled published $\delta^{18}O$ and $\delta^{2}H$ data for neoformed illite, smectite, and chlorite from several different geological settings to place our results in a broader context: (1) sedimentary basins, (2) active and fossil hydrothermal systems, (3) sedimentary basins that experienced meteoric water flushing (illite only, e.g., Whitney and Northrup, 1987), (4) bentonites (smectite only), (5) bentonites where significant post-formation alteration caused ^{2}H and ^{18}O exchange to became decoupled (smectite only, e.g., Cadrin et al., 1996; Horton and Chamberlain, 2006), (6) metamorphic rocks (chlorite only), and (7) fault zones (illite and chlorite only). Compiled literature data are shown in Figures A.5A, A.5C, and A.5E. Compiled data are found in Data Repository File DR5, and supporting references in Data Repository File DR6.

Illite/Smectite Gouge Samples

Our gouge illite samples are isotopically depleted relative to illite that forms in sedimentary basins, and they are also depleted in ^{2}H with respect to illite that formed in hydrothermal systems. Some gouge illites (Waterman Hills, Amargosa, and Badwater) have oxygen and hydrogen isotopic compositions that are similar to illites from sedimentary basins interpreted to have been formed during basinal flushing with meteoric water ("meteorically reset") (Figure A.5A; Glasmann et al., 1989) or hydrothermal systems; but other gouge illites (Ruby Mountains and Panamint) have δ^{18}O and δ^{2}H values far lower than any reported from sedimentary basins. The Ruby Mountains illite samples preserve hydrogen and oxygen isotope values lower than any illite measurements yet reported (δ^{18}O = -1.8‰ and -2.0‰, δ^{2}H = -142‰ for both). Gouge smectite samples have isotopic compositions that are very similar to illite results, with the Waterman Hills sample (δ^{18}O = +17.9‰, δ^{2}H = -95‰) similar to smectites in sedimentary basins or smectites from bentonites (Figure A.5C) and the extremely isotopically depleted Ruby

Mountains smectite ($\delta^{18}O$ = +3.6‰, $\delta^{2}H$ = -147‰), which is the most depleted smectite isotopic measurement with respect to both oxygen and hydrogen yet reported.

Chlorite Microbreccia Samples

The chlorite isotopic data are similar to the most isotopically depleted chlorites found in hydrothermal systems (Figure A.5E), with the BAD-1 (G) (M) sample being the lowest $\delta^{2}H$ value yet reported ($\delta^{2}H$ = -147‰). Overall, our chlorite samples are very isotopically depleted, especially with respect to hydrogen (all $\delta^{2}H$ = -97‰ to -113‰), relative to those found in metamorphic terranes or in sedimentary basins (Figure A.5E and references in Data Repository File DR6). $\delta^{18}O$ values for the chlorite samples are more variable, ranging from = +0.6‰ to +11.5‰, likely reflecting variable amounts of fluid–wall-rock interaction.

Equivalent Fluid Compositions

Interpreting stable isotopic values of phyllosilicate minerals and using them to estimate the composition of the fluid with which they exchanged requires constraints on the temperature at which neoformed minerals grew and the associated fractionation between mineral and fluid. While clay gouges lack fluid inclusions that permit direct estimation of the temperature of formational fluids, the clay mineral assemblages found in these gouges place constraints on temperature at their time of formation. Previous studies of clay gouge mineralogy with reliable thermal constraints indicate that neoformed illite in fault gouges from a range of fault settings form at temperatures 80 °C to 180 °C, and perhaps as low as 50 °C (Haines and van der Pluijm, 2012). Because the neoformed illite is the low-temperature $1M_d$ polytype for all samples and XRD analysis indicates that all samples contain some interlayered smectite, the likely temperature of formation is no more than ~120 °C for both illite and smectite in LANF gouge. From measurements of $\delta^{18}O$ and $\delta^{2}H$ and estimates of a plausible clay-formation temperature range, the isotopic composition of the fluid that exchanged with the clay can be calculated. Using published $\delta^{18}O$ fractionation equations for illite and smectite (Sheppard and Gilg, 1996), we determine $\delta^{18}O$ fluid compositions in equilibrium with the clay phases measured (Figure A.5B and A.5D). Similarly, published water-mineral $\delta^{2}H$ fractionation equations for illite and smectite (Capuano, 1992) permit calculation of the fluid composition exchanging with the neoformed clays in LANF fault gouge. Based on this analysis, we find that the compositions of the fluids with which clays exchanged range from nearly pristine meteoric water to weakly isotopically enriched meteoric water. Calculated end-member water compositions are compatible with prior estimates of Middle Miocene (Ruby Mountains and Waterman Hills) and Pliocene (Armargosa, Panamint, and Badwater) Basin and Range meteoric waters (Poage and Chamberlain, 2002; Gébelin et al., 2012, 2015). Only the fluid exchanging with the Badwater gouge illite (Bad-1) shows significant deviation of oxygen enrichment from the field of isotopic values of fluids found in sedimentary basins with increasing depth (Figure A.5B), possibly reflecting oxygen exchange with silicate minerals in the fault zone prior to illite growth. Alternatively, the Death Valley area has been periodically evaporative since the Pliocene (Knott et al., 2005). Evaporative fluids are higher in $\delta^{18}O$ than the meteoric water line (Holser, 1979), which might also explain the observed O enrichment of the Badwater sample relative to other samples.

Previous Fault Zone Isotopic Results

The sole previous oxygen and hydrogen analyses of illite from the gouge of a normal fault, the Moab fault in Utah, USA ($\delta^{18}O$ = +7.9‰ and +8.6‰, $\delta^{2}H$ = -114‰ and -116‰, respectively; Solum, 2005) did not report an equivalent fluid composition, but our calculations from the reported mineral values are consistent with a weakly heavy isotope–enriched meteoric fluid ($\delta^{18}O$ = -4.0 to -6.5‰, $\delta^{2}H$ = -83 to -93‰). These limited results support our interpretation of a link between kinematic environment and fluid source, with normal fault systems being dominated by fluids of meteoric origin, while reverse fault systems are dominated by fluids of basinal or metamorphic origin (e.g., Kerrich, 1988; McCaig, 1997). By contrast, data from deeply rooted strike systems suggest fluid sources are more variable in these systems. Data from the crustal-scale North Anatolian fault zone indicate fluid infiltration at various times by fluids of metamorphic or magmatic origin (Tonguç Uysal et al., 2006) and meteoric origin (Boles et al., 2015). Data from the subparallel but shallower-rooted Savcili strike-slip fault zone (Isik et al., 2014) suggest a deep basinal origin for circulating fluids.

The temperature of chlorite formation in epidote-chlorite breccias is less constrained than that for illitic gouges. Estimates range from 300 to 350 °C (Kerrich, 1988) to 350–520 °C (Morrison and Anderson, 1998) and to 380–420 °C (Selverstone et al., 2012). To capture this uncertainty, we use a temperature range of 340–440 °C. The variation in oxygen isotope fractionation over the full range of proposed temperatures (300–520 °C) is <1.3‰, far smaller than the observed range for illite or smectite, and thus the uncertainty in temperature has little effect on interpretation of the chlorite data. Hydrogen isotope fractionation between chlorite and water is poorly constrained at -30‰

to -40‰ but is thought not to change significantly with temperature over the range at which these breccias formed (Graham et al., 1987). Unlike illitic and smectitic clay minerals, chlorite in both brittle fault zones (<300 °C) and mylonitic greenschist- and amphibolite-faces shear zones has been extensively studied with stable isotopic methods. Previous studies of chlorites in fault zones include LANF (Picacho Mountains metamorphic core complex [MCC], Kerrich and Rehrig, 1987), as well as upper greenschist- and/or lower amphibolite-facies shear zones in the French Pyrenees (Leclere et al., 2014) and central Australia (Clark et al., 2006; Raimondo et al., 2011) and a Tertiary thrust fault in the Pyrenees active at ~200 °C (Lacroix et al., 2012) (Figure A.5E). The results most germane to this study are chlorite samples from the Picacho Mountains MCC, which have $\delta^{18}O$ values of +4.7‰ to +5.5‰ and $\delta^{2}H$ values of -85‰ and -95‰. Our results are similar to these and suggest exchange with a fluid moderately enriched in $\delta^{18}O$ but depleted in $\delta^{2}H$. Overall, chlorites from LANF systems have similar $\delta^{18}O$ values to chlorites from amphibolite-facies shear zones inferred to have been infiltrated by meteoric fluids but have far lower $\delta^{2}H$ and $\delta^{18}O$ values than chlorites taken from brittle thrusts in compressional tectonic settings (Lacroix et al., 2012). Significantly, our samples all have $\delta^{2}H$ that is ~20‰ lighter than those observed in fault zones other than LANFs.

Meteoric Water Infiltration and Circulation

Isotopic exchange with fluids of meteoric origin has been increasingly documented associated with faults at mid-crustal depths (Morrison, 1994; Mulch et al., 2004; Gottardi et al., 2011; Gébelin et al., 2012; Mancktelow et al., 2015), but the mechanisms by which surface fluids reach these depths is not well understood (Roddy et al., 1988; Barentt et al., 1996; Losh et al., 2005; Hetzel et al., 2013). Our data from the upper brittle reaches of LANF systems show that meteoric water (with evidence of some wallrock–fluid interaction) is the predominant fluid in deformed upper crust of LANF systems down to several kilometers depths. Our results showing meteoric fluid infiltration in the brittle portion of LANFs, together with observations of meteoric fluids at greater depths (i.e., chlorite breccias and mylonites) and model predictions, suggest that the drawdown of meteoric water along brittle faults is the dominant fluid circulation system in and near fault zones in extended crust. Convective flow up to balance the fluid-flow system must therefore occur either away from the fault zones or elsewhere up some other reach of the same fault system. Recent studies in the Dixie Valley hydrothermal field have suggested that in some cases, fluids travel updip along discrete sections of basin-bounding normal faults and resurface in hydrothermal springs, the location of which are transient over thousand- to ten-thousand–year timescales, as supported by geochronologic studies of hot spring deposits (Blackwell et al., 2007). Additionally, geothermal modeling of this region suggests that thermal activity and fluid flow along faults may vary according to permeability structure of the fault, with some portions of the fault favoring the upward flow of fluids, whereas other along-strike portions of the fault may behave in a hydraulically opposite sense, allowing fluids to flow downdip (McKenna and Blackwell, 2004; Wanner et al., 2014). Variations in geothermal gradient in the basins also suggest that fluids may flow basinward away from faults through permeable sedimentary layers and layers with favorably oriented fracture networks (Blackwell et al., 2007). Our study of neoformed clays offers novel documentation that supports previous assertions that hanging-wall rocks of evolving LANFs experienced extensive infiltration of surface fluid at least along some, if not all, portions of transient fault and fracture systems to depths of as much as 10 km over time periods of millions of years. This upper-crustal plumbing system provides a pathway for meteoric fluids to mid-crustal depths and formation of mineral deposits by mixing of meteoric fluids with deeper-sourced, metal-enriched fluids (Spencer and Welty, 1986; Roddy et al., 1988).

Evaluation of Post-Faulting Isotopic Exchange

A concern with stable isotopic analysis of clay minerals is the possibility that the measured isotopic values record late isotopic exchange at near-surface conditions and that the measured values do not reflect the conditions at the time of clay formation at temperatures of 60–180 °C for illite and smectite, or the greenschist-facies conditions at which the cataclastically reworked chlorites originally formed. To address this concern, we: (1) compared our calculated paleofluid compositions to present-day meteoricwater compositions near the faults we sampled, and (2) dated the sample material we used for the stable isotopic measurements by $^{40}Ar/^{39}Ar$ methods.

The stable isotopic composition of modern precipitation across the western United States has been investigated extensively and was recently reviewed by Lechler and Niemi (2011). The $\delta^{18}O$ values of precipitation at sites closest to our sample sites range from -15.6‰ to -8.3‰ with a general trend toward more negative values toward the north and northwest (Friedman et al., 1992, 2002; Lechler and Niemi, 2012; Table A.3 and Figure A.7). The $\delta^{2}H$ of precipitation at sites closest to our sample sites range from -115‰ to –57‰, decreasing toward the north and northwest, generally correlating with $\delta^{18}O$ and following the global meteoric water line across the Great Basin. The $\delta^{2}H$ values of precipitation do deviate slightly from the meteoric water line during the summer months when evaporative fractionation effects are strongest (Friedman et al., 2002). Our calculated paleofluid compositions record a similar trend in that more isotopically depleted paleofluid compositions are also found at faults where present-day precipitation is strongly isotopically depleted. However, two lines of evidence suggest our calculated paleofluid compositions reflect ancient fluids and not late alteration or mixing with present-day fluids. (1) Calculated fluid compositions are sometimes isotopically heavier with respect to both oxygen and hydrogen (e.g., BAD-1) or lighter (ASH-1, S-PARK-1, WH68-1, and WH68-3) than present-day precipitation (Figure A.7), suggesting that there is not a direct relationship between calculated paleofluid composition and observed present-day precipitation. Where calculated paleofluid compositions are similar to present-day precipitation compositions (SEC 1-2 and SEC 4-2), the required 100–120 °C temperatures are inconsistent with vadose-zone interaction with current precipitation and instead consistent with higher-temperature interaction with an even more isotopically depleted fluid. (2) Dating of the authigenic clays also excludes the concern that mineral isotopic signals are indicative of late, near-surface low-temperature exchange after faulting. All of the $^{40}Ar/^{39}Ar$ ages for the samples listed in Table A.2 are geologically consistent with clay growth while the sampled faults were active. The Ruby Mountains ages (reported in Haines and van der Pluijm, 2010, on splits from the samples used in this study) document the last major period of slip and fluid activity on the detachment at ca. 12 Ma, consistent with previous thermochronometer work (Colgan et al., 2010). The Panamint detachment gouge age of 3.6 ± 0.2 Ma is consistent with an inferred Pliocene time of slip (Andrew and Walker, 2009), while the mid-Miocene age for the Tucki Mountain gouge (16.9 ± 2.4 Ma) is also geologically plausible (Hodges et al., 1990).

Table A.3: Average isotopic values of present-day precipitation nearest our sampling sites						
Detachment fault	Range	Gouge sample	Nearest present-day precipitation measurement	Average δ^{18}O (‰ SMOW)	Average δ^{2}H (‰ SMOW)	Source
Amargosa detachment	Black Mountains, CA	Ash-1	Death Valley, CA	-9.5	-75	Friedman et al. (1992, 2002)
Badwater turtleback	Black Mountains, CA	Bad-1	Death Valley, CA	-9.5	-75	Friedman et al. (1992, 2002)
Badwater turtleback	Black Mountains, CA	Bad-1 (G)	Death Valley, CA	-9.5	-75	Friedman et al. (1992, 2002)
Mormon point turtleback	Black Mountains, CA	Mormon-2	Death Valley, CA	-9.5	-75	Friedman et al. (1992, 2002)
Mormon point turtleback	Black Mountains, CA	Mormon-3	Death Valley, CA	-9.5	-75	Friedman et al. (1992, 2002)
Buckskin-Rawhide detachment	Buckskin Mountains, AZ	A-Bomb 3 (M)	Parker Dam, AZ	-8.3	-61	Friedman et al. (1992)
Waterman Hills detachment	Waterman Hills, CA	WH-68	Dagett, CA	-10.9	-72	Friedman et al. (1992)
Waterman Hills detachment	Waterman Hills, CA	WH-68	Dagett, CA	-10.9	-72	Friedman et al. (1992)
Chemehuevi detachment	Chemehuevi Mountains, CA	Lobeck-3 (M)	Needles, CA	-8.3	-57	Friedman et al. (1992)
Panamint range front LANF	Panamint Mountains, CA	S-Park-1	Panamint Range, CA	-13.4	-108	Lechler and Neimi (2012)
Ruby Mountains core complex	Ruby Mountains, NV	SEC 1-2	Elko, NV	-15.6	-115	Friedman et al. (2002)
Ruby Mountains core complex	Ruby Mountains, NV	SEC 4-2	Elko, NV	-15.6	-115	Friedman et al. (2002)
Ruby Mountains core complex	Ruby Mountains, NV	SEC 3-3	Elko, NV	-15.6	-115	Friedman et al. (2002)

Note: Data compiled from Friedman et al. (1992, 2002) and Lechler and Neimi (2102). (M) in sample name represents 02-0.05 µm size fraction; Bad-1 (G) is a <0.2 µm size fraction.
LANF – low-angle normal fault.

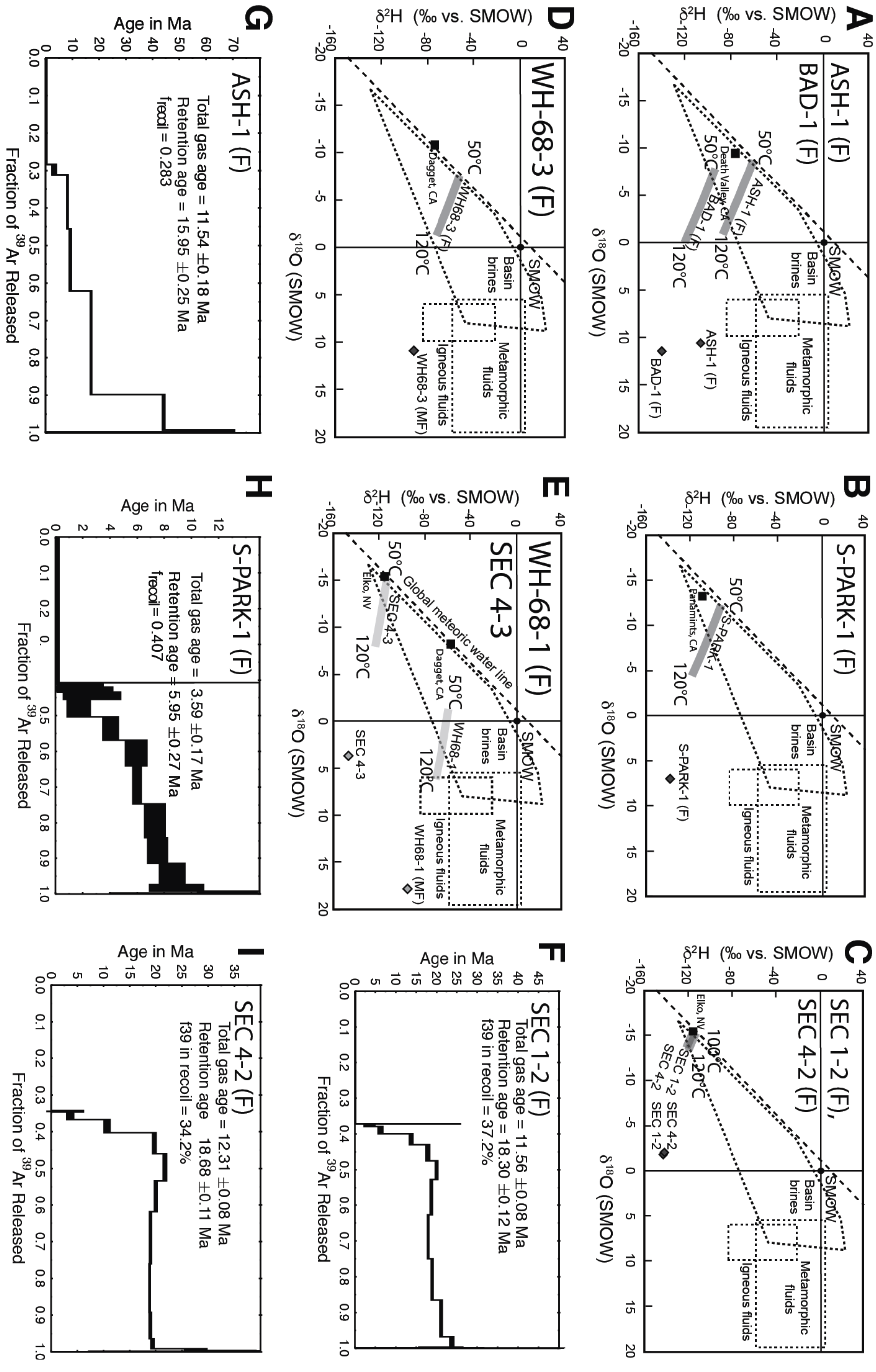

Figure A.7: Plots showing independence of measured isotopic values in gouges and present-day meteoric water signatures. (A)–(D) δ^{18}/δ^{2}H plots for individual illitic samples. Temperatures are lower and upper temperatures used for exchanging fluid-composition calculations based on clay mineralogy. (E) δ^{18}/δ^{2}H plot for smectitic samples. (F)–(I) ^{40}Ar/^{39}Ar spectra from splits of material used for isotopic analysis. Diamonds—measured isotopic values; brown lines—calculated equivalent fluid composition; blue squares—average isotopic signature of present-day precipitation (data from Friedman et al., 1992, 2002; Lechler and Neimi, 2012; compiled in Table A.3). Please note: (F) in sample name indicates size fraction <0.05 μm (Stokes equivalent); (M) represents 0.2–0.05 μm size fraction.

Likewise, Late Pliocene ages for gouge formation in Armargosa (3.2 ± 3.9 Ma), Mormon (2.8 ± 0.5 ma), and Badwater (3.3 ± 0.4 Ma) detachments of the Black Mountains record the last major pulse of motion on these LANFs (e.g., Knott et al., 2005; Norton, 2011). The dated fault rocks do not show evidence of significant postfaulting alteration, which demonstrates that meteoric fluid signatures preserved in neoformed clays are representative of ancient fluid circulation and not modern surface alteration.

Conclusions

Our study of neoformed clays and chlorites in exhumed shallow-crust to mid-crustal LANF systems shows that both LANF clay gouges and mid-crustal chlorite "microbreccias" exchanged isotopically with pristine to weakly evolved meteoric water. The presence of meteoric waters in LANF detachments at multiple crustal levels indicates these systems were hydrologically open for large parts of their history. Instead of recording lateral infiltration along major detachments or burial of pre-metamorphic fluids (e.g., Clark et al., 2006; Raimondo et al., 2011, 2013), we conclude that fluid circulation of crustal-scale LANF systems occurs by drawdown of meteoric waters through evolving fault and fracture networks that form and propagate in response to regional extension in the hanging wall, possibly aided by topography to drive fluid flow (Figure A.8).

Our dynamic scenario explains the observations of near-pristine meteoric water at upper- to mid-crustal levels in LANFs, with transient fault networks providing efficient pathways for significant quantities of meteoric water to reach into the crust. Our interpretation of a surface-to-depth plumbing system in LANFs and comparison with depth-to-surface fluids in thrust systems suggests that fluid dynamics of the upper crust is closely linked to the kinematic environment.

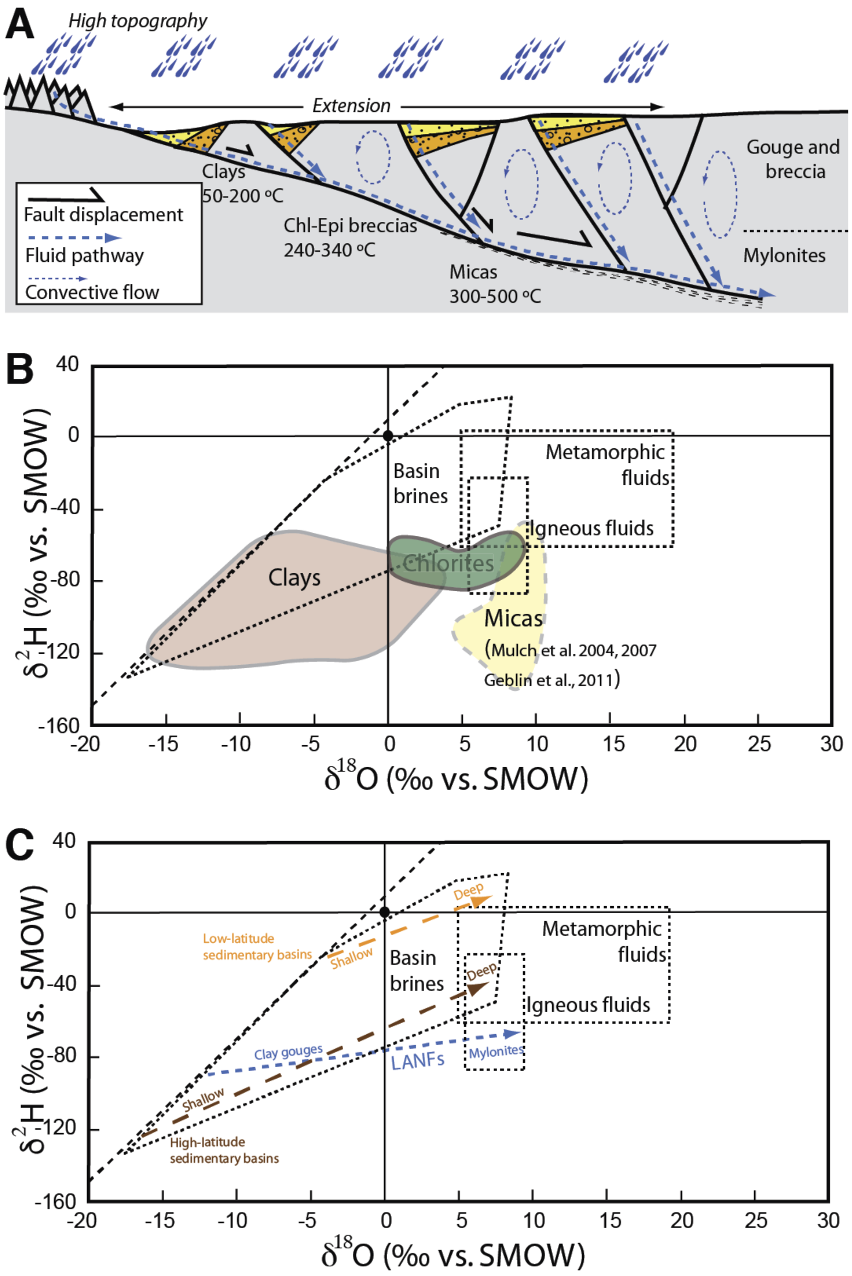

Figure A.8: (A) Schematic illustration showing low-angle normal fault (LANF) meteoric fluid circulation system. Transient networks of faults and fractures in actively extending upper crust create efficient pathways for downward infiltration of meteoric fluids driven by topographic head and transient opening and closing of narrow spaces in evolving fracture networks that reach basal detachment faults. (B) Calculated fluid compositions in equilibrium with clay minerals (illite and smectite), chlorite, and muscovite from LANF systems. Clay and chlorite fields are plotted from equivalent fluid compositions calculated from our data; mica field is equilibrium fluid compositions for data from muscovite data of Mulch et al. (2004, 2007) and Gébelin et al. (2011) and calculated using the fractionation equations of O'Neil and Taylor (1969) and Suzuoki and Epstein (1976). (C) Fluid circulation in LANFs as deduced from our data and previously published data. Fluid isotopic composition with increasing depth as observed in present-day sedimentary basins is shown for reference (Clayton et al., 1966). Note the increasing deviation from the meteoric water line of the calculated fluid composition with increasing depth, indicating progressive rock buffering of an initially meteoric fluid migrating down the detachment system.

Acknowledgements

This chapter was published in *Lithosphere* with coauthorship of Samuel Haines and Ben van der Pluijm. Research was supported by National Science Foundation (NSF) grant EAR-1118704 (to van der Pluijm) and the Turner and Wilson funds of the University of Michigan (to Haines and Lynch). We thank Monamie Bhadra and Kaajal Bhadra for assistance with fieldwork. We thank R.E. Anderson at the U.S. Geological Survey in Denver for pilot measurements that supported this study at the initial stages and Mike Spicuzza at University of Wisconsin–Madison for laser fluorination. We are grateful to staff at Death Valley National Park for permission to sample within the park area. We thank Christian Teyssier and an anonymous reviewer for reviews, as well as Gary Axen, Vincent Famin, and another anonymous reviewer for comments on an earlier version. Mulch acknowledges support through Deutsche Forschungsgemeinschaft (DFG) grant Mu2845/2-1. The Stable Isotope laboratory at UW-Madison was supported by grants NSF-EAR-1144454 and DOE-BES DE-FG02-93ER14389.

Appendix B. ^{40}Ar/^{39}Ar-dating correction procedure

Ar-dated samples from March, 2015 to October, 2017 were affected by a gas-line leak in the Argon Geochronology Lab. The malfunction, affecting total gas age analysis for encapsulated samples only, was reflected in unusually large recoil percentages (Figure B.1). The leaking section of the vacuum line caused mis-measurement of the first gas fraction relative to those later in the step-heating procedure. In effect, the first fraction was not allowed to leak out of a defective valve for the first fraction, which made that fraction abnormally large compared to the remaining gas fraction, producing the anomalously large gas recoil fraction (Figure B.1).

In order to determine a correction procedure, we selected 22 key samples from 4 previous studies (Chapter III; Chapter V; Appendix 1; Boles, 2017) for re-analysis. To remove the effect of the leak for non-repeat TGAs, we determined the signal decay rate to correct to a time after gas inlet that accounts for the loss in the remaining gas fraction. By comparing the first, affected set of analyses with 9 re-analyzed samples (bold, table B.1), we obtained a decay time of 117 seconds. We arrived at 117 seconds through iterative least squares optimization to match the re-measured ^{40}Ar/^{39}Ar-ages and recalculated ages that resulted from removing different amounts of time from the initial measurement run (e.g., 60s, 90s, 120s, 180s, etc.). Sample re-runs were not used for decay time determination if their Retention Ages were >5% different from one another, indicating that the sample material that was re-dated was not identical to the original dated fractions. The resulting systematic relationship between re-calculated ages and re-measured ages shows excellent correlation (Figure B.2, Table B.1). The average error on the corrected total gas ages (C-TGA) for the Appalachian samples is ±2% TGA.).

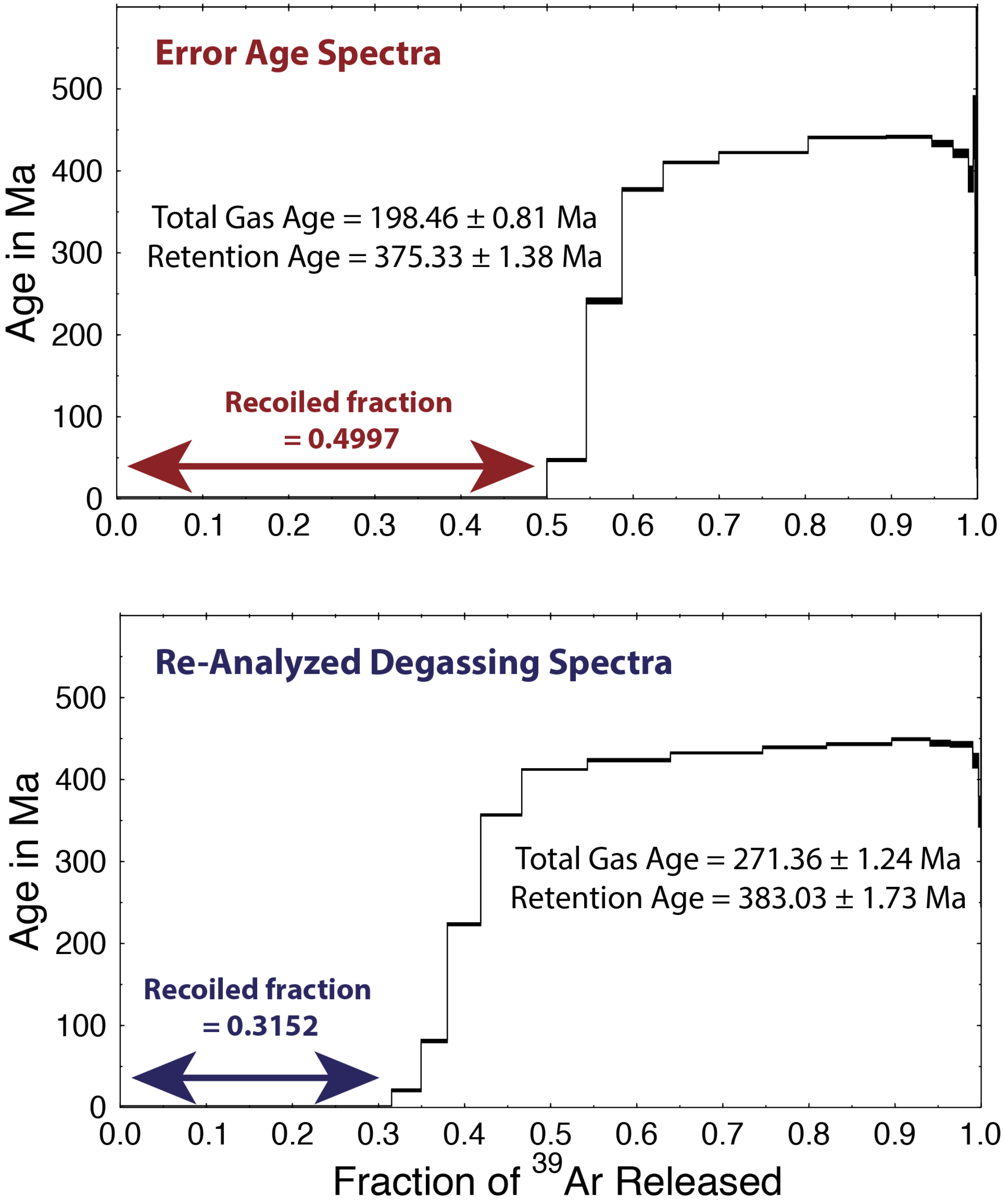

Figure B.1: Two Ar-degassing spectra for sample MD-MS-1 Fine (<0.05 µm). The top degassing spectrum (error age) has a recoil fraction that makes up nearly half of the measured gas fraction. This fraction (age=0) caused the Total Gas age to be anomalously young. The bottom spectrum (re-analyzed sample) has a smaller recoiled gas fraction, which gives an older (true) Ar-age.

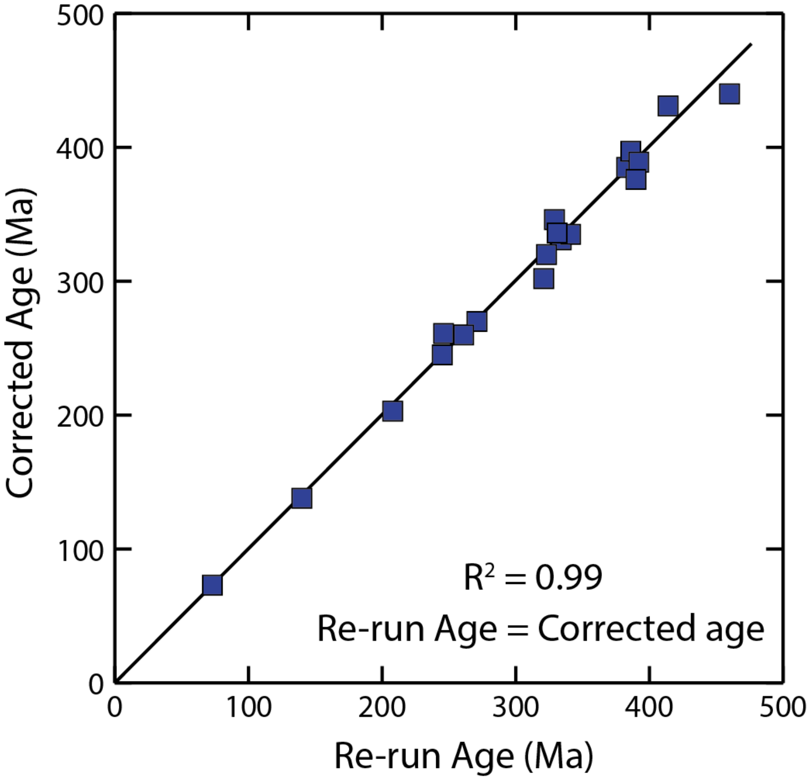

Figure B.2: Re-dating plots showing the minimal misfit between re-run ages and 117s corrected ages. This correction is subsequently used for previously dated samples that were affected by the gas leak.

Table B.1: ^{40}Ar/39Ar-dating data used for decay time correction correlation

Sample Name	Error Age (Ma)	Re-run Age (Ma)	Corrected age (Ma)	Error (%)
SNPA07 Fine[1]	259	334	331	-1%
SNPA07 Coarse[1]	320	460	440	-4%
MDMS1 Fine[1]	198	271	270	0%
MDMS1 Medium[1]	412	383	385	1%
WVMcK7a Fine[1]	189	261	260	0%
WVMcK7a Med. Fine[1]	270	329	346	5%
PABF22 Fine[1]	180	245	245	0%
PABF22 Medium[1]	275	386	397	3%
PHRH33 Fine[1]	189	246	261	6%
PARH33 Med. Coarse[1]	342	392	389	-1%
NY04 Very Fine[2]	238	321	302	-6%
NY04 Fine[2]	166	341	335	-2%
NY07 Coarse[2]	114	414	431	4%
NY07 Very Fine[2]	268	323	320	-1%
NY15 Medium[2]	399	390	376	-4%
NY15 Very Fine[2]	293	331	336	2%
W15-163A Medium[3]	114	140	138	-1%
W15-275 Med. Fine[3]	166	208	203	-2%
BW-2c Fine[4*]	3.3	5.6	3.6	-36%
JA03 Fine[5]	64	73	73	-1%

[1] Chapter V

[2] Boles, 2017

[3] Chapter III

[4] Appendix A

[5] Unpublished sample

*Not used in correlation due to Retention Age difference of 41%

Samples listed in **bold** represent the first batch of re-analyzed samples and were used in determining the 117 second decay time correction procedure.

Appendix C. A preliminary comparison of orogenic fluids in the Southern and Central Appalachians

Abstract

We compare the orogenic fluid history of the thrust-fault dominated Southern Appalachian foreland deformation belt with the fold-dominated Central Appalachian foreland belt. Our preliminary stable isotopic study of dated clay gouge and foreland shale from the Southern Appalachian Tennessee salient includes measurements of oxygen and hydrogen isotopic composition (δD and $\delta^{18}O$) on four clay samples: three thrust fault gouges and one foreland shale. Calculations of fluid composition based on temperatures derived from illite crystallinity and constrained by conodont alteration indices suggests that fluid sources are likely not the same for each setting. The foreland shale authigenic illite grew from fluids that resemble evaporatively enriched formation/basin fluids (δD = -1.6 ± 7.6‰, $\delta^{18}O$ = 2.2 ± 0.4‰), possibly originating from Ordovician seawater or nearshore (low-elevation) precipitation. Authigenic illite in the Copper Creek thrust appears to have grown from Appalachian metamorphic fluids (δD = -26.6 ± 9.2‰, $\delta^{18}O$ □ 6.6 ± 0.4‰). More negative δD values in both the St. Clair (-67 ± 4.2‰) and Great Smoky (-43 ± 13.9‰) thrusts fluids indicate that they contained a component of surface-sourced/meteoric-derived fluid. The $\delta^{18}O$ composition of the St. Clair Thrust fluid (11.2 ± 0.4‰) implies extensive fluid-rock isotopic buffering of the surface-sourced fluid component. These results indicate that deeply-rooted thrust structures tap voluminous

deep fluid sources, but also variably involve surface fluids during contractional deformation.

Introduction

The Southern Appalachian Mountains differ structurally from the central and northern portions of the orogenic belt in that they are characterized by the long-distance transport of late Paleozoic thrust sheets rather than large-scale folding and strike-slip faulting (Hatcher et al., 1989). Faults in the Central Appalachian region are small and typically not exposed (blind thrusts), whereas deeply-rooted large thrust faults crop out in the southern Appalachians. The latter have displacements on the order of 10s to 100s of kilometers and typically displace massive carbonate or higher grade metamorphic units onto of a comparatively thin package of Paleozoic siliciclastic sediments (Hatcher et al., 2007). This history is a result of the terminal collision of Laurentia and Gondwana in the Late Paleozoic, which formed the supercontinent Pangea.

Fault gouges and foreland shale samples collected from the Tennessee-Virginia section of the Southern Appalachians (Figure C.1) were characterized and dated by Hnat (2009) and Hnat and van der Pluijm (2014), who consistently found Permian ages for fault activity. Using a subset of their samples (Table C.1), this study mirrors the techniques described in Chapter V of this dissertation to expand the fluid record of the Appalachians to the south. For four samples—three thrust faults (Great Smoky, Copper Creek, and St. Clair) and one foreland shale (Ordovician outcrop from the Nashville Dome, Tennessee)—we measured the stable isotopic composition of the illitic clay minerals and calculate the isotopic composition of the fluid from which those clays grew.

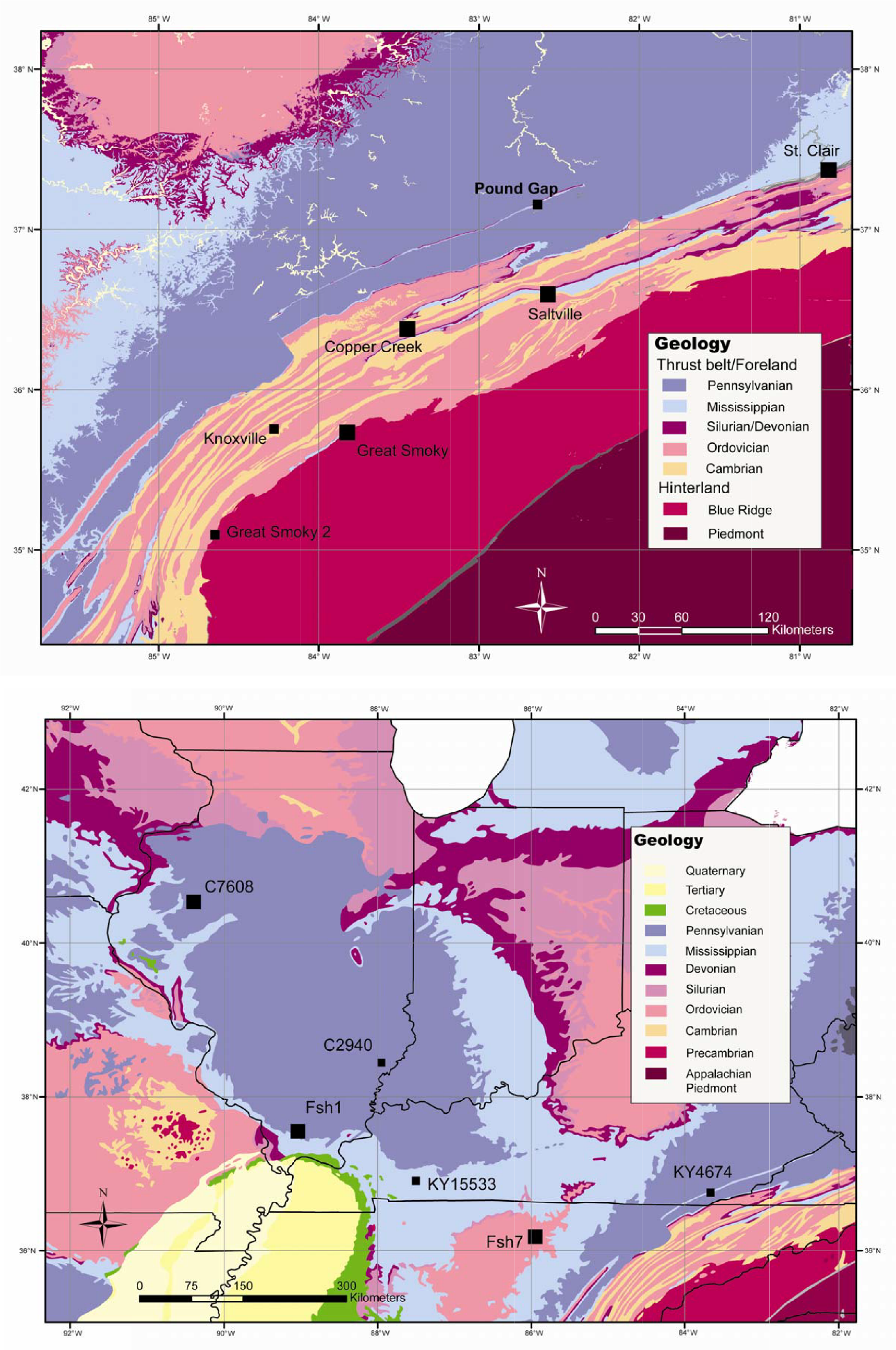

Figure C.1: Geologic map from Hnat (2009) showing the location of the samples used in this study. Thrust samples are shown in the top map, the single foreland shale location is shown in the bottom map (labeled Fsh7).

These four samples were chosen due to their favorable clay composition that contain large (>70%) portions of authigenic $1M_d$ illite (Hnat, 2009).

Table C.1: Summary of the results of $^{40}Ar/^{39}Ar$-dating of the samples used in this study with data compiled from Hnat (2009)

Sample	Fraction	$\%1M_d$	$^{40}Ar/^{39}Ar$-age (MA)	Authigenic Age (MA)
Copper Creek	Coarse	82 ± 2.0	344.9 ± 0.5*	279.5 ± 11.3*
	Medium	88 ± 2.0	326.8 ± 0.8*	
	Fine	96 ± 2.0	293.7 ± 0.6*	
St. Clair	Medium	73 ± 3.0	300.4 ± 0.9**	276.6 ± 6.8**
	Medium Fine	81 ± 2.0	294.0 ± 0.8**	
	Fine	84 ± 2.0	290.7 ± 0.4**	
Great Smoky	Coarse	78 ± 2.0	448.0 ± 1.5**	277.2 ± 29.6**
	Medium	84 ± 2.0	385.5 ± 1.2**	
	Fine	91 ± 2.0	357.3 ± 1.0**	
Ordovician Shale	Coarse	71 ± 2.0	438.6 ± 1.2*	300.1 ± 28.6*
	Medium	81 ± 2.0	408.0 ± 0.9*	
	Fine	95 ± 2.0	321.5 ± 0.6*	

* Total Gas Age
**Retention Age

The Great Smoky Thrust is one of the major thrust structures in the Southern Appalachian belt, separating the metamorphic Blue Ridge province from the sedimentary foreland fold-thrust belt (Hatcher et al., 2007) (Figure C.1). Estimates for total displacement on portions of this thrust based on seismic-reflection data are greater than 300 km (Hatcher et al., 2007). The magnitude of displacement is interpreted to be much smaller on the Copper Creek and St. Clair Thrusts, on the order of 10s of kilometers (Hatcher et al., 2007; Whisonant, and Schultz, 1986). Both of these thrusts place Cambro-Ordovician carbonate units onto younger fine-grained siliciclastics. At the sample locations, the Copper Creek and St. Clair thrust gouge zones were ~0.5 and ~0.25 meters wide, respectively, whereas at the Great Smoky thrust outcrop, the gouge deformation zone was gradational into the footwall shale.

Stable Isotopic Measurement

Previously processed sample separates (see Hnat, 2009, for specifics on sample preparation) were collected from the sample repository at the University of Michigan and analyzed in the Stable Isotope Laboratory at the Institute for Earth Surface Dynamics (IDYST) at University of Lausanne (UNIL). Methods of isotopic measurement completed at UNIL for this study are described in Chapters IV and V of this dissertation. Hydrogen isotopic composition (δD) measurements (and duplicates) were completed on all fractions except the finest fraction of the Great Smoky Thrust, which was not available for analysis. Oxygen isotopic composition ($\delta^{18}O$) was measured for the three fine fractions available, including one duplicate measurement on the Copper Creek sample to determine variability between sample fine fraction aliquots. Error on δD measurements is ±2‰ based on duplicates and reproducibility of internal standard measurements. Error on $\delta^{18}O$ measurements is in ±0.2 ‰ based on reproducibility of internal standards, however, a 0.38‰ difference between duplicate measurement of the Copper Creek sample indicate that there is some variability within sample size fraction aliquots. We adopt an error of ±0.4‰ for the interpretation of our $\delta^{18}O$ results. Results are listed in Table C.2.

Regression Analysis

We use a York-style statistics to determine the δD composition of the authigenic illite end member (Figure C.2) (York, 1968). For the Copper Creek Thrust, St Clair Thrust, and Ordovician shale localities, we use three size fractions (6 data points including duplicates) to complete the regressions. For the Great Smoky locality, only two size fractions are analyzed (4 data points) due to the small amount of fine material available. As a result, the error on the calculated intercept value for the Great Smoky Thrust is larger than that of the other three samples.

Table C.2: Results of stable isotopic measurements

Sample	Fraction	δD (±2‰)	δD (duplicate)	δ^{18}O (±0.2‰)	δ^{18}O (duplicate)
Copper Creek	Coarse	-70.0	-70.7	-	-
	Medium	-71.2	-72.8	-	-
	Fine	-38.8	-38.7	20.22	19.85
St. Clair	Medium	-72.9	-74.2	-	-
	Medium Fine	-70.7	-71.0	-	-
	Fine	-71.7	-72.2	18.14	-
Great Smoky	Coarse	-72.7	-71.4	-	-
	Medium	-64.6	-64.4	-	-
	Fine*	-	-	-	-
Ordovician Shale	Coarse	-67.8	-66.8	-	-
	Medium	-67.8	-66.6	-	-
	Fine	-15.4	-14.3	15.65	-

*No sample material available

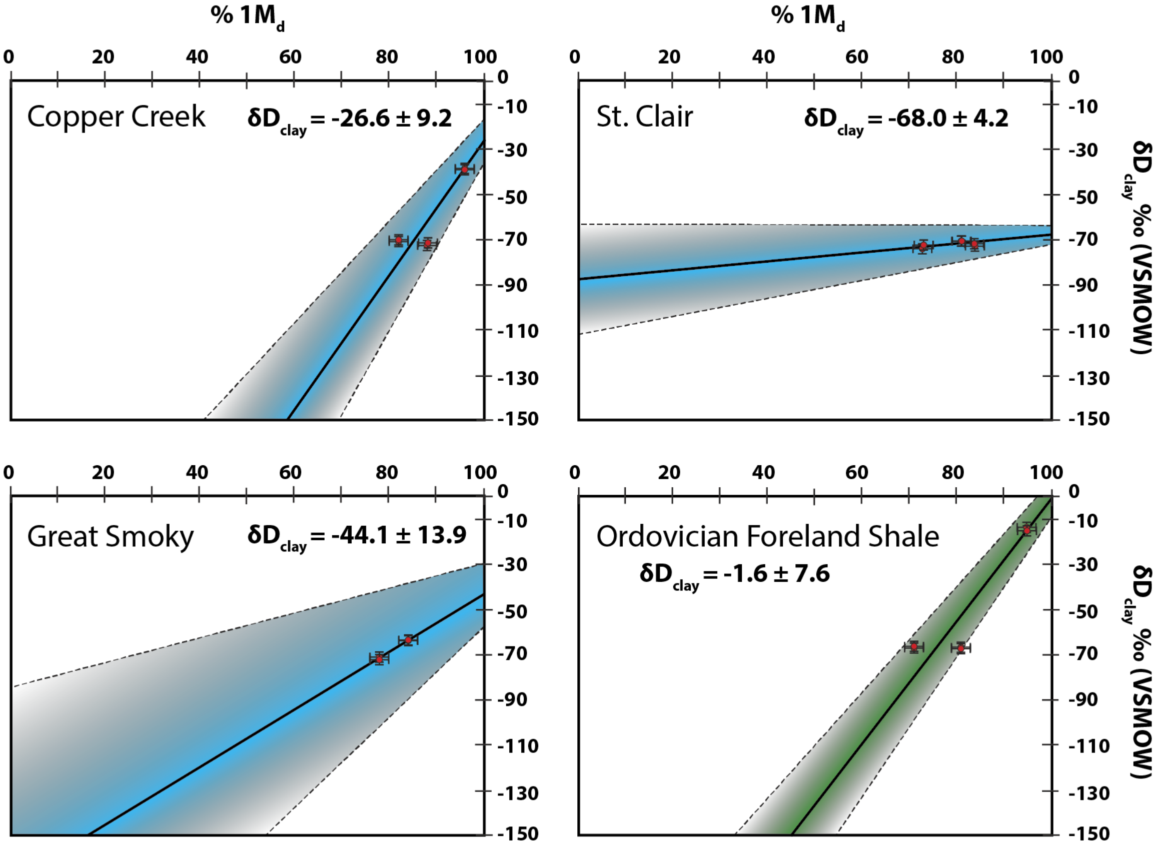

Figure C.2: Results of the regression analyses are shown for the three thrust samples (blue) and one foreland shale sample (green). The bold black best-fit line is shown in the colored error envelope, which is outlined with a dotted line. Data points and error bars are shown in red. δD$_{clay}$ (the 100% authigenic intercept) is listed in bold for each sample.

Two of the samples, Copper Creek and the Foreland Shale, have fine fractions that are noticeably less negative than their larger fractions, which is illustrated in the steep slope of their regression lines. These two fine fractions are comprised of at least 95% $1M_d$ illite. In the case of the St. Clair and Great Smoky thrust, no equally pure fraction was available.

Discussion

Fractionation

Using the illite crystallinity measurements reported in Hnat (2009) and Hnat and van der Pluijm (2014), and illite crystallinity correlations with diagenetic grade (Verdel et al., 2012) we estimate the temperature of illite formation for the samples to be between 100 and 200°C (Table C.3). From this, we use the fractionation equations of Capuano et al. (1992) and Sheppard and Gilg (1996) to calculate the δD and $\delta^{18}O$ composition of the fluid using an average temperature of formation of 150°C (Table C.3). Results reveal significant differences between fluid compositions for each sample, in fact, none of the samples' isotopic compositions overlap within error in either oxygen or hydrogen space.

Table C.3: Fractionation calculation temperatures and fluid isotopic composition

Sample	δD_{clay} (‰)	$\delta^{18}O_{clay}$ (±0.4‰)	IC_{fine} (°2θ)*	δD_{fliud} (‰)	$\delta^{18}O_{fluid}$ (±0.4‰)
Copper Creek	-26 ± 9.2	20.22, 19.85	1.149	-14 ± 9.2	10.6, 10.3
St. Clair	-68 ± 4.2	18.14	0.582	-56 ± 4.2	8.5
Great Smoky	-44 ± 13.9	-	0.567	-32 ± 13.9	-
Foreland Shale	-2 ± 7.6	15.65	1.181	11 ± 7.6	6.5

*From Hnat(2009)

Fluid Source(s)

Results of the fractionation calculations indicate that multiple source fluids and mixing processes were at play in the Southern Appalachians (Figure C.3). First, the foreland shale fluid has a positive δD signature, on the high end of the metamorphic fluid field. It is more positive than standard mean ocean water (SMOW = 0‰). Its $\delta^{18}O$ composition is also slightly positive. The likely process to create fluids of this composition is the evaporative enrichment of formation/basin fluids that originated as ocean water (Sheppard, 1986). This suggests that this foreland shale did not interact with metamorphic fluids released from the orogenic core of the belt, and rather that the authigenic illite grew from locally-sourced fluids that were contained within the pore spaces of Ordovician shale, likely originating as ocean water.

The thrust fault fluids show varied fluid sources. The St. Clair thrust fluids fall within the composition of Appalachian Metamorphic fluids, indicating that this fault may have been a conduit for upward migrating deeply-sourced fluids. The Copper Creek and Great Smoky thrusts, on the other hand, have δD values that are negative enough to require the input of meteoric fluids in some proportion to explain their isotopic composition. The $\delta^{18}O$ composition of the Copper Creek fluid is very heavy/positive relative to meteoric water, suggesting that isotopic exchange between the fluid and the host rock has occurred. No oxygen isotopic data was available for the Great Smoky Thrust.

Comparison of Orogenic Fluids in the Southern and Central Appalachians

There are several differences between the Southern Appalachian fault and Central Appalachian fold samples that emerge from this exploratory study. First, in the Southern Appalachians, we observe one sample location (Copper Creek) that seems to have interacted only with metamorphic fluids, and not with significant volumes of meteoric or surface-sourced fluids. In the Central Appalachians, all samples pointed to a fluid source that incorporated at least 25% meteoric fluid input (Chapter V). Of the two Southern Appalachian samples that did indicate surface-fluid involvement, both δD values overlapped with the calculated isotopic composition of the Central Appalachian orogenic fluids (Figure C.3).

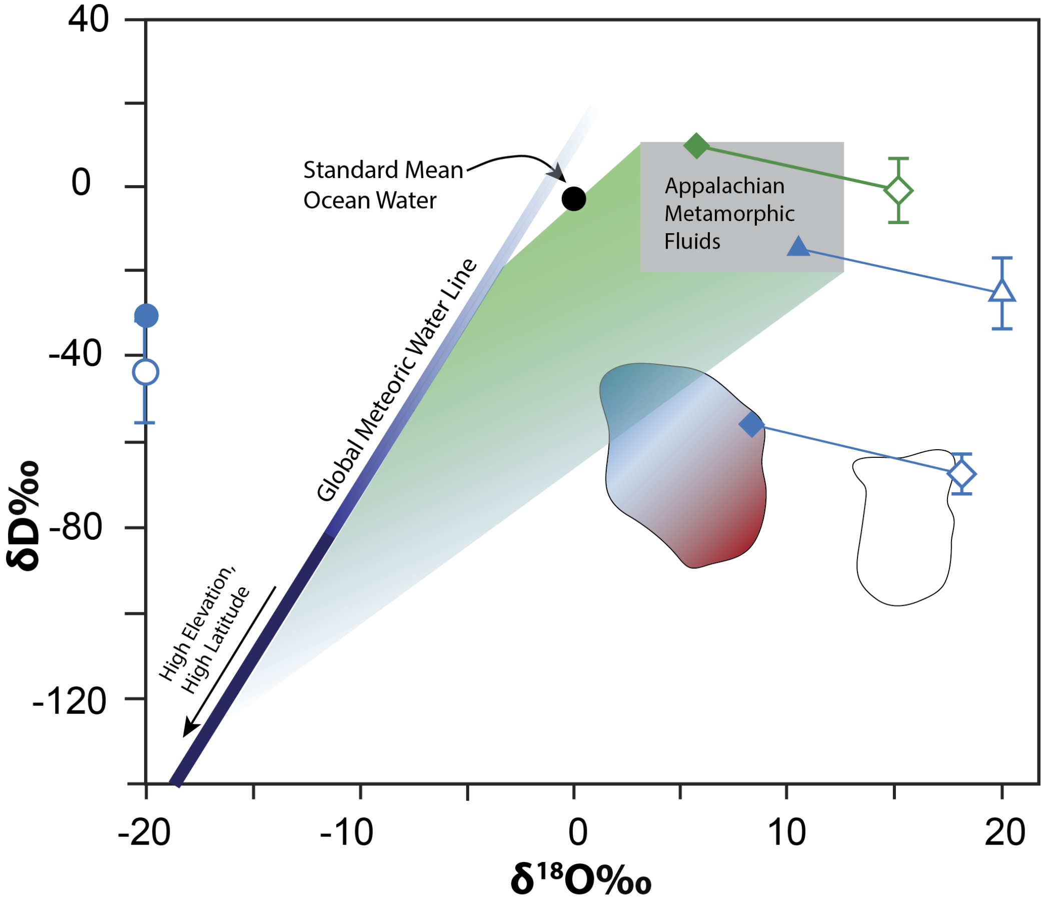

Figure C.3: Stable isotope plot adapted from Chapter V showing the fields of fluid composition and the isotopic composition of authigenic clay minerals. The indigo line represents the range of isotopic compositions of meteoric water (Sheppard, 1986). The gray box shows the composition of Appalachian metamorphic fluids. The green band shows the region of mixing of the two end-member fluids. The white outlined region shows the composition of Central Appalachian authigenic clay minerals with their associated fluids shown in the red to blue shaded field (Chapter V). Data from this study are shown by the open and solid symbols. Blue symbols show the isotopic composition of authigenic fault illite and associated fault fluids (open and solid, respectively): Triangle = Copper Creek, Diamond = St. Clair, Circle = Great Smoky (no δ^{18}O data). The green diamonds show the isotopic composition of the foreland shale sample (open) and its fluid (solid). Errors on δ^{18}O values are smaller than the symbols.

Preliminary exploration of $\delta^{18}O$ composition of Central Appalachian orogenic fluids indicates that isotopic buffering with the host rock was an important process in modifying the composition of the orogenic fluid. In the case of the St. Clair sample, $\delta^{18}O$ composition is also very positive, similarly to the isotopically buffered fluids of the Central Appalachians, falling along the right edge of the Central Appalachian fluid field in Figure C.3. This supports the interpretation of our studies elsewhere (Chapter V,) that isotopic buffering masks the original oxygen isotopic composition and thus source(s) of the fluid.

Conclusions

Stable isotopic analysis of fault gouge and shale illite shows that fluid sources within fold-thrust belts and foreland basins are varied. δD values ≤-40‰ for the Great Smoky and St. Clair thrusts indicate significant involvement of surface-sourced fluid, whereas δD values >0‰ for the Copper Creek thrust and foreland shale sample indicate metamorphic or evaporatively-enriched basinal fluid sources, respectively. Heavy oxygen isotopic compositions indicate that water-rock buffering played a role in modifying the isotopic composition of the orogenic fluids, which is overcome by the analysis of their H composition. This limited, four-sample study provides an intriguing glimpse into the variability of orogenic fluids of the Appalachians, and likely success of for future work to characterize the spatial and structural heterogeneity of fluids in this major fold-thrust belt.

Acknowledgements

This study was possible thanks to a Pre-doctoral fellowship to Lynch from the Rackham Graduate School at the University of Michigan. Funding for isotopic measurements was provided by the NSF grant. Additional thanks are extended to Benita Putlitz for her guidance in the IDSYT Stable Isotope Lab at UNIL.

Appendix D. Isotope geochemistry of Mercury in fault rocks and host rocks of the San Andreas Fault system, Parkfield, CA

Abstract

Documenting the mercury cycle on a global scale has typically focused on its movement through the hydrosphere and the biosphere. In the solid earth record, mercury fluxes are generally studied only in the uppermost parts of the geosphere, particularly in volcanic emissions and soil cycling. Study of mercury in the rock record has focused on mercury ore deposits, which are generally near-surface deposits. Expanding the understanding of mercury fluxes in the deeper crust is a topic that has only recently begun. This study examines the concentration of mercury into fault and host rock of California's San Andreas Fault zone. We observe an increase in mercury concentration in fault rocks relative to host rocks, with fine-grained samples hosting more mercury than coarse grained samples. This enrichment is also sometimes associated with an increase in total organic carbon (TOC). With mercury enrichment, we note a change in isotopic composition that records a negative mass dependent fractionation (MDF), but no significant mass independent fractionation (MIF). We propose three possible explanations for the MDF of mercury in fault rocks: (1) input of mercury to the fault zone from an external source, (2) fractionation associated with mercury adsorption to clay minerals or binding to organic matter, or (3) fractionation associated with the liberation of mercury from its original source/vaporization of dissolved mercury in the fault zone. We are unable to identify a mercury source that matches the mixing profile of the fault

rocks, so we interpret the isotopic signature to reflect fractionation processes during mercury migration, limiting utility in using mercury isotopes as tracers for the source fluids in fault zones.

Introduction

Mercury Isotopes in the Geologic Record

The study of isotopic variation of mercury in both geologic and biologic samples is benefiting from increasing precision and application of multi-collector inductively coupled plasma mass spectrometry (MC-ICP-MS). The characteristic isotopic signatures and fluxes of mercury have been examined in regards to natural reservoirs at or near Earth's surface, including the oceanic, atmospheric, geologic, and biologic realms. A large variation in isotopic ratios has been observed across the major terrestrial mercury reservoirs, reflecting the multitude of pathways of isotopic fractionation that are influenced by both geologic and biologic processes.

The cycling of mercury has been the subject of many recent studies (Blum et al., 2014). Mercury is introduced into the atmosphere by both anthropogenic and volcanic processes (Yin et al., 2010). Volcanic and geothermal activity also contribute mercury to the oceanic reservoir, which also undergoes exchange with that atmosphere primarily through redox reactions. Gaseous, elemental Hg(0) in the atmosphere is oxidized to Hg(II), which causes it to become reactive and to be deposited onto soils and plants, and into bodies of water (Engstrom, 2007). Various processes occur following the introduction of Hg into water, such as oxidation and reduction, volatilization and evaporation, which are all associated with mass dependent fractionation (MDF), and when mediated by photochemical reactions, they may exhibit mass independent fractionation (MIF). Methylation and demethylation of mercury also occurs, involving both photochemical and biochemical pathways, and is associated with MIF as well as MDF (Blum et al., 2014). Characteristic fractionation pathways for many of these processes are shown in Figure D.1 (Blum and Bergquist, 2007). Sediments and soils act as sinks in the mercury cycle, incorporating various MDF and MIF signatures that are characteristic of their pathways of formation.

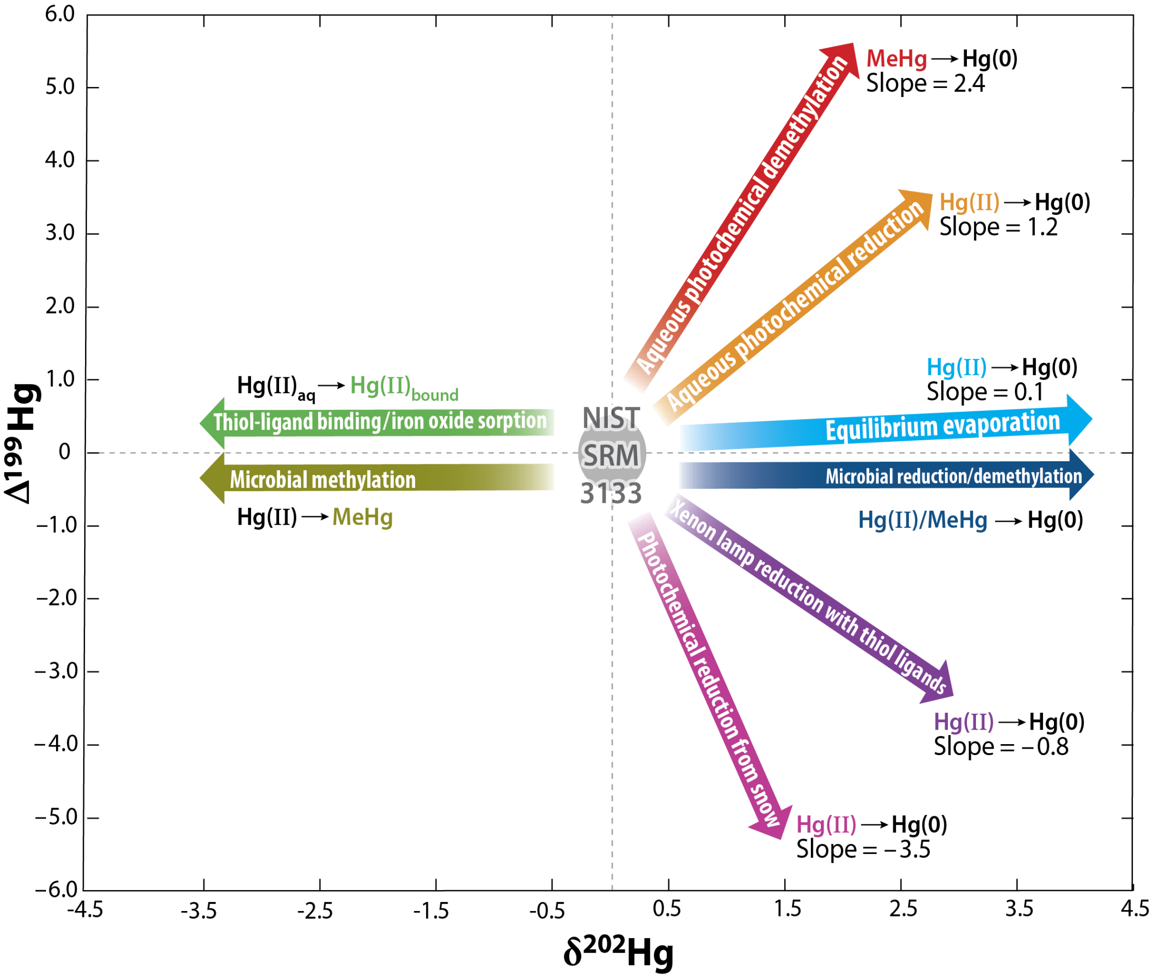

Figure D.1: Diagram from Blum et al. (2014) showing the fractionation signatures for various processes. δ^{202}Hg is used to notate mass dependent fractionation signatures. Δ^{199}Hg notates mass independent fractionation processes. δ- and Δ- values are reported in permil (‰) relative to the NIST SRM 3133 Hg standard (Blum and Bergquist, 2007).

Anthropogenic emissions of mercury generally fall into two categories: industrial and fossil fuel related. Industrial emissions of mercury are often associated with mercury ores and elemental mercury, which is characterized by a lack of MIF and a MDF signature that favors heavy isotopes (Liu et al., 2011). Fossil fuel related emissions may show small amounts of MIF (Biswas et al., 2008; Lefticariu et al., 2011), however they are associated with very negative MDF signatures (Liu et al., 2011). Most rocks show no evidence of significant MIF, though their MDF is variable and likely depends on the equilibrium kinetic fractionation during geologic processes such as reduction, evaporation, and volatilization (Bergquist and Blum, 2007). Shales and organic rich sedimentary rocks, such as coal, occasionally have a negative MIF, indicating their association with biologic processes prior to deposition (Blum et al., 2014). A significant negative MDF,and small positive MIF signature has been observed in near-surface hydrothermal spring deposits and has been interpreted to arise due to boiling and liberation of light mercury from the source rocks (Smith et al., 2005). These natural variations in mercury isotopic signatures have proven a valuable tool in several previous studies that have been successful in using isotopic ratios to fingerprint the source of mercury deposited in sediments and to trace the pathways of mercury migration in sedimentary systems (e.g. Foucher et al., 2008; Feng et al., 2010; Liu et al., 2011).

Though these studies have focused on sediments, which are primarily considered a sink in the global mercury cycle, mercury has also been shown to migrate out of sediments under certain conditions. Yangfen et al. (1989) observed that mercury concentrations in groundwater experienced significant spikes associated with faulting and hydrofracturing, indicating that changes in temperature and pressure conditions at depth in the crust trigger the mobilization of mercury. The potential isotopic fractionation associated with this mobilization has not been well-characterized. Zhang et al. (2014) completed a study of fault rocks from the Wenchuan Earthquake Fault Scientific Drilling Project Hole-1 and noted significant increase in mercury content within the fault core. They proposed that mercury mobilized by fault activity was transported in fluids and subsequently adsorbed onto clay particles in fault gouge. The current study explores this idea through the lens of the San Andreas Fault system by characterizing the mercury content and isotopic composition of both wall rock and fault rock collected from the SAFOD core and nearby outcrops.

The San Andreas Fault

The San Andreas Fault is a well-studied continental transform fault zone that accommodates lateral slip between the North American and Pacific tectonic plates. Due to the seismic hazards and large population centers proximal to the fault, the structure of the fault zone as well as the composition of the surrounding rock units is well studied (e.g, Bradbury et al., 2007; Solum et al., 2006; 2007; Schleicher et al., 2007). In 2004, the San Andreas Fault Observatory at Depth (SAFOD) project completed a ~3 km long borehole that extended to approximately 2.2 vertical kilometers depth in the crust, intersecting the San Andreas Fault in the area of Parkfield, California. One of the primary research objectives for the SAFOD project was to study the source and composition of fluids present in the fault zone and to understand their impact on seismicity (Hickman et al., 2004).

The source of San Andreas Fault fluids has been a topic of discussion for several decades. Previous research identified the presence of mantle helium in the fault zone and argued a deep mantle source for fluids in the fault system (Kennedy et al., 1997; Pili et al., 2011). Based on these and other observations, several authors have proposed possible mechanisms for deep-fluid generation and up-fault fluid flow (Becken et al., 2008; Kirby et al., 2014). Others have proposed that meteoric fluids and/or formation fluids play a major contributing role in deformation (Kharaka et al., 1999; Luetkemeyer et al., 2016).

Samples of fault rock from the SAFOD core were chosen for studying mercury cycling for two primary reasons. First, the samples were collected from depth and are, therefore, unlikely to have been altered by dry deposition of mercury from the atmosphere, thus preserving their primary signature. Second, the coastal source rocks and mercury ores in the region were previously studied and characterized with respect to their MDF and MIF signatures (Smith et al., 2008, Blum et al., 2014). With this study, we hoped to use the mercury isotopic signatures as a fluid tracer that determines where fault fluids originated.

Methods

Sample Selection

SAFOD core samples and Franciscan outcrop samples were compiled from a variety of sources for geochemical studies. The location of the SAFOD drill site and the Franciscan sample locations are shown in Figure D.2. The SAFOD core drills through Salinian block gravels and granitoid units, crossing the Buzzard Canyon Fault and boring through arkosic sandstones and conglomerates before it reaches the main fault zone, which is contained primarily in the Great Valley Sequence units (Zoback et al., 2011) (Figure D.3). Fault zone samples from the SAFOD core samples consist of variously deformed host rock from gently sheared claystone, to intensely sheared and foliated gouge and cataclasite (Solum et al., 2007; Bradbury et al., 2007; Zoback et al., 2011; Holdsworth et al., 2011) (Figure D.3). The SAFOD core does not intersect the Cretaceous Franciscan complex; samples of Franciscan units were instead obtained from the collection of Smith et al. (2008). They include a variety of lithologies: serpentinites, greywacke, blueschist, and mudstone. The locations of the outcrops sampled are shown in Figure D.3; individual samples are described in Table D.1.

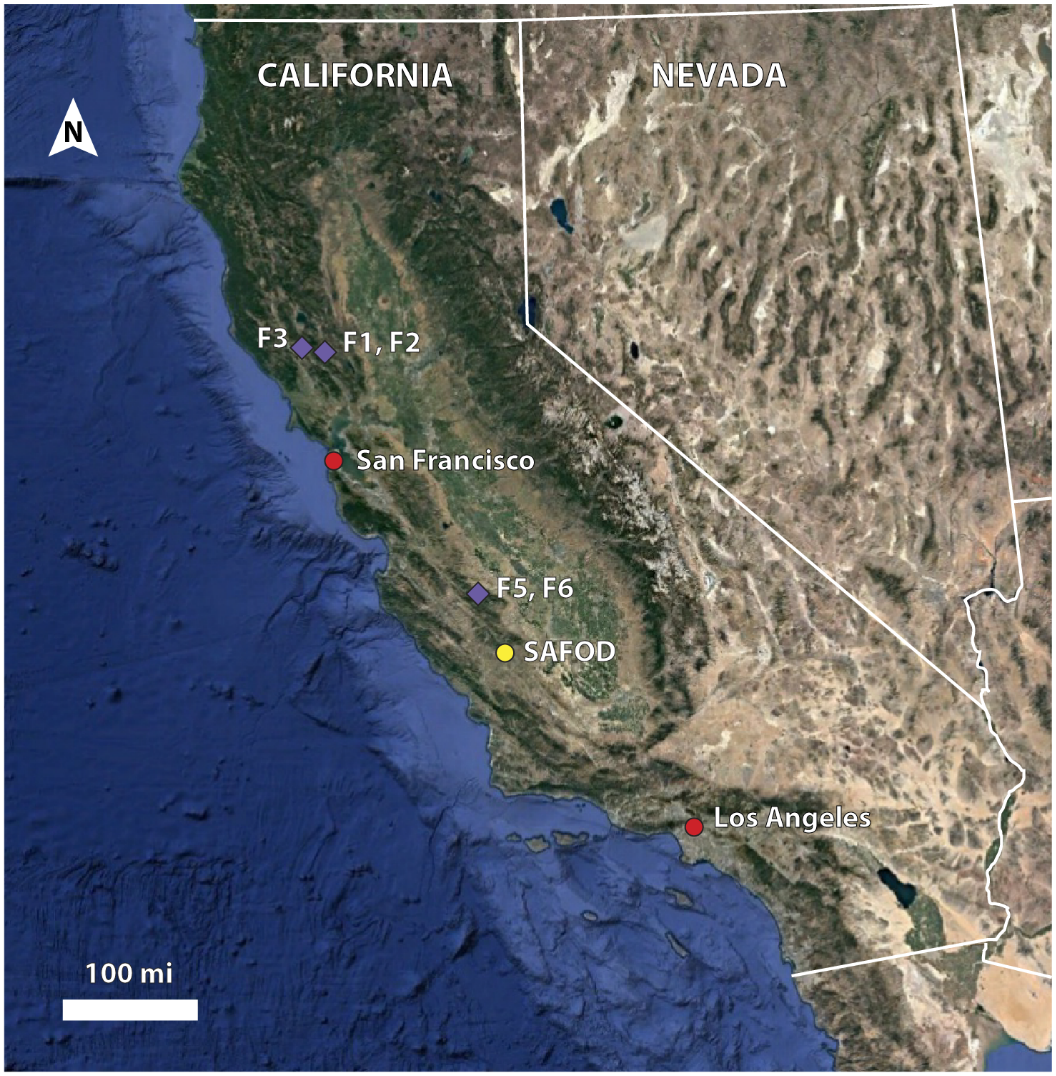

Figure D.2: Map of California showing the location of the SAFOD drilling site and the locations of the Franciscan sample outcrops (purple diamonds).

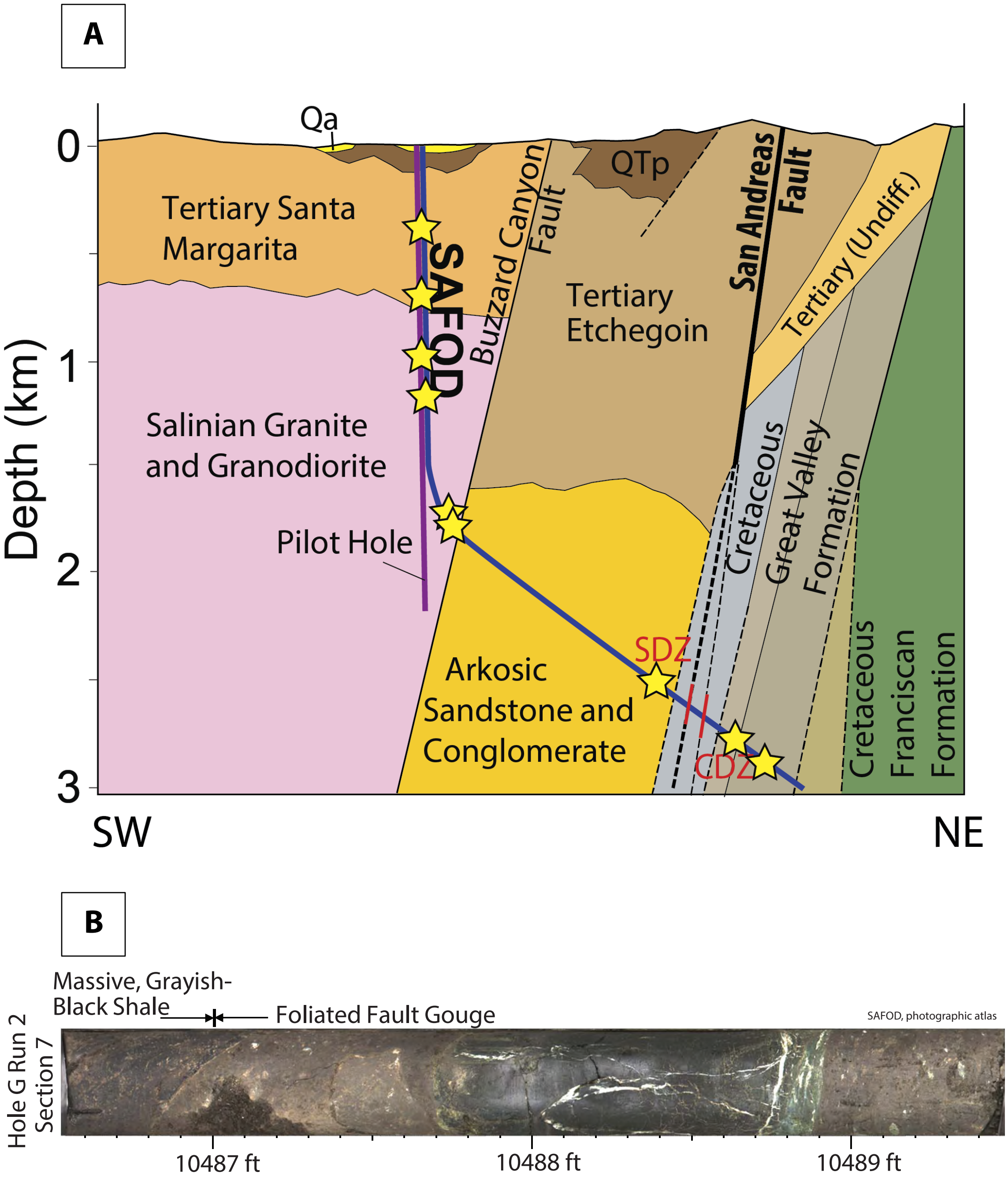

Figure D.3: (A) schematic cross section of the SAFOD core after Zoback et al., 2011. Stars show the approximate location of the non-fault zone samples used in this study. The fault zone is marked in red where it intersects the SAFOD core in the Southern Deforming Zone (SDZ) and Central Deforming Zone (CDZ). (B) Image of the core taken from the SAFOD fault zone (SAFOD Photographic Atlas, 2011). Sample GR2S8 was obtained from foliated fault gouge in this section of the core.

Table D.1: Sample names and descriptions

Sample	Rock Type	Formation	Source
4600 MD	Granite	Salinian Granodiorite	SAFOD core
4900 MD	Granodiorite	Salinian Granodiorite	SAFOD core
3400 MD	Granite	Salinian Granodiorite	SAFOD core
E1S1	Arkose	Santa Margarita Formation	SAFOD core
E1S4	Shale	Santa Margarita Formation	SAFOD core
F-1	Serpentinite	Franciscan Formation	Smith et al., 2008
F-2	Greywacke	Franciscan Formation	Smith et al., 2008
F-3	Blueschist	Franciscan Formation	Smith et al., 2008
F-5	Cherty mudstone	Franciscan Formation	Smith et al., 2008
F-6	Greywacke	Franciscan Formation	Smith et al., 2008
B4R4	Granodiorite	Salinian Granodiorite	SAFOD core
G5S3	Siltstone	Great Valley Sequence	SAFOD core
2002A*	Siltstone	Great Valley Sequence	SAFOD core
GR1S1-Coarse	Cataclasite	Fault Zone	SAFOD core
GR6S5-Coarse	Sheared claystone	Fault Zone	SAFOD core
GR6S5-Medium	Sheared claystone	Fault Zone	SAFOD core
GR6S5-Fine	Sheared claystone	Fault Zone	SAFOD core
GR2S8-Fine	Fault gouge	Fault Zone	SAFOD core
GR4S3-Fine	Fault gouge	Fault Zone	SAFOD core
GR1S1-Fine	Cataclasite	Fault Zone	SAFOD core

*Parès et al., 2008

Total Organic Carbon Measurement

In preparation for analysis, samples were ground by hand in an agate mortar and pestle. Fault samples were separated into size fractions in order to isolate the clay mineral populations. Aliquots of ground samples treated with a solution of 5% HCl to remove carbonates, washed with deionized water, and vacuum filtered using a Millipore vacuum filtration system. Samples were then slowly dried under a low-intensity heat lamp (T<50°C). Approximately ~15mg to 100mg of treated, dried sample powder was loaded into tin foil capsules and analyzed on a Costech ECS4010 elemental analyzer in the University of Michigan's Earth System Science Lab. For Acetanilide standard (71.09 wt% C), the mean and standard deviation on replicate measurments (n=8) were 71.19 wt% C and 1.84 wt%, respectively.

Mercury Geochemistry Analyses

Mercury concentration measurements were done on a (Nippon Instruments, MA 2000) cold vapor atomic absorption spectrometer (CV-AAS). Solid samples were loaded into ceramic boats and combusted directly into the AAS line. Liberated Hg gas was collected on a gold trap. Concentrations are reported in ppb with an error < ~3 ppb based on replicate analyses.

Mercury isotopic compositions were determined using a Nu Instruments multi-collector inductively coupled plasma mass spectrometer (MC-ICP-MS). Measurements were made only on fault zone rock samples (cataclasite, gouge, and sheared host rock). Powdered sample material was loaded into ceramic boats and combusted in a dual-stage furnace at 750°C to volatilize mercury to Hg(0) gas. The mercury gas released was collected in an oxidizing $KMnO_4$ solution as Hg(II). $KMnO_4$ solutions were partially neutralized with hydroxylamine prior isotopic measurements. Combusted samples were reduced win $SnCl_2$ and re-transferred to a $KMnO_4$ solution and re-oxidized to Hg(II). The $KMnO_4$ solutions were then diluted to a constant Hg concentration for analysis with the MC-ICP-MS using continuous flow cold vapor generation with Sn(II) reduction. With the samples we also analyzed procedural blanks, UM-Almaden standards, and an internal lab standard (MESS-3). Isotopic compositions are reported in permil (‰) using delta-notation relative to the NIST SRM 3133 standard (Blum and Bergquist, 2007). Precision on the isotopic measurement of fault samples (n=7) is ±0.14‰ (2σ) for δ202, ±0.11‰ (2 σ) for Δ201, and ±0.11‰ (2σ) based on the long term average of measurements (n=8) for internal lab standard MESS-3 (mean measurements: δ202 = -2.22‰, Δ201 = 0.01‰, Δ199 = -0.01 ‰).

Results

Mercury Concentration

Mercury concentration in fault zone samples is generally higher than in host rock samples (Table D.2), though samples of lightly sheared host rock samples taken from the fault zone are approximately identical to undeformed host rocks samples. Additionally, several of the Franciscan samples have mercury concentrations that are comparable to those of the fault zone samples (Figure D.4). The cataclasite sample (GR1S1) has the highest concentration of mercury; two of the clay gouge samples (GR4S3 and GR2S8) have the next highest concentrations of mercury. Host rock samples all have concentrations <100 ppb.

Table D.2: Mercury concentration

Sample	Description	Hg (ng/g ± 1.7%)
4600 MD	Granite	38.5
4900 MD	Granodiorite	16.6
3400 MD	Granite	3.7
E1S1	Arkose	0.04
E1S4	Shale	22.7
F-1	Serpentinite	24.3
F-2	Greywacke	88.0
F-3	Blueschist	50.9
F-5	Cherty mudstone	68.1
F-6	Greywacke	61.0
B4R4	Granodiorite	36.6
G5S3	Siltstone	49.1
2002A	Siltstone	63.1
GR1S1-Coarse	Cataclasite	144.9
GR6S5-Coarse	Sheared claystone	35.2
GR6S5-Medium	Sheared claystone	43.0
GR6S5-Fine	Sheared claystone	32.0
GR2S8-Fine	Fault gouge	81.7
GR4S3-Fine	Fault gouge	143.2
GR1S1-Fine	Cataclasite	308.6

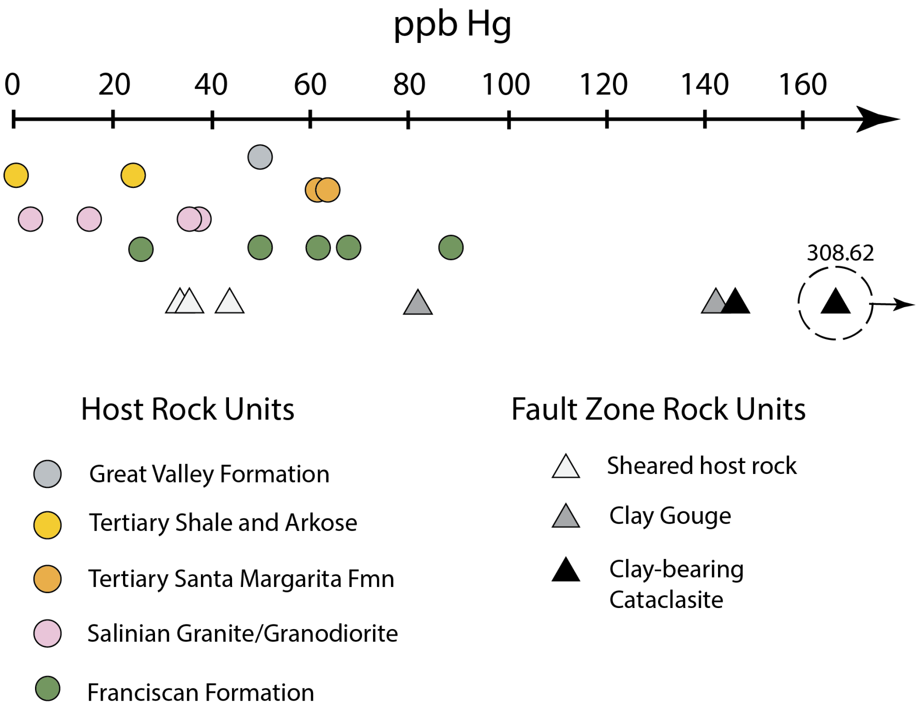

Figure D.4: Concentration of Mercury measured in SAFOD core samples. Circles represent samples not from the damage zone, triangles represent units taken from the damage zone. The sheared host rock samples have approximately the same concentration as the undamaged host rock units. The clay gouge samples are enriched in Mercury relative to the wall rock, and the clay-bearing cataclasite samples are even more enriched, with the most enriched sample (fined-grained size fraction from the cataclasite) charting off the end of the scale.

Total Organic Carbon

Twenty samples were measured for total organic carbon (TOC), including nine fault zone samples and eleven host rock samples (Table D.3, Figure D.5). Most samples have negligible amounts of organic carbon <1%, and all have <3%. Fault zone samples have larger amounts of organic carbon relative to host rock samples. Fine-grained samples generally have more organic carbon than coarse-grained samples and igneous/metamorphic crystalline samples.

A comparison between mercury concentration and wt% organic carbon shows that host rock samples have low concentrations of both organic carbon and mercury (Figure D.5). Fault rock samples have higher concentrations of organic carbon and mercury.

Sheared claystone samples from the fault zone have higher concentrations of organic carbon that does not correlate with increased concentration of mercury.

Table D.3: Organic carbon concentration		
Sample	Description	wt % Organic Carbon (±0.5%)
4600 MD	Granite	0.08
4900 MD	Granodiorite	0.06
3400 MD	Granite	0.09
E1S1	Arkose	0.05
E1S4	Shale	0.45
F-1	Serpentinite	0.04
F-2	Greywacke	0.06
F-3	Blueschist	0.24
F-5	Cherty mudstone	0.04
F-6	Greywacke	0.18
B4R4	Granodiorite	0.09
G5S3	Siltstone	0.28
2002a	Siltstone	0.49
GR1S1-Coarse	Cataclasite	1.29
GR6S5-Coarse	Sheared claystone	1.01
GR6S5-Medium	Sheared claystone	2.0
GR6S5-Fine	Sheared claystone	0.7
GR2S8-Fine	Fault gouge	1.75
GR4S3-Fine	Fault gouge	0.8
GR1S1-Fine	Cataclasite	2.65

Isotopic Composition

Isotopic composition of California rock units was completed by Smith et al. (2008) and is plotted with fault zone sample measurements in Figure D.6. Host rock samples generally exhibit a slightly negative MDF signature, with almost no MIF signature (note the difference in scale between MDF and MIF axes). Fault zone samples show an isotopic shift towards more negative MDF when compared to the host rock, shown by a blue arrow. As previously discussed, this shift corresponds with increasing mercury concentration in cataclasite and clay gouges samples. Sheared host rock from the fault zone shows little or no isotopic differentiation from relatively undeformed California country rock.

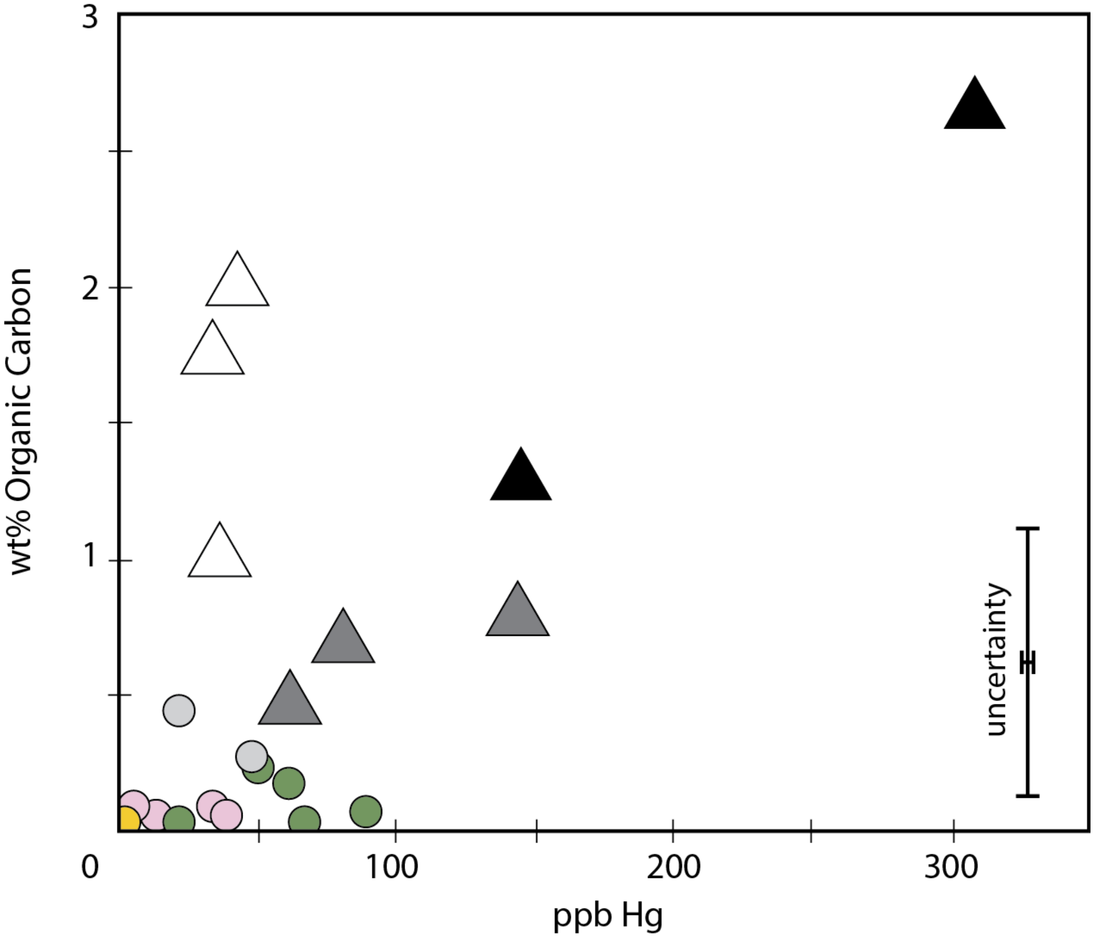

Figure D.5: Concentration of Mercury measured in SAFOD core samples. Circles represent samples not from the damage zone, triangles represent units taken from the damage zone. The sheared host rock samples have approximately the same concentration as the undamaged host rock units. The clay gouge samples are enriched in Mercury relative to the wall rock, and the clay-bearing cataclasite samples are even more enriched, with the most enriched sample (fined-grained size fraction from the cataclasite) charting off the end of the scale.

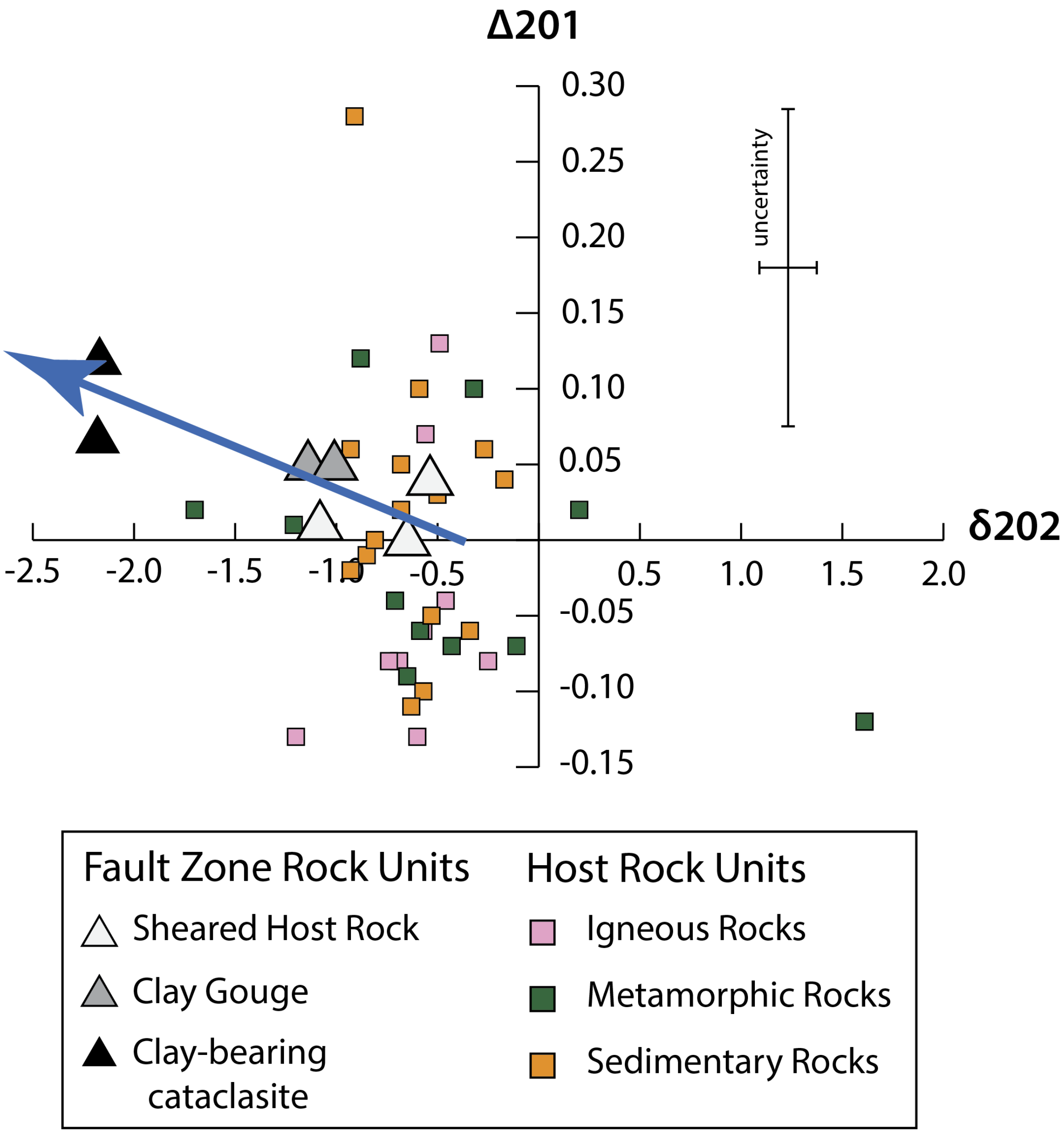

Figure D.6: Isotopic composition of Mercury in California country rocks. MDF signatures are shown on the x-axis; MIF signatures are shown on the y-axis. Colored squares (Smith et al., 2008) show the range of isotopic composition in the host rock units, grouped by rock type. Triangles show the composition of the SAFOD fault zone samples and have the same coloring as in Figure D.4 Note the difference in the scale of the axes (particularly the y-axis) relative to Figure D.1.

Discussion

The concentration of mercury in the fault rocks (Figure D.4) is enriched relative to the concentration of mercury in the host (wall) rocks from the SAFOD core. This enrichment of mercury in the fault zone suggests the mobilization of mercury into the fault zone, likely transported by fluids. The enrichment in mercury concentration in the fine fraction of the fault rock samples relative to the coarse fraction of the same sample could suggest that the mercury is hosted by clay minerals, due to the increased surface area available for adsorption with increasing proportion and decreasing size of clay minerals present in the rocks. Furthermore, the correlation between mercury content and organic carbon content could also suggest a relationship between mercury and organic material, possibly though binding with thiol (-SH) groups, which would be subsequently adsorbed to the charged clay mineral *001* surfaces. Alternatively, the organic matter and mercury could both be independently adsorbed to the clay minerals.

The isotopic composition of the sheared host rock and clay gouge from the damage zone of the San Andreas fault overlap with the isotopic composition of the host rock. The isotopic composition of clay-bearing cataclasite, however, has a more negative δ202 signature than that of the host rock. We interpret this enrichment to record the passage of larger volumes of mercury-rich and organic-rich fluids through the fault zone, which modified the isotopic composition of the fault rocks relative to the original isotopic composition of the rock units. Both the higher concentration of mercury and the larger isotopic depletion in the cataclasite relative to the fault gouge are likely due to the higher permeability of the cataclasite unit (Janssen et al., 2011; Morrow et al., 2014), which may have allowed larger volumes of fluid to infiltrate and migrate through it.

The negative δ202 signatures recorded in the fault rocks relative to the host rock could be due to one of three main possibilities (Figure D.7). The first hypothesis is that the signature could be imparted due to mixing of host rock signatures with an external mercury source. Mercury ore deposits in the coast range have been shown to exhibit a wide range of δ202 signatures (Blum et al., 2014), including signatures in the range of the mercury-enriched fault samples as well as signatures that are more negative. Though this may be one possible source, the bulk of the MDF signatures in the coastal range deposits is between 0 and -2.0‰, and does not overlap with our hypothetical external fluid source illustrated in Figure D.7. The second possibility is that the fractionation signatures due to processes that bind mercury to the host material in the fault zone. For instance, if mercury enrichment in the fault zone is a direct cause of hydrocarbon migration through the fault zone, fractionation may be caused by binding of the mercury to thiol (-SH) functional groups, which are common in most organic compounds. Wiederhold et al. (2010) observed a strong negative mass dependent fractionation and no significant mass independent fractionation associated with the binding of mercury to thiol groups. On the other hand, if adsorption of mercury to clay minerals is the main process that binds mercury and traps it in fault zones, a similar fractionation process may be occurring. Jiskra et al. (2012) described a negative mass dependent fractionation of mercury isotopes upon their adsorption to goethite, an iron oxyhydroxide mineral common in soils. They suggested that this adsorption fractionation process may apply to other fine-grained materials, such as clay minerals, causing soils (and perhaps clay-rich fault rocks) to be enriched in light isotopes. These two possibilities are represented by green arrows in Figure D.7.

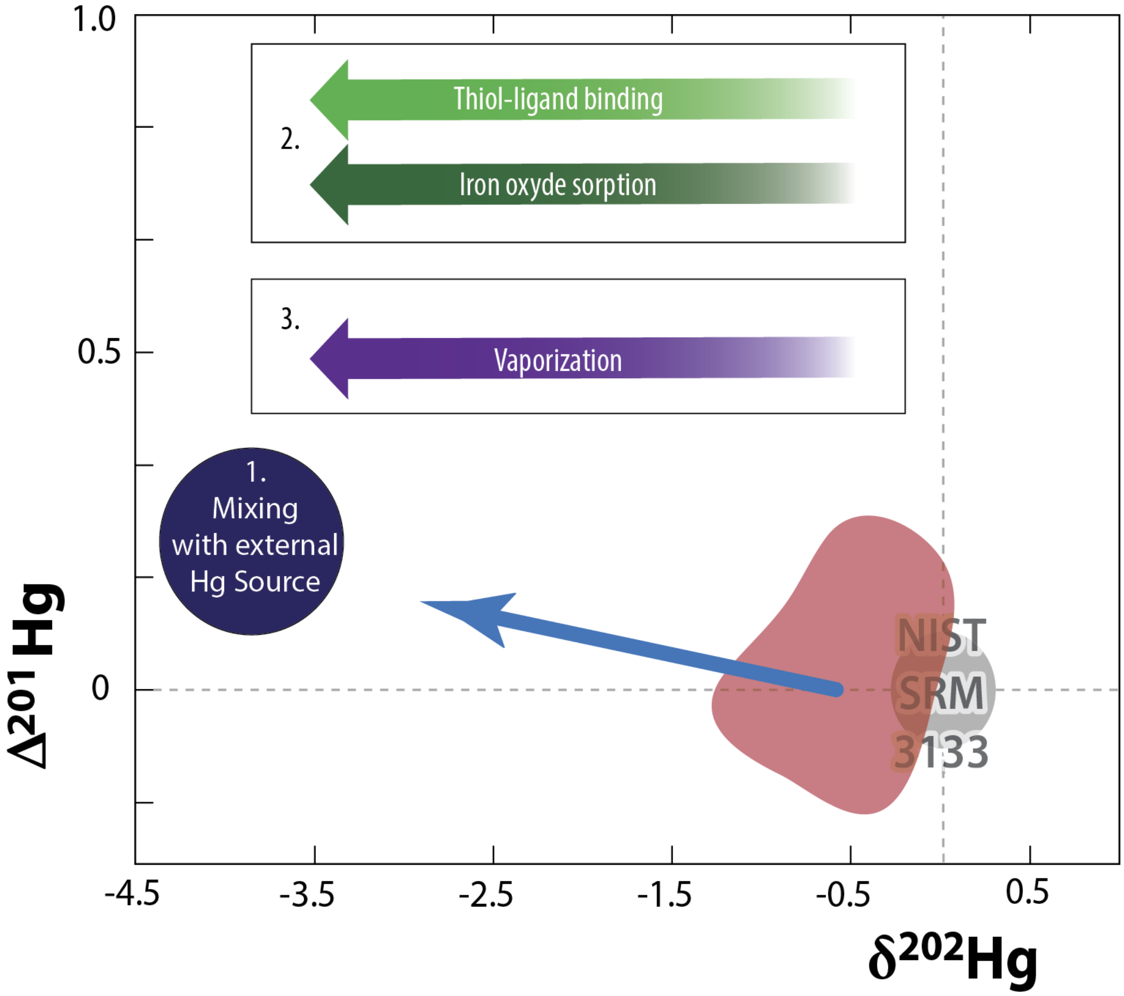

Figure D.7: Schematic representation of possible sources of for the mercury isotopic composition of San Andreas fault rock. The red shaded region represents the isotopic composition of California rock units. The blue arrow show the observed direction of MDF in SAFOD fault rocks. Hypothesis 1: Mercury source mixing is represented as a dark blue circle, showing the likely composition of the proposed external mercury source. Hypotheses 2: Fractionation due to mercury binding is shown by the green arrows. Light green represents fractionation related to the binding of mercury to organic matter, dark green represents that related to the adsorption of mercury to iron oxides and clay minerals. Hypothesis 3: fractionation due to the liberation of mercury from host rock by vaporization is shown as a purple arrow.

The third possible source of the fractionation signature is the complementary process to the binding mechanisms fractionation—mercury liberation and migration into the fault zone. Some studies have observed variation in groundwater chemistry during the earthquake cycle, suggesting that changes in crustal stress states and the resulting changes in the physical characteristics of the crust, cause changes in the mobility and transport of chemical species. Mercury concentration in groundwater has been shown to increase during times of fault activity (Yangfen et al., 1989). Changes in pressure and temperature during faulting may promote the vaporization of the fault fluid (Weatherley and Henley, 2013). This would cause deposition of dissolved species, in the case of silica or gold (Sibson, 1987; Weatherley and Henley, 2013), but in the case of Hg(0), it would instead cause vaporization of the mercury gas. Vaporization of mercury has been shown to cause a negative mass dependent fractionation (Zheng et al., 2007), which has been used to explain the negative MDF signatures in the mercury ores and sinters of the California coast ranges (Smith et al., 2005).

Based on the magnitude of the observed negative MDF, we favor a combination of both hypotheses 2 and 3. With the wealth of knowledge and isotopic measurements of potential mercury source rocks, we believe it unlikely that a large mercury source with the isotopic composition needed for mixing to create the isotopic compositions observed has not yet been identified. For this reason, we suggest that the isotopic composition of the fault rock is recording fault-related processes and fractionation due to mercury migration rather than mixing of multiple sources. Thiol ligand binding and iron oxide adsorption fractionation signatures have been estimated to produce negative MDF fractionations of ~0.53-0.63‰ and 0.30-0.44‰, respectively (Wiederhold et al., 2010; Jiskra et al., 2012). Vaporization has been estimated to produce a negative MDF of ~1-1.5‰ (Smith et al., 2005; Zheng et al., 2007). With an approximate host rock δ^{202}Hg signature of 0.5‰, a combination of both processes would produce a fractionation large enough to explain the ~-2‰ shift observed in the cataclasite samples.

Summary

Increased mercury content in fault rocks of the San Andreas Fault system indicates that fluid migration in the fault causes the mobilization of mercury into the fault zone, and its subsequent deposition by adsorption to clay minerals and binding to organic matter. The negative MDF signature associated with enriched mercury concentration gives clues to the fractionation processes that occur during mercury mobilization. With the observed magnitude of MDF, we favor the interpretation that mercury isotopic composition of the fault rock is dependent on migration-related fractionation processes, rather than due to mixing of an external mercury source. Further work is needed to distinguish between or to measure the relative contributions of the two proposed mechanisms for generating the negative MDF signature in fault rocks. Furthermore, due to the volatile and mobile nature of mercury, mass dependent isotopic fractionation modifies the original source signature, so we conclude that MDF is not a good source tracer for sub-surface fluids. However, with the potential to also record contrasting MIF signatures, which we did not find in this study, mercury isotopes my prove a useful source tracer in the future.

Additional work is under way to characterize the mercury isotopic composition of host rock.

Acknowledgements

The authors would like to acknowledge Anja Schleicher and Austin Boles for sample characterization and hydrogen isotope measurements for the fault zone samples. Thanks also to Kelly Bradbury for sharing additional samples from the SAFOD core outside of the fault zone. We would also like to thank Marcus Johnson, Aaron Kurz, Sophia Wensman, Neal Hughes, and Spencer Washburn for help and guidance in the Biogeochemistry and Environmental Isotope Geochemistry Lab at the University of Michigan. Lastly, we would like to acknowledge Nathan Sheldon and Katy Rico for their support and direction in collecting organic carbon concentration measurements. This project was supported by a Scott Turner student research grant to Lynch.

References

Allmendinger, R.W., and Judge, P.A., 2014, The Argentine Precordillera: A foreland thrust belt proximal to the subducted plate: Geosphere, v. 10, no. 6, p. 1–16, doi: 10.1130/GES01062.1.

Alvarez-Marron, J., Rodriguez-Fernandez, R., Heredia, N., Busquets, P., Colombo, F., and Brown, D., 2006, Neogene structures overprinting Palaeozoic thrust systems in the Andean Precordillera at 30°S latitude: Journal of the Geological Society, London, v. 163, p., 949-964, doi: 10.1144/0016-76492005-142.

Anastasio, D.J., Bebout, G.E., and Holl, J.E., 2004, Extra-basinal fluid infiltration, mass transfer, and volume strain during folding: Insights from the Idaho-Montana thrust belt: American Journal of Science, v. 304, no. 4, p. 333–369, doi: 10.2475/ajs.304.4.333.

Anderson, J.L., 1988. Core complexes of the Mojave-Sonoran desert: Conditions of plutonism, mylonitization and decompression. In: Metamorphism and crustal evolution of the western United States (Ernst, W., ed.), p. 503-525. Rubey Volume VII, Prentice Hall.

Anderson, R. E., 1971. Thin skin distension in Tertiary rocks of southeastern Nevada. Geological Society of America Bulletin 82, p. 43-58.

Andrew, J., Walker, J., 2009, Reconstructing late Cenozoic deformation in central Panamint Valley, California: Evolution of slip partitioning in the Walker Lane. Geosphere v. 5, p. 172-198.

Atnipp, V.A., 1988, Timing and fluid sources of vein mineralization in the Wyoming overthrust belt, Masters thesis, 33 pages. University of Michigan, Ann Arbor, MI.

Axen, G., 2004, Mechanics of low-angle normal faults. in Rheology and Deformation of the Lithosphere at Continental Margins (eds. Karner, G., Taylor, B., Driscoll, N., Kohlstedt, D.) New York, Columbia Univ. Press. P. 46 – 91.

Aydin, A., 2000, Fractures, faults, and hydrocarbon entrapment, migration and flow: Marine and Petroleum Geology, v. 17, no. 7, p. 797–814, doi: 10.1016/S0264-8172(00)00020-9.

Bailey, R.C., 1990, Trapping of aqueous fluids in the deep crust: Geophysical Research Letters, v. 17, no. 8, p. 1129-1132, doi: 10.1029/GL017i008p01129

Barker, A.J., Bennett, D.G., Boyce, A.J., and Fallick, A.E., 2000, Retrogression by deep infiltration of meteoric fluids into thrust zones during late-orogenic rapid unroofing: Journal of Metamorphic Geology, v. 18, no. 3, p. 307–318.

Barnett, D., Bowman, J., Bromley, C., Cady, C., 1996. Kinetically limited isotope exchange in a shallow level normal fault, Mineral Mountains, Utah. J. Geophy. Res. B v. 101, p. 673-685.

Bebout, G.E., Anastasio, D.J., and Holl, J.E., 2001, Synorogenic crustal fluid infiltration in the Idaho-Montana Thrust Belt: Geophysical Research Letters, v. 28, no. 22, p. 4295–4298, doi: 10.1029/2001GL013711.

Becken, M., Ritter, O., Park, S.K., Bedrosian, P.A., Weckmann, U., and Weber, M., 2008, A deep crustal fluid channel into the San Andreas Fault system near Parkfield, California: Geophysical Journal International, v. 173, no. 2, p. 718–732, doi: 10.1111/j.1365-246X.2008.03754.x.

Beer, J.A., 1990, Steady sedimentation and lithologic completeness, Bermejo Basin, Argentina: The Journal of Geology, v. 98, no. 4, p. 501-517.

Bergmann, J., 2005, Rietveld Analysis Program BGMN Manual: Dresden, Germany.

Bergmann, J., Friedel, P., and Kleeberg, R., 1998, BGMN—a new fundamental parameter based Rietveld program for laboratory X-ray sources, its use in quantitative analysis and structure investigations: CPD Newsletter, Commission of Powder Diffraction, International Union of Crystallography, v. 20, p. 5-8.

Bergquist, B.A., and Blum, J.D., 2007, Mass-dependent and -independent fractionation of Hg isotopes by photoreduction in aquatic systems: Science, v. 318, no. 5849, p. 417-420, doi: 10.1126/science.1148050

Bethke, C.M., and Marshak, S., 1990, Brine migrations across North America - the plate tectonics of groundwater: Annual Review of Earth and Planetary Sciences, v. 18, no. 1, p. 287–315, doi: 10.1146/annurev.ea.18.050190.001443.

Bird, J.M., and Dewey, J.F., 1970, Lithosphere Plate-Continental Margin Tectonics and the Evolution of the Appalachian Orogen: Geological Society of America Bulletin, v. 81, p. 1031–1060.

Biswas, A., Blum, J.D., Bergquist, B.A., Keeler, G.J., and Zhouqing, X., 2008, Natural mercury isotope variation in coal deposits and organic soils: Environmental Science and Technology, v. 42, p. 8303–8309.

Blackner, G.C., Omar, G.I., and Gold, D.P., 1994, Post-Alleghanian Unroofing Histroy of the Appalachian Basin, Pennsylvania, From Apatite Fission Track Analysis and Thermal Models: Tectonics, v. 13, no. 5, p. 1259–1276.

Blackwell, D.D., Smith, R.P., and Richards, M.C., 2007, Exploration and development at Dixie Valley, Nevada: Summary of DOE studies: Stanford, California, Proceedings, Thirty-Second Workshop on Geothermal Reservoir Engineering, Stanford University, January 22–24, SGP-TR-183.

Blanpied, M.L., Lockner, D.A., and Byerlee, J.D., 1992, An earthquake mechanism based on rapid sealing of faults: Nature, v. 358, no. 6387, p. 574–576, doi: 10.1038/358574a0.

Blum, J.D., and Bergquist, B.A., 2007, Reporting of variations in the natural isotopic composition of mercury: Analytical and Bioanalytical Chemistry, v. 388, no. 2, p. 353–359, doi: 10.1007/s00216-007-1236-9.

Blum, J.D., Sherman, L.S., and Johnson, M.W., 2014, Mercury Isotopes in Earth and Environmental Sciences: Annual Review of Earth and Planetary Sciences, v. 42, no. 1, p. 249–269, doi: 10.1146/annurev-earth-050212-124107.

Boles, A.H., 2017, Clay Neomineralization and the Timing, Thermal Conditions and geofluids History of Upper Crustal Deformation Zones, Ph.D. dissertation, 178 pages. University of Michigan, Ann Arbor, MI.

Boles, A., Mulch, A., and van der Pluijm, B.A., 2018, Near-surface clay authigenesis in exhumed fault rock of the Alpine Fault Zone (New Zealand); O-H-Ar isotopic, XRD and chemical analysis of illite and chlorite: Journal of Structural Geology, v. 111, p. 27–41, doi: 10.1016/j.jsg.2018.03.008.

Boles, A., van der Pluijm, B., Mulch, A., Mutlu, H., Uysal, T., Warr, L., 2015. Hydrogen and ^{40}Ar/^{39}Ar isotope evidence for multiple and protracted paleofluid flow events within the long-lived North Anatolian Keirogen (Turkey).

Bowen, G.J., and Revenaugh, J., 2003, Interpolating the isotopic composition of modern meteoric precipitation: Water Resources Research, v. 39, no. 10, doi: 10.1029/2003WR002086.

Boyer, S.E., and Elliott, D., 1982, Thrust systems: American Association of Petroleum Geologists Bulletin, v. 66, no. 9, p. 1196–1230.

Bradbury, H.J and Woodwell, G.R., 1987, Ancient fluid flow within foreland terrains: Geological Society, London, Special Publications, v. 34, p. 87–102, doi: 10.1144/GSL.SP.1987.034.01.07.

Bradbury, K.K., Barton, D.C., Solum, J.G., Draper, S.D., and Evans, J.P., 2007, Mineralogic and textural analyses of drill cuttings from the San Andreas Fault Observatory at Depth (SAFOD) boreholes: Initial interpretations of fault zone composition and constraints on geologic models: Geosphere, v. 3, no. 5, p. 299–20, doi: 10.1130/GES00076.1.

Burtner, R.L., and Nigrini, A., 1994, Thermochronology of the Idaho-Wyoming Thrust Belt During the Sevier Orogeny: A New, Calibrated, Multiprocess Thermal Model: AAPG Bulletin, v. 78, no. 10, p. 1586–1612.

Byerlee, J., 1993, Model for episodic flow of high-pressure water in fault zones before earthquakes: Geology, v. 21, no. 4, p. 303–306, doi: 10.1130/0091-7613(1993)021<0303:MFEFOH>2.3.CO;2.

Cadrin, A., Kyser, T., Caldwell, W., Longstaffe, F., 1995. Isotopic and chemical composition of bentonites as paleoenvironmental indicators of the Cretaceous Western Interior Seaway. Paleogeography, Paleoclimatology, Paleoecology 119, p. 301-320.

Caine, J.S., Evans, J.P., and Forster, C.B., 1996, Fault zone architecture and permeability structure: Geology, v. 24, no. 11, p. 1025–1028, doi: 10.1130/0091-7613(1996)024<1025:FZAAPS>2.3.CO;2.

Campani, M., Mulch, A., Kempf, O., Schlunegger, F., Mancktelow, N., 2012, Miocene paleotopography of the Central Alps: Earth and Planetary Science Letters, v. 337-338, p. 174-185, doi: 10.1016/j.epsl.2012.05.017.

Capuano, R., 1992. The temperature dependence of hydrogen isotope fractionation between clay minerals and water: Evidence from a geopressured system. Geochim. et Cosmochim. Acta. V. 56, p. 2547-2554.

Carpenter, B., Marone, C., Saffer, D., 2011. Weakness of the San Andreas Fault revealed by samples from the active fault zone. Nature Geoscience 4, 251–254.

Cederquist, D.P., Van der Voo, R., and van der Pluijm, B.A., 2006, Syn-folding remagnetization of Cambro-Ordovician carbonates from the Pennsylvania Salient post-dates oroclinal rotation: Tectonophysics, v. 422, no. 1-4, p. 41–54, doi: 10.1016/j.tecto.2006.05.005.

Cerling , T.E., Harris, J.M., MacFadden B.J. , Leakey, M.G., Quade, J., Eisenmann, V., and Ehleringer, J.R., 1997, Global vegetation change through the Miocene/Pliocene boundary: Nature, v. 389, p.153-158.

Chacko, T., Cole, D.R. and Horita, J., 2001, Equilibrium oxygen, hydrogen and carbon isotope fractionation factors applicable to geologic systems: Reviews in Mineralogy and Geochemistry, v. 43, p. 1–81.

Chamberlain, C.P., Poage, M.A., Craw, D., and Reynolds, R.C., 1999, Topographic development of the Southern Alps recorded by the isotopic composition of authigenic clay minerals, South Island, New Zealand: Chemical Geology, v. 155, no. 3-4, p. 279–294, doi: 10.1016/S0009-2541(98)00165-X.

Chamberlain, C.P., Mix, H.T., Mulch, A., Hren, M.T., Kent-Corson, M.L., Davis, S.J., Horton, T.W., and Graham, S.A., 2012, The Cenozoic climatic and topographic evolution of the western North American Cordillera: American Journal of Science, v. 312, no. 2, p. 213–262, doi: 10.2475/02.2012.05.

Chamberlain, R.T., 1910, The Appalachian Folds of Central Pennsylvania: The Journal of Geology, v. 18, no. 3, p, 228-251.

Chester, F.M., and Logan, J.M., 1987, Composite planar fabric of gouge from the Punchbowl Fault, California: Journal of Structural Geology, v. 9, no. 5-6, p. 621–634, doi: 10.1016/0191-8141(87)90147-7.

Clark, C., Hand, M., Faure, K., Schmidt Mumm, A., 2006. Up-temperature flow of surface-derived fluids in the mid-crust: the role of pre-orogenic burial of hydrated fault rocks. J. Metamorphic Geology 24, p. 367-387.

Clauer, N., Zwingmann, H., Liewig, N., and Wendling, R., 2012, Comparative 40Ar/39Ar and K–Ar dating of illite-type clay minerals: A tentative explanation for age identities and differences: Earth Science Reviews, v. 115, no. 1-2, p. 76–96, doi: 10.1016/j.earscirev.2012.07.003.

Clauer, N., Fallick, A.E., Eberl, D.D., Honty, M., Huff, W.D., and Aubert, A., 2013, K-Ar dating and δ^{18}O-δD characterization of nanometric illite from Ordovician K-bentonites of the Appalachians: Illitization and the Acadian-Alleghenian tectonic activity: American Mineralogist, v. 98, no. 11-12, p. 2144–2154, doi: 10.2138/am.2013.4510.

Clayton, R., Friedman, I., Graf, D., Mayeda, T., Meents, W., Schimp, N., 1966. The origin of saline formation waters. 1. Isotopic composition. J. Geophysical Research B 71, p. 3869-3882.

Cole, D., and Ripley, E., 1998, Oxygen isotope fractionation between chlorite and water from 170 to 350C: A preliminary assessment based on partial exchange and fluid/rock experiments: Geochimica and Cosmochimica Acta, v. 63, p. 449–457.

Colgan, J., and Metcalf, J., 2006. Rapid middle Miocene unroofing of the southern Ruby Mountains, Nevada: Geological Society of America Abstracts with Programs, v. 38, no. 7, p. 417.

Collettini, C., 2011. The mechanical paradox of low-angle normal faults: Current understanding and open questions. Tectonophysics v. 510, p. 253-268.

Connolly, C.A., Walter, L.M., Baadsgaard, H., and Longstaffe, F.J., 1990, Origin and evolution of formation waters, Alberta Basin, Western Canada Sedimentary Basin. II. Isotope systematics and water mixing: Applied Geochemistry, v. 5, no. 4, p. 397–413, doi: 10.1016/0883-2927(90)90017-Y.

Connolly, J.A.D., 1997, Devolatilization-generated fluid pressure and deformation-propagated fluid flow during prograde regional metamorphism: Journal of Geophysical Research, v. 102, no. B8, p. 18149-18173, doi: 10.1029/97JB00731.

Connolly, J.A.D., 2010, The Mechanics of Metamorphic Fluid Expulsion: Elements, v. 6, no. 3, p. 165–172, doi: 10.2113/gselements.6.3.165.

Connolly, J., and Podladchikov, Y., 2004. Fluid flow in compressive tectonic settings: Implications for midcrustal seismic reflectors and downward fluid migration. J. Geophysical Research B 109, doi:10.1029/2003JB002822.

Constenius, K.N., Johnson, R.A., Dickinson, W.R., Williams, T.A., 2000. Tectonic evolution of the Jurassic–Cretaceous Great Valley forearc, California: implications for the Franciscan thrust-wedge hypothesis: GSA Bulletin, v. 112, p. 1703–1723, doi: 10.1130/0016-7606(2000)112<1703:TEOTJC>2.0.CO;2.

Cooley, M.A., Price, R.A., Kyser, T.K., and Dixon, J.M., 2011, Stable-isotope geochemistry of syntectonic veins in Paleozoic carbonate rocks in the Livingstone Range anticlinorium and their significance to the thermal and fluid evolution of the southern Canadian foreland thrust and fold belt: AAPG Bulletin, v. 95, no. 11, p. 1851–1882, doi: 10.1306/01271107098.

Cooper, M., 2007, Structural style and hydrocarbon prospectivity in fold and thrust belts: a global review: Geological Society London, Special Publications, v. 272, no. 1, p. 447–472, doi: 10.1144/GSL.SP.2007.272.01.23.

Craddock, J.P., 1988, Geologic Map, Cross Section, and Meso-structures Across the Idaho-Wyoming Fold-and-thrust Belt at Latitude 42° 45′: Geological Society of America Map and Chart Series, MCH067, 18p.

Craw, D., 1988, Shallow-level metamorphic fluids in a high uplift rat metamorphic belt; Alpine Schist, New Zealand: Journal of Metamorphic Geology, v. 6, no. 1, p. 1–16, doi: 10.1111/j.1525-1314.1988.tb00405.x.

Craw, D., Koons, P.O., Horton, T.W., and Chamberlain, C.P., 2002, Tectonically driven fluid flow and gold mineralisation in active collisional orogenic belts: comparison between New Zealand and western Himalaya: Tectonophysics, v. 348, no. 1-3, p. 135–153.

Crittenden, M. et al., 1980 (eds). Cordilleran metamorphic core complexes. Geological Society of America Memoir 153, 400 pp.

Dahlen, F.A., Suppe, J., and Davis, D., 1984, Mechanics of fold-and-thrust belts and accretionary wedges: Cohesive Coulomb theory: Journal of Geophysical Research, v. 89, no. B12, p. 10087–10101.

Dallmeyer, R.D., 1982, ^{40}Ar/^{39}Ar ages from the Narragansett Basin and southern Rhode Island basement terrane: Their bearing on the extent and timing of Alleghenian tectonothermal events in New England: Geological Society of America Bulletin, v. 93, no. 11, p. 1118–1130, doi: 10.1130/0016-7606(1982)93<1118:AAFTNB>2.0.CO;2.

Dansgaard, W., 1964, Stable isotopes in precipitation: Tellus, v. 16, no. 4, p. 436–468, doi: 10.3402/tellusa.v16i4.8993.

Davis, D., Suppe, J., and Dahlen, F.A., 1983, Mechanics of fold-and-thrust belts and accretionary wedges: Journal of Geophysical Research, v. 88, no. B2, p. 1153–1172.

De Caritat, P., Hutcheon, I., and Walshe, J.L., 1993, Chlorite Geothermometry - a Review: Clays and Clay Minerals, v. 41, no. 2, p. 219–239.

DeCelles, P.G., 1994, Late Cretaceous-Paleocene synorogenic sedimentation and kinematic history of the Sevier thrust belt, northeast Utah and southwest Wyoming: Geological Society of America Bulletin, v. 106, no. 1, p. 32-56, doi: 10.1130/0016-7606(1994)106<0032:LCPSSA>2.3.CO;2.

Deming, D., 1994, Fluid flow and heat transport in the upper continental crust: Geological Society London, Special Publications, v. 78, no. 1, p. 27–42, doi: 10.1144/GSL.SP.1994.078.01.04.

Deming, D., and Chapman, D., 1989, Thermal histories and hydrocarbon generation: and example from Utah-Wyoming thrust belt: AAPG Bulletin, v. 73, no. 12, p. 1455-1471, doi: 10.1306/44B4AA6E-170A-11D7-8645000102C1865D.

Dettman, D.L., and Lohmann, K.C., 1993, Seasonal change in Paleogene surface water del18O: Fresh-water bivalves of western North America *in* P. K. Swart, K. C. Lohmann, J. Mckenzie, and S. M. Savin, eds.: Geophysical Monograph, v. 78, p. 153–163.

Dettman, D.L., and Lohmann, K.C., 2000, Oxygen isotope evidence for high-altitude snow in the Laramide Rocky Mountains of North America during the Late Cretaceous and Paleogene: Geology, v. 28, no. 3, p. 243–246, doi: 10.1130/0091-7613(2000)28<243:OIEFHS>2.0.CO;2.

De Segonzac, G.D., 1970, The transformation of clay minerals during diagenesis and low-grade metamorphism: A review: Sedimentology, v. 15, no. 3-4, p. 281–346, doi: 10.1111/j.1365-3091.1970.tb02190.x.

de Witt, Jr., W. and Milici, R.C.,1989, Energy resources of the Appalachian orogen: in Hatcher Jr, R.D., Thomas, W.A. and Viele, G.E., eds., The Appalachian-Ouachita Orogen in the United States, The Geology of North America Volume F-2*:* Geological Society of America, Boulder, Colorado, p. 495-510.

Doebelin, N., and Kleeberg, R., 2015, Profex: a graphical user interface for the Rietveld refinement program BGMN: Journal of Applied Crystallography, v. 48, p. 1573-1580, p. 1–8, doi: 10.1107/S1600576715014685.

Dong, H., Hall, C.M., Peacor, D.R., and Halliday, A.N., 1995, Mechanisms of argon retention in clays revealed by laser ^{40}Ar-^{39}Ar dating: Science, v. 267, no. 5196, p. 355–359, doi: 10.1126/science.267.5196.355.

Dong, H., Hall, C.M., Halliday, A.N., and Peacor, D.R., 1997, 40Ar/39Ar illite dating of Late Caledonian (Acadian) metamorphism and cooling of K-bentonites and slates from the Welsh Basin, UK: Earth and Planetary Science Letters, v. 150, no. 3-4, p. 337–351, doi: 10.1016/S0012-821X(97)00100-3.

Dworkin, S.I., 1999, Geochemical constraints on the origin of thrust fault fluids: Geophysical Research Letters, v. 26, no. 24, p. 3665–3668, doi: 10.1029/1999GL008377.

Engelder, J.T., 1974, Cataclasis and the generation of fault gouge: Geological Society of America Bulletin, v. 85, p. 1515–1522.

Engelder, T., 1984, The role of pore water circulation during the deformation of foreland fold and thrust belts: Journal of Geophysical Research: Solid Earth (1978–2012), v. 89, no. B6, p. 4319–4325, doi: 10.1029/JB089iB06p04319.

England, T.D.J., and Bustin, R.M., 1986, Effect of thrust faulting on organic maturation in the southeastern Canadian Cordillera: Organic Geochemistry, v. 10, no. 1-3, p. 609–616, doi: 10.1016/0146-6380(86)90057-4.

Engstrom, D.R., 2007, Fish respond when the mercury rises: Proceedings of the National Academy of Sciences of the United States of America, v. 104, no. 42, p. 16394–16395, doi: 10.1073/pnas.0708273104.

Enkin, R.J., Osadetz, K., Baker, J., and Kisilevsky, D., 2000, Orogenic remagnetizations in the Front Ranges and inner Foothills of the southern Canadian Cordillera: Chemical harbinger and thermal handmaiden of Cordilleran deformation: Bulletin of the Geological Society of America, v. 112, no. 6, p. 929–942, doi: 10.1130/0016-7606(2000)112<929:ORITFR>2.0.CO;2.

Epstein, A.G., Epstein, J.B., and Harris,.J.A., 1977, Conodont color alteration--an index to organic metamorphism: Geological Survey Professional Paper, v. 995, p. 1–27.

Etheridge, M.A., Wall, V.J., and Vernon, R.H., 1983, The role of the fluid phase during regional metamorphism and deformation: Journal of Metamorphic Geology, v. 1, no. 3, p. 205–226, doi: 10.1111/j.1525-1314.1983.tb00272.x.

Etheridge, M.A., Wall, V.J., Cox, S.F., and Vernon, R.H., 1984, High fluid pressures during regional metamorphism and deformation: Implications for mass transport and deformation mechanisms: Journal of Geophysical Research, v. 89, no. B6, p. 4344–4358, doi: 10.1029/JB089iB06p04344.

Evans, J.P., Forster, C.B., and Goddard, J.V., 1997, Permeability of fault related rocks, and implications for hydraulic structure of fault zones: Journal of Structural Geology, v. 19, no. 11, p. 1393-1404, doi: 10.1016/S0191-8141(97)00057-6.

Evans, M.A., 1989, The structural geometry and evolution of foreland thrust systems, northern Virginia: Bulletin of the Geological Society of America, v. 101, no. 3, p. 339–354, doi: 10.1130/0016-7606(1989)101<0339:TSGAEO>2.3.CO;2.

Evans, M.A., 2010, Temporal and spatial changes in deformation conditions during the formation of the Central Appalachian fold-and-thrust belt: Evidence from joints, vein mineral paragenesis, and fluid inclusions, *in* Tollo, R.P., Bartholomew, M.J., Hibbard, J.P., and Karabinos, P.M., eds., From Rodinia to Pangea: The Lithotectonic Record of the Appalachian Region: Geological Society of America Memoir 206, p. 477–552, doi: 10.1130/2010.1206(21)

Evans, M.A., and Battles, D.A., 1999, Fluid inclusion and stable isotope analyses of veins from the central Appalachian Valley and Ridge province: Implications for regional synorogenic hydrologic structure and fluid migration: Geological Society of America Bulletin, v.111, no. 12, p. 1841–1860.

Evans, M.A., Bebout, G.E., and Brown, C.H., 2012, Changing fluid conditions during folding: An example from the central Appalachians: Tectonophysics, v. 576-577, p. 99–115, doi: 10.1016/j.tecto.2012.03.002.

Faill, R.T., 1997a, A geologic history of the north-central Appalachians. Part 1. Orogenesis from the Mesoproterozoic through the Taconic orogeny: American Journal of Science, v. 297, p. 551-619.

Faill, R.T., 1997b, A geologic history of the north-central Appalachians. Part 2. The Appalachian Basin from the Silurian through the Carboniferous: American Journal of Science, v. 297, p. 729-761.

Faill, R.T., 1998, A geologic history of the north-central Appalachians. Part 3. The Alleghany orogeny: American Journal of Science, v. 298, p. 131-179.

Fan, M., and Dettman, D.L., 2009, Late Paleocene high Laramide ranges in northeast Wyoming: Oxygen isotope study of ancient river water: Earth and Planetary Science Letters, v. 286, no. 1-2, p. 110–121, doi: 10.1016/j.epsl.2009.06.024.

Farrar, S.S., 1985, Tectonic evolution of the easternmost Piedmont, North Carolina: Bulletin of the Geological Society of America, v. 96, no. 3, p. 362–380, doi: 10.1130/0016-7606(1985)96<362:TEOTEP>2.0.CO;2.

Faulkner, D.R, Jackson, C.A.L, Lunn, R.J., Schlische, R.W., Shipton, Z.K., Wibberley, C.A.J., and Withjack, M.O., 2010,A review or recent developments concerning the structure, mechanics and fluid flow properties of fault zones: Journal of Structural Geology, v. 32, p. 1557–1575, doi: 10.1016/j.jsg.2010.06.009.

Feinstein, S., Kohn, B., Osadetz, K., and Price, R.A., 2007, Thermochronometric reconstruction of the prethrust paleogeothermal gradient and initial thickness of the Lewis thrust sheet, southeastern Canadian Cordillera foreland belt, in Special Paper 433: Whence the Mountains? Inquiries into the Evolution of Orogenic Systems: A Volume in Honor of Raymond A. Price, Geological Society of America, p. 167–182, doi: 10.1130/2007.2433(08).

Feiss, P.G., and Slack, J.F.,1989, Mineral deposits of the U.S. Appalachians: in Hatcher Jr, R.D., Thomas, W.A. and Viele, G.E., eds., The Appalachian-Ouachita Orogen in the United States, The Geology of North America Volume F-2*:* Geological Society of America, Boulder, Colorado, p. 479-494.

Feng, R., Poulsen, C.J., Werner, M., Chamberlain, C.P., Mix, H.T., and Mulch, A., 2013, Early Cenozoic evolution of topography, climate, and stable isotopes in precipitation in the North American Cordillera: American Journal of Science, v. 313, no. 7, p. 613–648, doi: 10.2475/07.2013.01.

Feng, X., Foucher, D., Hintelmann, H., Yan, H., He, T., and Qiu, G., 2010, Tracing Mercury Contamination Sources in Sediments Using Mercury Isotope Compositions: Environmental Science & Technology, v. 44, no. 9, p. 3363–3368, doi: 10.1021/es9039488.

Ferry, J.M., 1988, Infiltration-driven metamorphism in northern New England, USA: Journal of Petrology, v. 29, no. 6, p. 1121–1159, doi: 10.1093/petrology/29.6.1121.

Ferry, J.M., 1994, Overview of the petrological record of fluid flow during regional metamorphism in northern New England: American Journal of Science, v. 294, p. 905–998, doi: 10.2475/ajs.294.8.905.

Ferry, J.M., and Gerdes, M.L., 1998, Chemically reactive fluid flow during metamorphism: Annual Review of Earth and Planetary Sciences, v. 26, p. 255–287, doi: 10.1146/annurev.earth.26.1.255.

Fitz-Diaz, E., Hudleston, P., Siebenaller, L., Kirschner, D.L., Camprubí, A., Tolson, G., and Puig, T.P., 2011, Insights into fluid flow and water-rock interaction during deformation of carbonate sequences in the Mexican fold-thrust belt: Journal of Structural Geology, v. 33, no. 8, p. 1237–1253, doi: 10.1016/j.jsg.2011.05.009.

Fitz-Diaz, E., and van der Pluijm, B.A., 2013, Fold dating: A new Ar/Ar illite dating application to constrain the age of deformation in shallow crustal rocks: Journal of Structural Geology, v. 54, no. C, p. 174–179, doi: 10.1016/j.jsg.2013.05.011.

Fitz-Diaz, E., Camprubí, A., Cienfuegos-Alvarado, E., Morales-Puente, P., Schleicher, A.M., and van der Pluijm, B.A., 2014, Newly-formed illite preserves fluid sources during folding of shale and limestone rocks; an example from the Mexican Fold-Thrust Belt: Earth and Planetary Science Letters, v. 391, no. C, p. 263–273, doi: 10.1016/j.epsl.2013.12.025.

Flower, B.P., and Kennett, J.P., 1994, The Middle Miocene climatic transition - east Antarctic ice-sheet development, deep-ocean circulation and global carbon cycling: Palaeogeography Palaeoclimatology Palaeoecology, v. 108, no. 3-4, p. 537–555, doi: 10.1016/0031-0182(94)90251-8.

Foreman, B.Z., Fricke, H.C., Lohmann, K.C., and Rogers, R.R., 2011, Reconstructing Paleocatchments by integrating stable isotope records, sedimentology and taphonomy: A Late Cretaceous case study (Montana, United States): Palaios, v. 26, no. 9/10, p. 545–554, doi: 10.2110/palo.2010.p10-133r.

Foucher, D., Ogrinc, N., and Hintelmann, H., 2008, Tracing Mercury Contamination from the Idrija Mining Region (Slovenia) to the Gulf of Trieste Using Hg Isotope Ratio Measurements: Environmental Science & Technology, v. 43, p. 33–39, doi: 10.1021/es801772b.

Fricke, H.C., 2003, Investigation of early Eocene water-vapor transport and paleoelevation using oxygen isotope data from geographically widespread mammal remains: Geological Society of America Bulletin, v. 115, no. 9, p. 1088-1096, doi: 10.1130/B25249.1.

Fricke, H.C., Foreman, B.Z., and Sewall, J.O., 2010, Integrated climate model-oxygen isotope evidence for a North American monsoon during the Late Cretaceous: Earth and Planetary Science Letters, v. 289, no. 1-2, p. 11–21, doi: 10.1016/j.epsl.2009.10.018.

Fricke, H.C., Rogers, R.R., Backlund, R., Dwyer, C.N., and Echt, S., 2008, Preservation of primary stable isotope signals in dinosaur remains, and environmental gradients of the Late Cretaceous of Montana and Alberta: Palaeogeography Palaeoclimatology Palaeoecology, v. 266, no. 1-2, p. 13–27, doi: 10.1016/j.palaeo.2008.03.030.

Fricke, H., Wickham, S., O'Neil, J., 1992, Oxygen and hydrogen isotope evidence for meteoric water infiltration during mylonitization and uplift in the Ruby Mountains-East Humboldt Range core complex, Nevada, Contrib. Mineral. Petrol. v. 111, p. 203 – 221.

Friedman, I., Smith, G.I., Gleason, J., Warden, A., and Harris, J.M., 1992, Stable Isotope Composition of Waters in Southeastern California, 1. Modern Precipitation: Journal of Geophysical Research: Atmospheres, v. 97, no. D5, p. 5795–5812, doi: 10 .1029 /92JD00184.

Friedman, I., Smith, G.I., Johnson, C.A., and Moscati, R.J., 2002, Stable isotope compositions of waters in the Great Basin, United States, 2. Modern precipitation: Journal of Geophysical Research: Atmospheres, v. 107, no. D19, p. ACL 15-1–ACL 15-22, doi: 10.1029 /2001JD000566.

Fyfe, W.S., and Kerrich, R., 1985, Fluids and thrusting: Chemical Geology, v. 49, no. 1-3, p. 353–362, doi: 10.1016/0009-2541(85)90167-6.

Garven, G., 1985, The role of regional fluid flow in the genesis of the Pine Point deposit, western Canada sedimentary basin: Economic Geology, v. 80, p. 307–324.

Garven, G., 1995, Continental-scale groundwater flow and geologic processes: Annual Review of Earth and Planetary Sciences, v. 23, p. 89–117.

Garven, G., and Freeze, R.A., 1984, Theoretical analysis of the role of groundwater flow in the genesis of stratabound ore deposits. 1. Mathematical and numerical model.: American Journal of Science, v. 284, no. 10, p. 1085–1124, doi: 10.2475/ajs.284.10.1085.

Gat, J.R., 1996, Oxygen and hydrogen isotopes in the hydrologic cycle: Annual Review of Earth and Planetary Sciences, v. 24, p. 225-262.

Ge, S and Garven, G., 1989, Tectonically Induced Transient Groundwater Flow in Foreland Basin: Geophysical Monograph Series, v. 14, no. 3, p.145-157, doi: 10.1029/GM048p0145.

Ge, S., and Garven, G., 1994, A theoretical model for thrust-induced deep groundwater expulsion with application to the Canadian Rocky Mountains: Journal of Geophysical Research, v. 99, no. B7, p. 13,851–13,868.

Gébelin, A., Mulch, A., Teyssier, C., Heizler, M., Vennemann, T., and Seaton, N.C.A., 2011, Oligo-Miocene extensional tectonics and fluid flow across the Northern Snake Range detachment system, Nevada. Tectonics v. 30, doi: 10.1029/2010TC002797.

Gébelin, A., Mulch, A., Teyssier, C., Chamberlin, C. Heizler, M., 2012, Coupled basin-detachment systems as paleoaltimetry archives of the western North American Cordillera. Earth Plan. Sci. Let. v. 335, p. 36-47.

Gébelin, A., Mulch, A., Teyssier, C., Jessup, M., Law, R., and Brunel, M., 2013, The Miocene elevation of Mount Everest: Geology, v. 41, p. 799–802.

Gébelin, A., Teyssier, C., Heizler, M., Mulch, A., 2015. Meteoric water circulation in a rolling-hinge detachment system (Northern Snake Range core complex, Nevada). *Geol. Soc. America Bulletin*, 127, 149-161. doi: 10.1130/B31063.1.

Gébelin, A., Jessup, M.J., Teyssier, C., Cosca, M.A., Law, R.D., Brunel, M., and Mulch, A., 2017, Infiltration of meteoric water in the South Tibetan Detachment (Mount Everest, Himalaya): When and why?: Tectonics, v. 6, no. 8, p. 381–24, doi: 10.1002/2016TC004399.

Geiser, P., and Engelder, T., 1983, The distribution of layer parallel shortening fabrics in the Appalachian foreland of New York and ‘Pennsylvania: Evidence for two non-coaxial phases of the Alleghanian orogeny: Geological Society of America.

Ghisetti, F., Kirschner, D.L., Vezzani, L., and Agosta, F., 2001, Stable isotope evidence for contrasting paleofluid circulation in thrust faults and normal faults of the central Apennines, Italy: Journal of Geophysical Research, v. 106, no. B5, p. 8811–8825, doi: 10.1029/2000JB900377/asset/jgrb12610.pdf.

Glasmann, J., Lundergard, P., Clark, R., Penny, B., Collins, I., 1989. Geochemical evidence for the history of diagenesis and fluid migration: Brent Sandstone, Heather Field, North Sea. Clay Minerals v. 24, p. 255-284.

Gottardi, R., Teyssier, C., Mulch, A., Vennemann, T., Wells, M., 2011. Preservation of an extreme transient geotherm in the Raft River detachment shear zone. Geology 39, p. 759-762.

Graham, C., Viglino, J., Harmon, R., 1987. Experimental study of hydrogen isotope exchange between aluminous chlorite and water and of hydrogen diffusion in chlorite. American Mineralogist 72, p. 566-579.

Gray, M.B., and Stamatakos, J., 1998, New model for evolution of fold and thrust belt curvature based on integrated structural and paleomagnetic results from the Pennsylvania salient: Geology, v. 25, no. 12, p. 1067–1070.

Grim, R.E., 1962, Applied clay mineralogy: McGraw Hill, New York, 422 p.

Gwinn, V.E., 1964, Thin-skinned tectonics in the Plateau and northwestern Valley and Ridge provinces of the central Appalachians: Geological Society of America Bulletin, v. 75, p. 863–900.

Haines, S., and van der Pluijm, B., 2008, Clay quantification and Ar-Ar dating of synthetic and natural gouge: Application to the Miocene Sierra Mazatán detachment fault, Sonora, Mexico: Journal of Structural Geology, v. 30, p. 525–538.

Haines, S. and van der Pluijm, B., 2010, Dating the detachment fault system of the Ruby Mountains, Nevada: significance for the kinematics of low-angle normal faults. Tectonics v. 29, doi:10.1029/2009TC002552.

Haines, S., van der Pluijm, B., 2012, Patterns of mineral transformations in clay gouge, with examples from low-angle normal fault rocks in the western USA: J. Structural. Geol. v. 43, p. 2 – 32.

Haines, S., Marone, C., Saffer, D., 2014. Frictional properties of low-angle normal fault gouges and implications for low-angle normal fault slip. Earth and Planetary Science Letters 408, p. 57-65.

Haines, S., Lynch, E., Mulch, A., Valley, J.W., and van der Pluijm, B.A., 2016, Meteoric fluid infiltration in crustal-scale normal fault systems as indicated by δ18O and δ2H geochemistry and 40Ar/39Ar dating of neoformed clays in brittle fault rocks: Lithosphere, v. 8, no. 6, p. L483.1–14, doi: 10.1130/L483.1.

Hall, C.M., 2014, Direct measurement of recoil effects on 40Ar/39Ar standards: Geological Society, London, Special Publications, v. 378, no. 1, p. 53–62, doi: 10.1144/SP378.7.

Haney, M.M., Snieder, R., Sheiman, J., and Losh, S., 2005, Geophysics: A moving fluid pulse in a fault zone: Nature, v. 437, no. 7055, p. 46, doi: 10.1038/437046a.

Hardebol, N.J., Callot, J.P., Bertotti, G., and Faure, J.L., 2009, Burial and temperature evolution in thrust belt systems: Sedimentary and thrust sheet loading in the SE Canadian Cordillera: Tectonics, v. 28, no. 3, p. n/a–n/a, doi: 10.1029/2008TC002335.

Harris, A.G., Stamm, N.R., Weary, D.J., Repetski, J.E., Stamm, R.G., and Parker, R.A., 1994, Conodont color alteration index (CAI) map and conodont-based age determinations for the Winchester 30" x 60" quadrangle and adjacent areas Virginia, West Virginia, and Maryland, p. 1–40.

Hatcher Jr, R.D., Thomas, W.A., Geiser, P.A., Snoke, A.W., Mosher, S. and Wiltschko, D.V., 1989, Alleghanian orogen: *in* Hatcher Jr, R.D., Thomas, W.A. and Viele, G.E., eds., The Appalachian-Ouachita Orogen in the United States, The Geology of North America Volume F-2*:* Geological Society of America, Boulder, Colorado, p. 233□318.

Hatcher, R.D., Lemiszki, P.J., and Whisner, J.B., 2007, Character of rigid boundaries and internal deformation of the southern Appalachian foreland fold-thrust belt, *in* Special Paper 433: Whence the Mountains? Inquiries into the Evolution of Orogenic Systems: A Volume in Honor of Raymond A. Price, Geological Society of America, p. 243–276.

Hatcher, R.D., Jr., 2010, The Appalachian orogen: A brief summary, *in* Tollo, R.P., Bartholomew, M.J., Hibbard, J.P., and Karabinos, P.M., eds., From Rodinia to Pangea: The Lithotectonic Record of the Appalachian Region: Geological Society of America Memoir, no. 206, p. 1–19, doi: 10.1130/2010.1206(01).

Hayes, M.J., and Boles, J.R., 1993, Evidence for meteoric recharge in the San Joaquin basin, California provided by isotope and trace element chemistry of calcite: Marine and Petroleum Geology, v. 10, no. 2, p. 135–144, doi: 10.1016/0264-8172(93)90018-N.

Hearn, P.P., Sutter, J.F., and Belkin, H.E., 1987, Evidence for Late-Paleozoic brine migration in Cambrian carbonate rocks of the central and southern Appalachians: Implications for Mississippi Valley-type sulfide mineralization: Geochimica et Cosmochimica Acta, v. 51, no. 5, p. 1323–1334, doi: 10.1016/0016-7037(87)90222-5.

Hetzel, R., Zwingmann, H., Mulch, A., Gessner, K., Akal, C., Hampel, A., Güngör, T., Petschick, R. Mikes, T., Wedin, F., 2013. K-Ar ages and hydrogen isotope data from detachment fault systems in the Menderes Massif (Turkey): Implications for the timing of brittle deformation and fluid flow. Tectonics, 32, 1-13. doi:10.1002/tect.20031

Hibbard, J.P., van Staal, C.R., and Rankin, D.W., 2010, Comparative analysis of the geological evolution of the northern and southern Appalachian orogen: Late Ordovician–Permian, in Tollo, R.P., Bartholomew, M.J., Hibbard, J.P., and Karabinos, P.M., eds., From Rodinia to Pangea: The Lithotectonic Record of the Appalachian Region: Geological Society of America Memoir 206, p. 51–69, doi: 10.1130/2010.1206(03).

Hickman, S.H., Zoback, M.D., and Ellsworth, W., 2004, Introduction to special section: Preparing for the San Andreas Fault Observatory at Depth: Geophysical Research Letters, v. 31, no. 12, doi: 10.1029/2004GL020688.

Hillier, S., 2000, Accurate quantitative analysis of clay and other minerals in sandstones by XRD: Comparison of a Rietveld and a reference intensity ratio (RIR) method and the importance of sample preparation: Clay Minerals, v. 35, no. 1, p. 291–302, doi: 10.1180/000985500546666.

Hitchon, B., and Friedman, I., 1969, Geochemistry and origin of formation waters in the western Canada sedimentary basin—I. Stable isotopes of hydrogen and oxygen: Geochimica et Cosmochimica Acta, v. 33, no. 11, p. 1321–1349, doi: 10.1016/0016-7037(69)90178-1.

Hnat, J.S., 2009, Kinematic and temporal evolution of the Southern Appalachian foreland fold-thrust belt: Constraints from structural, magnetic and radiometric analyses, Ph.D. dissertation, 286 pages. University of Michigan, Ann Arbor, MI.

Hnat, J.S., and van der Pluijm, B.A., 2014, Fault gouge dating in the Southern Appalachians, USA: Geological Society of America Bulletin, v. 126, no. 5-6, p. 639–651, doi: 10.1130/B30905.1.

Hodges, K., McKenna, L., Stock, J., Knapp, J., Page, L., Sternlof, K., Silverberg, D., Wust, G., Walker, J., 1989. Evolution of extensional basins and Basin and Range topography west of Death Valley, California. Tectonics 8, pp. 453-467.

Hoke, G.D., Garzione, C.N., Araneo, D.C., Latorre, C., Strecker, M.R., and Williams, K.J., 2009, The stable isotopic altimeter: Do Quaternary pedogenic carbonats predict modern elevations?: Geology, v. 37, no., 11., p.1015-1018, doi: 10.1130/G30308A.1.

Hoke, G.D., Aranibar, J.N., Viale, M., Araneo, D.C., and Llano, C., 2013, Seasonal moisture sources and the isotopic composition of precipitation, rivers, and carbonates across the Andes at 32.5-35.5°S: Geochemistry, Geophysics, Geosystems, v.14, no. 4, doi: 10.1002/ggge.20045.

Hoke, G.D, Giambiagi, L.B, Garzione, C.N, Mahoney, J.B and Strecker, M.R., 2014, Neogene paleoelevation of intermontane basins in a narrow compressional mountain range, southern Central Andes of Argentina: Earth and Planetary Science Letters, v. 406, p. 153–164, doi: 10.1016/j.epsl.2014.08.032.

Holdsworth, R.E., van Diggelen, E.W.E., Spiers, C.J., de Bresser, J.H.P., Walker, R.J., and Bowen, L., 2011, Fault rocks from the SAFOD core samples: Implications for weakening at shallow depths along the San Andreas Fault, California: Journal of Structural Geology, v. 33, no. 2, p. 132–144, doi: 10.1016/j.jsg.2010.11.010.

Holland, M., Urai, U., van der Zee, W., Stanjek, H., Konstanty, J., 2006. Fault gouge evolution in highly overconsolidated claystones.. J. Structural Geology 28, p. 323-332.

Holser, W., 1979. Trace elements and isotopes in evaporates. In: Marine Minerals (ed. R. Burns). Rev. in Min. v. 6, 295-346.

Horton, T., Chamberlin, C.P., 2006. Stable Isotopic evidence for Neogene surface downdrop in the central Basin and Range province. Geol. Soc. Amer. Bull 118, p. 475-490.

Hubbert, M.K., and Rubey, W.W., 1959, Role of fluid pressure in mechanics of overthrust faulting I. Mechanics of fluid-filled porous solids and it's application to overthrust faulting: Geological Society of America Bulletin, v. 70, no. 2, p. 115–166, doi: 10.1130/0016-7606(1959)70[115:ROFPIM]2.0.CO;2.

Hunziker, J.C., 1986, The evolution of illite to muscovite: An example of the behaviour of isotopes in low-grade metamorphic terrains: Chemical Geology, v. 57, no. 1, p. 31–40, doi: 10.1016/0009-2541(86)90092-6.

Hüpers, A., Torres, M.E., Owari, S., McNeill, L.C., Dugan, B., Henstock, T.J., Milliken, K.L., Petronotis, K.E., Backman, J., Bourlange, S., Chemale, F., Chen, W., Colson, T.A., Frederik, M.C.G., et al., 2017, Release of mineral-bound water prior to subduction tied to shallow seismogenic slip off Sumatra: Science, v. 356, no. 6340, p. 841–844, doi: 10.1126/science.aal3429.

IAEA/WMO, 2016, Global Network of Isotopes in Precipitation, The GNIP Database, International Atomic Energy Agency, Vienna: http://www.iaea.org/water.

Isik, V., Tonguc Uysal, I., Caglayan, A., Seyitoglu, G., 2014. The evolution of intraplate fault systems in central Turkey: Structural evidence and Ar-Ar and Rb-Sr age constraints for the Savcili Fault Zone. Tectonics 33, pp. 1875-1899. doi: 10.1002/2014TC003565

Jamieson, R.A., and Beaumont, C., 1988, Orogeny and metamorphism: A model for deformation and pressure-temperature-time paths with applications to the Central and Southern Appalachians: Tectonics, v. 7, no. 3, p. 417–445.

Janssen, C., Wirth, R., Reinicke, A., Rybacki, E., Naumann, R., Wenk, H.-R., and Dresen, G., 2011, Nanoscale porosity in SAFOD core samples (San Andreas Fault): Earth and Planetary Science Letters, v. 301, no. 1-2, p. 179–189, doi: 10.1016/j.epsl.2010.10.040.

Jiskra, M., Wiederhold, J.G., Bourdon, B., and Kretzschmar, R., 2012, Solution Speciation Controls Mercury Isotope Fractionation of Hg(II) Sorption to Goethite: Environmental Science & Technology, v. 46, no. 12, p. 6654–6662, doi: 10.1021/es3008112.

Jordan, T.E., Allmendinger, R.W., and Damanti, J.F., 1993, Chronology of motion in a complete thrust belt: the Precordillera, 30-31 S, Andes Mountains: The Journal of Geology, v. 101, no. 2, p. 135–156.

Jordan, T.E., Schlunegger, F., and Cardozo, N., 2001, Unsteady and spatially variable evolution of the Neogene Andean Bermejo foreland basin, Argentina: Journal of South American Earth Sciences, v. 14, p. 775–798.

Kalkreuth, W., and McMechan, M.E., 1984, Regional pattern of thermal maturation as determined from coal-rank studies, Rocky Mountain Foothills and Front Ranges north of Grande Cache, Alberta - implications for petroleum exploration: Bulletin of Canadian Petroleum Geology, v. 32, no. 3, p. 249–271.

Kay, S.M., Ramos, V.A., Mpodozis, C., and Sruoga, P., 1989, Late Paleozoic to Jurassic silicic magmatism at the Gondwana margin: Analogy to the Middle Proterozoic in North America: Geology, v. 17., no. 4, p. 324-328.

Kendrick, M.A., and Burnard, P., 2012, Noble gases and halogens in fluid inclusions: A journey through the Earth's crust, in Burnard, P. ed., The Noble Gases as Geochemical Tracers, Springer Berlin Heidelberg, Berlin, Heidelberg, p. 319–369.

Kennedy, B.M., Kharaka, Y.K., Evans, W.C., Ellwood, A., DePaolo, D.J., Thordsen, J., Ambats, G., and Mariner, R.H., 1997, Mantle fluids in the San Andreas Fault System, California: Science, v. 2782, n. 5341, p.1278-1281, doi: 10.1126/science.278.5341.1278.

Kent, D.V., 1988, Further paleomagnetic evidence for oroclinal rotation in the central folded Appalachians from the Bloomsburg and the Mauch Chunk Formations: Tectonics, v. 7, no. 4, p. 749–759, doi: 10.1029/TC007i004p00749.

Kerrich, R., 1986, Fluid Infiltration Into Fault Zones: Chemical, Isotopic, and Mechanical Effects: Pure and Applied Geophysics, v. 124, no. 1-2, p. 225–268, doi: 10.1007/BF00875727.

Kerrich, R., 1988. Detachment zones of Cordilleran metamorphic core complexes: thermal, fluid and metasomatic regimes. Geologische Rundschau 77/1, p. 157-182.

Kerrich, R., Hyndman, D., 1986. Thermal and fluid regimes in the Bitterroot lobe-Sapphire block zone detachment zone, Montana: Evidence from $\delta^{18}O/\delta^{16}O$ relations. GSA Bulletin, v. 97, p. 147-156.

Kerrich, R., Rehrig, W., 1987. Fluid motion associated with Tertiary mylonitization and detachment faulting: $^{18}O/^{16}O$ evidence from the Picacho metamorphic core complex, Arizona. Geology 15, p. 58-62.

Kerrich, R., La Tour, T., Willmore, L., 1984. Fluid participation in deep fault zones: Evidence from geological, geochemical and 18O/16O relations. J. Geophysical Research B 89, p. 4331-4343.

Kesler, S.E. and van der Pluijm, B.A., 1990, Timing of Mississippi Valley-type mineralization; relation to Appalachian orogenic events: Geology, v. 18, no. 11, p. 1115- 1118, doi: 10.1130/0091-7613(1990)018<1115:TOMVTM>2.3.CO;2.

Kharaka, Y.K., Thordsen, J.J., Evans, W.C., and Kennedy, B.M., 1999, Geochemistry and hydromechanical interactions of fluids associated with the San Andreas fault system, California: Geophysical Monograph, v. 113, p. 129–148, doi: 10.1029/GM113p0129.

Kirby, S.H., Wang, K., and Brocher, T.M., 2014, A large mantle water source for the northern San Andreas fault system: a ghost of subduction past: Earth, Planets and Space, v. 66, no. 1, p. 67–18, doi: 10.1186/1880-5981-66-67.

Kirschner, D.L., and Kennedy, L.A., 2001, Limited syntectonic fluid flow in carbonate-hosted thrust faults of the Front Ranges, Canadian Rockies, inferred from stable isotope data and structures: Journal of Geophysical Research, v. 106, no. B5, p. 8827-8840, doi: 10.1029/2000JB900414.

Kirschner, D.L., and Sharp, Z.A., 1997, Oxygen isotope analyses of fine-grained minerals and rocks using the laser-extraction technique: Chemical Geology, v. 137, no. 1-2, p. 109-115, doi: 10.1016/S0009-2541(96)00123-4.

Kleeberg, R., 2009, State-of-the-art and trends in quantitative phase analysis of geological and raw materials: Zeitschrift für Kristallographie Supplements, v. 30, p. 47–52, doi: 10.1524/zksu.2009.0007.

Knott, J., Sarna-Wojiciki, A., Machette, Klinger, R., 2005, Upper Neogene stratigraphy and tectonics of Death Valley – a review. Earth-Science Reviews 73, p. 245-270, doi: 10.1016/j.earscirev.2005.07.004

Koch, P.L., Zachos, J.C., and Dettman, D.L., 1995, Stable-Isotope Stratigraphy and Paleoclimatology of the Paleogene Bighorn Basin (Wyoming, Usa): Palaeogeography Palaeoclimatology Palaeoecology, v. 115, no. 1-4, p. 61–89, doi: 10.1016/0031-0182(94)00107-J.

Koons, P.O., and Craw, D., 1991, Evolution of Fluid Driving Forces and Composition Within Collisional Orogens: Geophysical Research Letters, v. 18, no. 5, p. 935–938, doi: 10.1029/91GL00910.

Koons, P.O., Craw, D., Cox, S.C., Upton, P., Templeton, A.S., and Chamberlain, C.P., 1998, Fluid flow during active oblique convergence: A Southern Alps model from mechanical and geochemical observations: Geology, v. 26, no. 2, p. 159–162, doi: 10.1130/0091-7613(1998)026<0159:FFDAOC>2.3.CO;2.

Lacroix, B., Charpintier, D., Buatier, M., Vennemann, T., Labaume, P., Adatte, T., Trave, A., Dubois, M., 2012. Formation of chlorite during thrust fault reactivation. Record of fluid origin and P-T conditions in the Monte Perdido thrust fault (southern Pyrenees). Contrib. Min. Petrol. 163, p. 1083-1102.

Lacroix, B., Travé, A., Buatier, M.D., Labaume, P., Vennemann, T.W., and Dubois, M., 2014, Syntectonic fluid-flow along thrust faults: Example of the South-Pyrenean fold-and-thrust belt: Marine and Petroleum Geology, v. 49, no. C, p. 84–98, doi: 10.1016/j.marpetgeo.2013.09.005.

Lawrence, J.R., and Taylor, H.P., Jr, 1971, Deuterium and oxygen-18 correlation: Clay minerals and hydroxides in Quaternary soils compared to meteoric waters: Geochimica et Cosmochimica Acta, v. 35, no. 10, p. 993–1003, doi: 10.1016/0016-7037(71)90017-2.

Leach, D.L., Taylo, R.D., Fey, D.L., Diehl, S.F and Saltus, R.W., 2010, A Deposit Model for Mississippi Valley-Type Lead-Zinc Ores, Chapter A *of* Mineral deposit models for resource assessment: USGS Scientific Investigations Report 2010-5070-A, 52 p.

Lechler, A.R., and Niemi, N.A., 2011, Controls on the spatial variability of modern meteoric $\delta^{18}O$: Empirical constraints from the western U.S. and East Asia and implications for stable isotope studies: American Journal of Science, v. 311, p. 664–700, doi: 10.2475/08.2011.02.

Lechler, A.R., and Niemi, N.A., 2012, The influence of snow sublimation on the isotopic composition of spring and surface waters in the southwestern United States: Implications for stable isotope–based paleoaltimetry and hydrologic studies: Geological Society of America Bulletin, v. 124, p. 318–334, doi: 10 .1130 /B30467 .1.

Leclere, H., Lacroix, B., Fabbri, O., 2014. Fault mechanics at the base of the continental seismogenic zone: Insights from geomechanical and mechanical analyses of a crustal-scale transpressional fault from the Argentera crystalline massif, French-Italian Alps. Journal of Structural Geology 66, p. 115-128.

Lee, D., Friedman, I., and Gleason, J., 1984, Modification of dD values in eastern Nevada granitoid rocks spatially related to thrust faults: Contributions to Mineralogy and Petrology, v. 88, p. 288–298.

Lefticariu, L. Klaue, B., Blum, J.D., and Buseck, P.R., 2011, Mercury isotopic evidence for multiple mercury sources in coal from the Illinois Basin: Environmental Science and Technology, v. 45, p. 1724–1729.

Levina, M., Horton, B.K., Fuentes, F., and Stockli, D.F., 2014, Cenozoic sedimentation and exhumation of the foreland basin system preserved in the Precordillera thrust belt (31-32°S), southern central Andes, Argentina: Tectonics, v. 33, no. 9, p. 1659-1680, doi: 10.1002/2013TC003424.

Liu, J., Feng, X., Yin, R., Zhu, W., and Li, Z., 2011, Mercury distributions and mercury isotope signatures in sediments of Dongjiang, the Pearl River Delta, China: Chemical Geology, v. 287, no. 1-2, p. 81–89, doi: 10.1016/j.chemgeo.2011.06.001.

Longstaffe, F.J., and Ayalon, A., 1990, Hydrogen-isotope geochemistry of diagenetic clay minerals from Cretaceous sandstones, Alberta, Canada: evidence for exchange: Applied Geochemistry, v. 5, no. 5, p. 657–668, doi: 10.1016/0883-2927(90)90063-B.

Losh, S., 1997. Stable isotope and modeling studies of fluid-rock interaction associated with the Snake Range and Mormon Peak detachment faults, Nevada. Geol. Soc. Amer. Bull. 109, p. 300-323.

Losh, S., Purvance, D., Sherlock, Jowett, E., 2005, Geologic and geochemical study of the Picacho gold mine, California: gold in a low-angle normal fault environment. Mineralium Deposita v. 40, p. 137-155.

Lu, G., Marshak, S., and Kent, D.V., 1990, Characteristics of magnetic carriers responsible for Late Paleozoic remagnetization in carbonate strata of the mid-continent, U.S.A.: Earth and Planetary Science Letters, v. 99, no. 4, p. 351–361, doi: 10.1016/0012-821X(90)90139-O.

Luetkemeyer, P.B., Kirschner, D.L., Huntington, K.W., Chester, J.S., Chester, F.M., and Evans, J.P., 2016, Constraints on paleofluid sources using the clumped-isotope thermometry of carbonate veins from the SAFOD (San Andreas Fault Observatory at Depth) borehole: Tectonophysics, v. 690, Part A, p. 174–189, doi: 10.1016/j.tecto.2016.05.024.

Lynch, E.A., and van der Pluijm, B.A., 2016, Meteoric fluid infiltration in the Argentine Precordillera fold-and-thrust belt: Evidence from H isotopic studies of neoformed clay minerals: Lithosphere, v. 9, no. 1, p. L568.1–12, doi: 10.1130/L568.1.

Lynch et al., *in review*, Surface fluids in the evolving Sevier fold-thrust belt of ID-WY indicated by hydrogen isotopes in dated, authigenic clay minerals: Earth and Planetary Science Letters.

Lyubetskaya, T., and Ague, J., 2009, Modeling the magnitudes and directions of regional metamorphic fluid flow in collisional orogens: Journal of Petrology, v. 50, p. 1505-1531.

Machel, H.G., Cavell, P.A., and Patey, K.S., 1996, Isotopic evidence for carbonate cementation and recrystallization, and for tectonic expulsion of fluids into the

Western Canada Sedimentary Basin: Geological Society of America Bulletin, v. 108, no. 9, p. 1108–1119, doi: 10.1130/0016-7606(1996)108<1108:IEFCCA>2.3.CO;2.

Machel, H.G., and Cavell, P.A., 1999, Low-flux, tectonically-induced squeegee fluid flow ("hot flash") into the Rocky Mountain Foreland Basin: Bulletin of Canadian Petroleum Geology, v. 47, no. 4, p. 510–533.

Mackay, P.A., 2015, The role of fluid pressure in contractional systems: examples from the Southern Canadian Rocky Mountains: Geological Society, London, Special Publications, v. 421, no. 1, p. 69–82, doi: 10.1144/SP421.5.

Mahon, K., 1996, The new "York" regression: Application of an improved statistical method to geochemistry: International Geology Review, v. 38, p. 293–303, doi: 10.1080/00206819709465336.

Mancktelow, N., Zwingmann, H., Campani, M., Fügenschuh, B., Mulch, A. 2015. Timing and conditions of brittle faulting on the Silltal-Brenner Fault Zone, Eastern Alps (Austria). Swiss Journal of Geosciences, doi: 10.1007/s00015-015-0179-y

Markshak, S., and Wilkerson, M.S., 2004, Fold-Thrust Belts *in* B.A. van der Pluijm and S. Marshak, eds.: Earth Structure, 2nd ed., W.W. Norton and Co, p. 444–474.

McCaig, A., 1997. The geochemistry of volatile fluid flow in shear zones, *in* Holness, M., et al., eds., Deformation-enhanced fluid transport in the Earth's crust and mantle (The Mineralogical Society Series 8): London, chapman & Hall, p. 227-266.

McCaig, A., Wayne, D., Marshall, J., Banks, D., Henderson, D., 1995. Isotopic and fluid inclusion studies of fluid movement along the Gavernie Thrust, Central Pyrenees: Reaction fronts in carbonate mylonites. American Journal of Science, v. 295, p. 309-343.

McFadden, R.R., Mulch, A., Teyssier, C., and Heizler, M., 2015, Eocene extension and meteoric fluid flow in the Wildhorse detachment, Pioneer metamorphic core complex, Idaho: Lithosphere, v. 7, no. 4, p. 355–366, doi: 10.1130/L429.1.

McKenna, J.R., and Blackwell, D.D., 2004, Numerical modeling of transient Basin and Range extensional geothermal systems: Geothermics, v. 33, p. 457–476, doi: 10.1016 /j.geothermics.2003.10.001.

Menzies, C., Teagle, D., Craw, D., Cox, S., Boyce, A., Barrie, C., Roberts, S., 2014. Incursion of meteoric waters into the ductile regime in an active orogen. Earth and Planetary Science Letters 399, p. 1-13.

Menzies, C.D., Teagle, D.A.H., Niedermann, S., Cox, S.C., Craw, D., Zimmer, M., Cooper, M.J., and Erzinger, J., 2016, The fluid budget of a continental plate boundary fault: Quantification from the Alpine Fault, New Zealand: Earth and Planetary Science Letters, v. 445, no. C, p. 125–135, doi: 10.1016/j.epsl.2016.03.046.

Micklethwaite, S., and Cox, S.F., 2004, Fault-segment rupture, aftershock-zone fluid flow, and mineralization: Geology, v. 32, no. 9, p. 813–4, doi: 10.1130/G20559.1.

Micklethwaite, S., Ford, A., Witt, W., and Sheldon, H.A., 2014, The where and how of faults, fluids and permeability - insights from fault stepovers, scaling properties and gold mineralisation: Geofluids, v. 15, no. 1-2, p. 240–251, doi: 10.1111/gfl.12102.

Milici, R.C., 1975, Structural Patterns in the Southern Appalachians: Evidence for a Gravity Slide Mechanism for Alleghanian Deformation: Geological Society of America Bulletin, v. 86, p. 1316–1320.

Miller, J.D., and Kent, D.V., 1988, Regional trends in the timing of Alleghanian remagnetization in the Appalachians: Geology, v. 16, p. 588–591.

Mitra, G., and Yonkee, W.A., 1985, Spaced cleavage and its relationship to folds and thrusts in the Idaho-Utah- Wyoming thrust belt of the Rocky Mountain Cordilleras: Journal of Structural Geology, v. 7, p. 361–373, doi: 10.1016/0191-8141(85)90041-0.

Mitra, S., 1987, Regional variations in deformation mechanisms and structural styles in the central Appalachian orogenic belt: Geological Society of America Bulletin, v. 98, p. 569–590.

Mix, H.T., and Chamberlain, C.P., 2014, Stable isotope records of hydrologic change and paleotemperature from smectite in Cenozoic western North America: Geochimica et Cosmochimica Acta, v. 141, no. C, p. 532–546, doi: 10.1016/j.gca.2014.07.008.

Monteiro, P.J.M., Rycroft, C.H., and Barenblatt, G.I., 2012, A mathematical model of fluid and gas flow in nanoporous media: Proceedings of the National Academy of Sciences of the United States of America, v. 109, no. 50, p. 20309–20313, doi: 10.1073/pnas.1219009109.

Moore, D.M., and Reynolds Jr., R.C., 1997, X-Ray Diffraction and the Identification and Analysis of Clay Minerals, Oxford University Press, New York.

Morad, S., Worden, R.H., and Ketzer, J.M., 2003, Oxygen and hydrogen isotopic composition of diagenetic clay minerals in sandstones: a review of the data and controls: International Association of Sedimentologists Special Publication, v. 34, p. 63-91.

Moretti, I., Labaume, P., Sheppard, S.M.F., and Boulègue, J., 2002, Compartmentalisation of fluid migration pathways in the sub-Andean Zone, Bolivia: Tectonophysics, v. 348, p. 5–24.

Morrison, J., 1994. Meteoric water-rock interaction in the lower plate of the Whipple Mountain metamorphic core complex, California. J. Met. Geol. v. 12, p. 827-840.

Morrison, J., Anderson, J. L., 1998. Footwall refrigeration along a detachment fault: Implications for the thermal evolution of core complexes. Science 279, p. 63-66.

Morrow, C., Lockner, D.A., Moore, D.E., and Hickman, S.H., 2014, Deep permeability of the San Andreas Fault from San Andreas Fault Observatory at Depth (SAFOD) core samples: Journal of Structural Geology, v. 64, no. C, p. 99–114, doi: 10.1016/j.jsg.2013.09.009.

Muir-Wood, R., and King, G.C.P., 1993, Hydrological Signatures of Earthquake Strain: Journal of Geophysical Research, v. 98, no. B12, p. 22,035–22,068, doi: 10.1029/93JB02219.

Mulch, A., Teyssier, C., Cosca, M.A., Vanderhaeghe, O., and Vennemann, T.W., 2004. Reconstructing paleoelevation in eroded orogens: Geology, v. 32, p. 525-529.

Mulch, A., and Chamberlain, C.P., 2007, Stable Isotope Paleoaltimetry in Orogenic Belts - The Silicate Record in Surface and Crustal Geological Archives: Reviews in Mineralogy and Geochemistry, v. 66, no. 1, p. 89–118, doi: 10.2138/rmg.2007.66.4.

Mulch, A., Teyssier, C., Cosca, M., and Chamberlin, C.P., 2007, Stable isotope paleoaltimetry of Eocene core complexes in the North American Cordillera: Tectonics, v. 26, TC4001, doi: 10.1029/2006TC001995.

Mulch, A., Uba, C.E., Strecker, M.R., Schoenberg, R., and Chamberlain, C.P., 2010, Late Miocene climate variability and surface elevation in the central Andes: Earth and Planetary Science Letters, v. 290, no. 1-2, p. 173–182, doi: 10.1016/j.epsl.2009.12.019.

Nesbitt, B.E., and Muehlenbachs, K., 1989, Geology, Geochemistry, and Genesis of Mesothermal Lode Gold Deposits of the Canadian Cordillera: Evidence for Ore Formation from Evolved Meteoric Water, in R. R. Keays, W. Ramsay, & D. I. Groves, Eds.: Economic Geology Monograph Series, v. 6, p. 553–563, doi: doi.org/10.5382/Mono.06.42.

Nesbitt, B.E., and Muehlenbachs, K., 1991, Stable isotopic constraints on the nature of the syntectonic fluid regime of the Canadian Cordillera: Geophysical Research Letters, v. 18, no. 5, p. 963-066, doi: 10.1029/91GL00914.

Nesbitt, B.E., and Muehlenbachs, K., 1995. Geochemical studies of the origins and effects of synorogenic crustal fluids in the southern Omineca Belt of British Colombia, Canada. Geol. Soc. Amer. Bull. 107, p. 1033-1050.

Norton, I., 2011. Two-stage formation of Death Valley. Geosphere, v. 7, p. 171-182.

Oliver, J., 1986, Fluids expelled tectonically from orogenic belts: Their role in hydrocarbon migration and other geologic phenomena: Geology, v. 14, p. 99–102, doi: 10.1130/0091-7613(1986)14<99:FETFOB>2.0.CO;2.

O'Neil, J., Taylor, H., (1969). Oxygen isotope equilibrium between muscovite and water. J. Geophysical Research B 74, p. 6012 – 6022.

Ong, P.F., van der Pluijm, B.A., and Van der Voo, R., 2007, Early rotation and late folding in the Pennsylvania salient (U.S. Appalachians): Evidence from calcite-twinning analysis of Paleozoic carbonates: Geological Society of America Bulletin, v. 119, no. 7-8, p. 796–804, doi: 10.1130/B26013.1.

Osadetz, K. G., B. P. Kohn, S. Feinstein, and R. A. Price, 2004, Foreland belt thermal history using apatite fission-track thermochronology: Implications for Lewis thrust and Flathead fault in the southern Canadian Cordilleran petroleum province, in R. Swennen, F. Roure, and J. W. Granath, eds., Deformation, fluid flow, and reservoir appraisal in foreland fold and thrust belts: AAPG Hedberg Series, no. 1, p. 21–48, doi: 10.1306/1025684H13111.

Painter, C.S., Carrapa, B., DeCelles, P.G., Gehrels, G.E., Thomson, S.N., 2014. Exhumation of the North American Cordillera revealed by multi-dating of Upper Jurassic–Upper Cretaceous foreland basin deposits. Geological Society of America Bulletin, v. 126, no.10/11, p. 1439–1464, doi: 10.1130/B30999.1.

Pană, D.I., and Elgr, R., 2013, Geological Map of the Alberta Rocky Mountains and Foothills (NTS 82G, 82H, 82J, 82O, 82N, 83B, 83C, 83D, 83F, 83E, and 83L). Energy Resources Conservation Board (ERCB)/Alberta Geological Survey (AGS) Map 560, scale 1:500 000. http:// www .ags .gov .ab .ca /publications /MAP /PDF /MAP 560 .PDF.

Pană, D.I., and van der Pluijm, B.A., 2015, Orogenic pulses in the Alberta Rocky Mountains: Radiometric dating of major faults and comparison with the regional tectono-stratigraphic record: Geological Society of America Bulletin, v. 127, no. 3-4, p. 480–502, doi: 10.1130/B31069.1.

Parés, J.M., Schleicher, A.M., VanderPluijm, B.A., and Hickman, S.H., 2008, Paleomagnetic reorientation of San Andreas Fault Observatory at Depth (SAFOD) core: Geophysical Research Letters, v. 35, no. 2, p. L02306–6, doi: 10.1029/2007GL030921.

Peacock, S.M., 1989, Numerical constraints on rates of metamorphism, fluid production, and fluid flux during regional metamorphism: Geological Society of America Bulletin, v. 101, no. 4, p. 476–485, doi: 10.1130/0016-7606(1989)101<0476:NCOROM>2.3.CO.

Perry, W.J., Jr., 1978, Sequential Deformation in the Central Appalachians: American Journal of Science, v. 278, p. 518-542.

Person, M., Mulch, A., Teyssier, C., Yongli, G., 2007, Isotope transport and exchange within metamorphic core complexes: American Journal of Science, v. 307, p. 555-589.

Peters, M., Wickham, S., 1995. On the causes of ^{18}O-depletion and ^{18}O/^{16}O homogenization during regional metamorphism; the East Humboldt Range core complex, Nevada. Contrib. Min. Petrol., v. 119, p. 68-82.

Peters, N.A., Huntington, K.W., and Hoke, G.D., 2013, Hot or not? Impact of seasonally variable soil carbonate formation on paleotemperature and O-isotope records from clumped isotope thermometry: Earth and Planetary Science Letters, v. 361, no. C, p. 208–218, doi: 10.1016/j.epsl.2012.10.024.

Pevear, D.R., 1999, Illite and hydrocarbon exploration: Proceedings of the National Academy of Sciences of the United States of America, v. 96, no. 7, p. 3440–3446, doi: 10.1073/pnas.96.7.3440.

Pili, É., Kennedy, B.M., Conrad, M.E., and Gratier, J.P., 2011, Isotopic evidence for the infiltration of mantle and metamorphic CO_2–H_2O fluids from below in faulted rocks from the San Andreas Fault system: Chemical Geology, v. 281, no. 3-4, p. 242–252, doi: 10.1016/j.chemgeo.2010.12.011.

Phillips, J.C., 1982. Character and origin of cataclasite developed along the low-angle Whipple Detachment fault, Whipple Mountains, California. In: Mesozoic and Cenozoic tectonic evolution of the Colorado River Region, (Frost, E., Martin, D., eds.). p. 109 – 116. Cordilleran Publishers.

Photographic Atlas of the SAFOD Phase 3 Cores, 2011, Version 5: https://data.icdp-online.org/upload/projects/safod/phase3/Core_Photo_Atlas_v5.pdf.

Poage, M., and Chamberlin, C.P., 2002, Stable isotopic evidence for a Pre-Middle Miocene rainshadow in the western Basin and Range: Implications for the surface uplift of the Sierra Nevada. Tectonics v. 21, p. 16-1 – 16-10.

Pollyea, R.M., Van Dusen, E.W., and Fischer, M.P., 2015, Topographically driven fluid flow within orogenic wedges: Effects of taper angle and depth-dependent permeability: Geosphere, v. 11, no. 5, p. 1427–1437, doi: 10.1130/GES01120.1.

Poulsen, C.J., Pollard, D., Montañez, I.P., and Rowley, D., 2007, Late Paleozoic tropical climate response to Gondwanan deglaciation: Geology, v. 35, no. 9, p. 771–4, doi: 10.1130/G23841A.1.

Price, R.A., 1981, The Cordilleran foreland thrust and fold belt in the southern Canadian Rocky Mountains: Geological Society, London, Special Publications, v. 9, no. 1, p., 427-448, doi: 10.1144/gsl.sp.1981.009.01.39.

Ragona, D., Anselmi, G., Gonzalez, P., and Vujovich, G., 1995, Mapa Geológico de la Provincia de San Juan: Secretaría de Minaría Direccion National del Servicio Geológico, scale 1:500,000.

Rahl, J.M., Haines, S., and van der Pluijm, B.A., 2011, Links between orogenic wedge deformation and erosional exhumation: Evidence from illite age analysis of fault rock and detrital thermochronology of syn-tectonic conglomerates in the Spanish Pyrenees: Earth and Planetary Science Letters, v. 307, no. 1-2, p. 180–190, doi: 10.1016/j.epsl.2011.04.036.

Raimondo, T., Clark, C., Hand, M., Cliff, J., Anckiewicz, R., 2013. A simple mechanism for mid-crustal shear zones to record surface-derived fluid signatures. Geology 41, p. 711-714.

Ramos, V.A., 1988, The tectonics of the Central Andes; 30° to 33°S latitude: Geological Society of America Special Paper, no. 218, p. 31-54.

Ramos, V.A., Cristallini, E.O., and Pérez, D.J., 2002, The Pampean flat-slab of the Central Andes: Journal of South American Earth Sciences, v. 15, p. 59–79.

Repetski, J.E., Ryder, R.T., Weary, D.J., Harris, A.G., and Trippi, M.H., 2008, Thermal maturity patterns (conodont color alteration index and vitrinite reflectance) in Upper Ordovician and Devonian rocks of the Appalachian basin: a major revision of USGS Map I-917-E using new subsurface collections.

Rice, J.R., 1992, Fault Stress States, Pore Pressure Distributions, and the Weakness of the San Andreas Fault, *in* Evans, B and Wong, T eds., Fault Mechanics and Transport Properties in Rocks: A Festschrift in Honor of W.F. Brace, International Geophysics, v. 51, p. 475–503, doi: 10.1016/S0074-6142(08)62835-1.

Rich, J.L., 1921, Moving underground water as a primary cause of the migration and accumulation of oil and gas: Economic Geology, v. 16, no. 6, p. 347–371.

Rich, J.L., 1934. Mechanics of low-angle overthrust faulting as illustrated by Cumberland thrust bloc, Virginia, Kentucky and Tennessee: American Association of Petroleum Geologists Bulletin, v. 18, p. 1584-1596

Rietveld, H.M., 1969, A Profile Refinement Method for Nuclear and Magnetic Structures: Journal of Applied Crystallography, v. 2, no. 65, p. 65-71.

Roddy, M., Reynolds, S., Smith, B., Ruiz, J., 1988, K-metasomatism and detachment-related mineralization, Harcuvar Mountains, Arizona. Geol. Soc. Amer. Bull. v. 100, p. 1627-1639.

Roden, M.K., and Miller, D.S., 1989, Apatite fission-track thermochronology of the Pennsylvania Appalachian Basin: Geomorphology, v. 2, no. 1-3, p. 39–51, doi: 10.1016/0169-555X(89)90005-6.

Roden, M.K., 1991, Apatite fission-track thermochronology of the southern Appalachian basin: Maryland, West Virginia, and Virginia: The Journal of Geology, v. 99, no. 1, p. 41–53.

Rossi, M., and Rolland, Y., 2014, Stable isotope and Ar/Ar evidence of prolonged multiscale fluid flow during exhumation of orogenic crust: Example from the Mont Blanc and Aar Massifs (NW Alps): Tectonics, v. 33, no. 9, p. 1681–1709, doi: 10.1002/2013TC003438.

Royse, F., 1993, An overview of the geologic structure of the thrust belt in Wyoming, northern Utah, and eastern Idaho, in Snoke, A.W., Steidtmann, J. R., & Roberts, S.M., eds., Geology of Wyoming, Geological Survey of Wyoming Memoir 5, p. 272–311.

Rye, D.M., and Bradbury, H.J., 1988, Fluid-Flow in the Crust: an Example From a Pyrenean Thrust Ramp: American Journal of Science, v. 288, no. 3, p. 197–235.

Rygel, A.C., Anastasio, D.J., and Bebout, G.E., 2006, Syntectonic infiltration by meteoric waters along the Sevier thrust front, southwest Montana: Geofluids, v. 6, no. 4, p. 288–301, doi: 10.1111/j.1468-8123.2006.00146.x.

Sak, P.B., McQuarrie, N., Oliver, B.P., Lavdovsky, N., and Jackson, M.S., 2012, Unraveling the central Appalachian fold-thrust belt, Pennsylvania: The power of sequentially restored balanced cross sections for a blind fold-thrust belt: Geosphere, v. 8, no. 3, p. 685–702, doi: 10.1130/GES00676.1.

Sample, J., 2010, Stable isotope constraints on vein formation and fluid evolution along a recent thrust fault in the Cascadia Accretionary wedge. Earth Plan. Sci. Let. v. 293, p. 300-312.

Savin, S.M., and Hsieh, J., 1998, The hydrogen and oxygen isotope geochemistry of pedogenic clay minerals: principles and theoretical background: Geoderma, v. 82, no. 1-3, p. 227–253.

Savin, S.M., and Lee, M., 1988, Isotopic studies of phyllosilicates: Reviews in Mineralogy, v. 19, p. 189–219.

Schedl, A., McCabe, C., Montañez, I.P., Fullagar, P.D., and Valley, J.W., 1993, Alleghenian Regional Diagenesis: A Response to the Migration of Modified Metamorphic Fluids Derived from beneath the Blue Ridge-Piedmont Thrust Sheet: The Journal of Geology, v. 100, no. 3, p. 339–352, doi: 10.1086/629636.

Schleicher, A.M., van der Pluijm, B.A., Warr, L.N., and Solum, J.G., 2007, Electron microscopy of clay minerals in mudrocks from the san andreas Fault observatory at depth (SAFOD) (H. Ito, J. Behrmann, S. H. Hickman, H. Tobin, & G. Kimura, Eds.): Scientific Drilling, Special Issue no. 1, p. 68–70, doi: 10.2204/iodp.sd.s01.33.2007.

Schleicher, A.M., van der Pluijm, B.A., and Warr, L.N., 2010, Nanocoatings of clay and creep of the San Andreas fault at Parkfield, California: Geology, v. 38, no. 7, p. 667–670, doi: 10.1130/G31091.1.

Seal, R.R., and Rye, R.O., 1993, Stable isotope study of fluid inclusions in fluorite from Idaho: implications for continental climates during the Eocene: Geology, v. 21, no. 3, p. 219–222, doi: 10.1130/0091-7613(1993)021<0219:SISOFI>2.3.CO;2.

Selverstone, J., Axen, G., Luther, A., 2012. Fault localization controlled by fluid infiltration into mylonites: Formation and strength of low-angle normal faults in the midcrustal brittle-ductile transition. J. Geophysical Research B 117, doi: 10.1029/2012JB009171.

Sharp, Z., 2005, Principles of Stable Isotope Geochemistry: New York, Prentice Hall, 344 p.

Sharp, Z., Atudorei, V., and Durakiewicz, T., 2001, A rapid method for determination of hydrogen and oxygen isotope ratios from water and hydrous minerals: Chemical Geology, v. 178, p. 197–210.

Sheppard, S.M.F., 1986, Characterization and isotopic variations in natural waters: Reviews in Mineralogy and Geochemistry, v. 16, p. 165–183.

Sheppard, S., and Gilg, H., 1996, Stable isotope geochemistry of clay minerals. Clay Minerals 31, p. 1-24.

Sibson, R.H., 1977. Fault rocks and fault mechanisms. J. Geological Society of London 133, p. 191-213.

Sibson, R.H., 1987, Earthquake rupturing as a mineralizing agent in hydrothermal systems: Geology, v. 15, p. 701-704, doi: 10.1130/0091-7613(1987)15<701:ERAAMA>2.0.CO;2.

Sibson, R.H., 1992, Fault-valve behavior and the hydrostatic-lithostatic fluid pressure interface: Earth Science Reviews, v. 32, p. 141–144, doi: 10.1016/0012-8252(92)90019-P.

Sibson, R.H., 1994, Crustal stress, faulting and fluid flow in Parnell, J., ed., Geofluids: Origin, Migration and Evolution of Fluids in Sedimentary Basins,: Geological Society, London, Special Publications, v. 78, no. 1, p. 69–84, doi: 10.1144/GSL.SP.1994.078.01.07.

Sibson, R.H., 1996, Structural permeability of fluid-driven fault-fracture meshes: Journal of Structural Geology, v. 18, no. 8, p. 1031–1042, doi: 10.1016/0191-8141(96)00032-6.

Sleep, N.H., and Blanpied, M.L., 1992, Creep, compaction and the weak rheology of major faults: Nature, v. 359, no. 6397, p. 687–692, doi: 10.1038/359687a0.

Smith, B., Reynolds, S., Day, H., Bodnar, R., 1991. Deep-seated fluid involvement in ductile-brittle deformation and mineralization, South Mountains metamorphic core complex, Arizona. Geol. Soc. Amer Bull. 103, p. 559-569.

Smith, C.N., Kesler, S.E., Klaue, B., and Blum, J.D., 2005, Mercury isotope fractionation in fossil hydrothermal systems: Geology, v. 33, no. 10, p. 825–4, doi: 10.1130/G21863.1.

Smith, C.N., Kesler, S.E., Blum, J.D., and Rytuba, J.J., 2008, Isotope geochemistry of mercury in source rocks, mineral deposits and spring deposits of the California Coast Ranges, USA: Earth and Planetary Science Letters, v. 269, no. 3-4, p. 399–407, doi: 10.1016/j.epsl.2008.02.029.

Sobel, E.R., and Strecker, M.R., 2003, Uplift, exhumation and precipitation: tectonic and climatic control of Late Cenozoic landscape evolution in the northern Sierras Pampeanas, Argentina: Basin Research, v. 15, no. 4, p. 431–451, doi: 10.1046/j.1365-2117.2003.00214.x.

Solum, J.G, 2005. Clay neomineralization in fault zones: extracting information of fault properties and timing. Unpublished PhD thesis, University of Michigan.

Solum, J.G, van der Pluijm, B. and Peacor, D., 2005. Neocrystallization, fabrics and age of clay minerals from an exposure of the Moab Fault, Utah. J. Structural Geology 27, pp. 1563-1576.

Solum, J.G., Hickman, S.H., Lockner, D.A., Moore, D.E., van der Pluijm, B.A., Schleicher, A.M., and Evans, J.P., 2006, Mineralogical characterization of protolith and fault rocks from the SAFOD Main Hole: Geophysical Research Letters, v. 33, no. 21, p. L21314, doi: 10.1029/2006GL027285.

Solum, J.G., Hickman, S.H., Lockner, D.A., Tembe, S., Evans, J.P., Draper, S.D., Barton, D.C., Kirschner, D.L., Chester, J.S., Chester, F.M., van der Pluijm, B.A., Schleicher, A.M., Moore, D.E., Morrow, C., et al., 2007, San Andreas fault zone mineralogy, geochemistry, and physical properties from SAFOD cuttings and core (H. Ito, J. Behrmann, S. H. Hickman, H. Tobin, & G. Kimura, Eds.): Scientific Drilling, Special Issue no. 1, p. 64–67, doi: 10.2204/iodp.sd.s01.34.2007.

Solum, J.G. and van der Pluijm, B.A., 2007, Reconstructing the Snake River–Hoback River Canyon section of the Wyoming thrust belt through direct dating of clay-rich fault rocks, in Sears, J.W., Harms, T.A., Evenchick, C.A., eds., Whence the Mountains? Inquiries into the Evolution of Orogenic Systems, a Volume in Honor of Raymond A. Price: Geological Society of America Special Paper 433, pp. 183–196, doi: 10.1130/2007.2433(09).

Spencer, J., Welty, J., 1986, Possible controls of base-metal and precious-metal mineralization associated with Tertiary detachment faults in the lower Colorado River Trough, Arizona and California. Geology v. 14, p. 195-198.

Spicuzza, M. Valley, J., McConnell, V., 1998, Oxygen isotope analysis of whole rock via laser fluorination: an air-lock approach. GSA Abst. w. Prog. V. 30:80.

Stamatakos, J., Hirt, A.M., and Lowrie, W., 1996, The age and timing of folding in the central Appalachians from paleomagnetic results: Geological Society of America Bulletin, v. 108, no. 7, p. 815–829.

Sutter, J.F., 1988, Innovative approaches to dating of igneous events in the early Mesozoic basins of the eastern United States, *in* Froelich, A.J. and Robinson, G.R.J. eds., Studies of the Early Mesozoic Basins of the Eastern United States, USGS Bulletin, no. 1776, p. 196–200.

Suzouki, T., Epstein, S., 1976. Hydrogen isotope fractionation between OH-bearing minerals and water. Geochim. et Cosm. Acta 40, p. 1229-1240.

Swanson, E., Wernicke B., Eiler, J., Losh, S., 2012, Temperatures and fluids on faults based on carbonate clumped isotope thermometry. Amer. J. Sci. v. 312, p. 1-21.

Sweetkind, D., Dickerson, R., Blakely, R., Denning, P., 2001. Interpretive geologic cross sections for the Death Valley regional flow system and surrounding areas, Nevada and California. USGS Miscellaneous field Studies Map MF-2370.

Symons, D.T.A., and Cioppa, M.T., 2002, Conodont CAI and magnetic mineral unblocking temperatures: Implications for the Western Canada Sedimentary Basin: Physics and Chemistry of the Earth, v. 27, no. 25-31, p. 1189–1193, doi: 10.1016/S1474-7065(02)00129-8.

Taylor, H.P., 1974, The application of oxygen and hydrogen isotope studies to problems of hydrothermal alteration and ore deposition: Economic Geology, v. 69, p. 843–883.

Templeton, A.S., Chamberlain, C.P, Koons, P.O and Craw, D., 1998, Stable isotopic evidence for mixing between metamorphic fluids and surface-derived waters during recent uplift of the Southern Alps, New Zealand: Earth and Planetary Science Letters, v. 154, p. 73–92.

Tobin, T.S., Wilson, G.P., Eiler, J.M., and Hartman, J.H., 2014, Environmental change across a terrestrial Cretaceous-Paleogene boundary section in eastern Montana, USA, constrained by carbonate clumped isotope paleothermometry: Geology, v. 42, no. 4, p. 351–354, doi: 10.1130/G35262.1.

Toby, B.H., 2006, R factors in Rietveld analysis: How good is good enough?: Powder Diffraction, v. 21, no. 1, p. 67–70, doi: 10.1154/1.2179804.

Tonguç Uysal, I., Mutlu, H., Altunel, E., Karabacak, V., 2006. Clay mineralogical and isotopic (K-Ar, $\delta^{18}O$, δD) constraints on the evolution of the North Anatolian Fault Zone, Turkey. Earth and Planetary Science Letters 243, p. 181-194

Travé, A., Labaume, P., Calvet, F., and Soler, A., 1997, Sediment dewatering and pore fluid migration along thrust faults in a foreland basin inferred from isotopic and elemental geochemical analyses (Eocene southern Pyrenees, Spain): Tectonophysics, v. 282, p. 375–398.

Travé, A., Labaume, P., and Verges, J., 2007, Fluid systems in foreland fold-and-thrust belts: An overview from the Southern Pyrenees. *in*: Thrust belts and foreland basins: from fold kinematics to hydrocarbon systems. Eds. Lacombe, O., Lave, J., Roure, F., Verges, J., Springer.

Ufer, K., Kleeberg, R., Bergmann, J., and Dohrmann, R., 2012, Rietveld Refinement of Disordered Illite-smectite Mixed-Layer Structures by a Recursive Algorithm. I: One-Dimensional Patterns: Clays and Clay Minerals, v. 60, no. 5, p. 507–534, doi: 10.1346/CCMN.2012.0600507.

Ufer, K., and Kleeberg, R., 2015, Parametric Rietveld refinement of coexisting disordered clay minerals: Clay Minerals, v. 50, no. 3, p. 287–296, doi: 10.1180/claymin.2015.050.3.03.

Uysal, I.T., Mutlu, H., Altunel, E., Karabacak, V., and Golding, S., 2006, Clay mineralogical and isotopic (K–Ar, δ18O, δD) constraints on the evolution of the North Anatolian Fault Zone, Turkey: Earth and Planetary Science Letters, v. 243, no. 1-2, p. 181–194, doi: 10.1016/j.epsl.2005.12.025.

Valley, J. W., Kitchen, N. E., Kohn, M. J., Niendorf, C. R., Spicuzza, M. J., 1995, UWG-2, A Garnet Standard for Oxygen Isotope Ratio: Strategies for High Precision and Accuracy with Laser Heating. Geochim. Cosmochim. Acta v. 59, p. 5223-5231.

Vandeginste, V., Swennen, R., Allaeys, M., Ellam, R.M., Osadetz, K., and Roure, F., 2012, Challenges of structural diagenesis in foreland fold-and-thrust belts: A case study on paleofluid flow in the Canadian Rocky Mountains West of Calgary: Marine and Petroleum Geology, v. 35, no. 1, p. 235–251, doi: 10.1016/j.marpetgeo.2012.02.014.

van der Pluijm, B.A., Hall, C.M., Vrolijk, P., Pevear, D.R., and Covey, M.C., 2001. The dating of shallow faults in the Earth's crust: Nature, v. 412, p. 172-174.

van der Pluijm, B.A., Vrolijk, P., Pevear, D.R., Hall, C.M., and Solum, J.G., 2006, Fault dating in the Canadian Rocky Mountains: Evidence for late Cretaceous and early Eocene orogenic pulses: Geology, v. 34, no. 10, p. 837–5, doi: 10.1130/G22610.1.

van der Pluijm, B.A., and Fitz-Diaz, E., 2013, Fold dating: A new Ar/Ar illite dating application to constrain the age of deformation in shallow crustal rocks: Journal of Structural Geology, v. 54, p. 174–179, doi: 10.1016/j.jsg.2013.05.011.

van der Pluijm, B., and Hall, C., 2015, Fault Zone—Thermochronology, in Rink, J.W., and Thompson, J.W., eds., Encyclopedia of Scientific Dating Methods: Dordrecht, Springer, 978 p., doi: 10 .1007 /978 -94 -007 -6304 -3.

Van der Voo, R., 1979, Age of Alleghenian folding in the Central Appalachians, v. 7, no. 6., p. 297–298, doi: 10.1130/0091-7613(1979)7<297:AOTAFI>2.0.CO;2.

Vannucchi, P., Maltman, A., Bettelli, G., and Clennell, B., 2003, On the nature of scaly fabric and scaly clay: Journal of Structural Geology, v. 25, no. 5, p. 673–688, doi: 10.1016/S0191-8141(02)00066-4.

Verdel, C., van der Pluijm, B.A., and Niemi, N., 2012, Variation of illite/muscovite 40Ar/39Ar age spectra during progressive low-grade metamorphism: an example from the US Cordillera: Contributions to Mineralogy and Petrology, v. 164, no. 3, p. 521–536, doi: 10.1007/s00410-012-0751-7.

von Gosen, W., 1997, Early Paleozoic and Andean structural evolution in the Río Jáchal section of the Argentine Precordillera: Journal of South American Earth Sciences, v. 10, no. 5-6, p. 361-388.

Vrolijk, P., and van der Pluijm, B., 1999, Clay gouge: Journal of Structural Geology, v. 21, p. 1039-1048.

Walther, J.V., and Orville, P.M., 1982, Volatile production and transport in regional metamorphism: Contributions to Mineralogy and Petrology, v. 79, no. 3, p. 252–257, doi: 10.1007/BF00371516.

Walther, J.V., and Wood, B.J., 1984, Rate and mechanism in prograde metamorphism: Contributions to Mineralogy and Petrology, v. 88, no. 3, p. 246–259, doi: 10.1007/BF00380169.

Wang, Y., Zwingmann, H., Zhou, L., Lo, C.-H., Viola, G., and Hao, J., 2016, Direct dating of folding events by 40Ar/39Ar analysis of synkinematic muscovite from flexural-slip planes: Journal of Structural Geology, v. 83, p. 46–59, doi: 10.1016/j.jsg.2015.12.003.

Wanner, C., Peiffer, L., Sonnenthal, E., Spycher, N., Iovenitti, J., and Kennedy, B.M., 2014, Reactive transport modeling of the Dixie Valley geothermal area: Insights on flow and geothermometry: Geothermics, v. 51, p. 130–141, doi: 10.1016 /j.geothermics.2013.12.003.

Warr, L.N., Wojatschke, J., Carpenter, B.M., Marone, C., Schleicher, A.M., and van der Pluijm, B.A., 2014, A "slice-and-view" (FIB-SEM) study of clay gouge from the SAFOD creeping section of the San Andreas Fault at ~2.7 km depth: Journal of Structural Geology, v. 69, p. 234–244, doi: 10.1016/j.jsg.2014.10.006.

Weatherley, D.K., and Henley, R.W., 2013, Flash vaporization during earthquakes evidenced by gold deposits: Nature Geoscience, v. 6, no. 4, p. 294–298, doi: 10.1038/ngeo1759.

Wernicke, B., 1981, Low-angle normal faults in the Basin and Range province: Nappe tectonics in an extensional orogen. Nature v. 291, p. 645-648.

Whisonant, R.C. and Schultz, A.P., 1986, Appalachian Valley and Ridge to Appalachian Plateau transition zone in southwestern Virginia and eastern West Virginia; structure and sedimentology: *in* Neathery, T.L., ed., Centennial Field Guide Volume 6, Southeastern section of the Geological Society of America, Geological Society of America, Boulder, Colorado, p. 113□118.

Whitney, G., Northrup, H., 1987. Diagenesis and fluid flow in the San Juan Basin, New Mexico: Regional zonation in the mineralogy and stable isotope composition of clay minerals in sandstone. American J. Science 287, p. 353-382.

Wiederhold, J.G., Cramer, C.J., Daniel, K., Infante, I., Bourdon, B., and Kretzschmar, R., 2010, Equilibrium Mercury Isotope Fractionation between Dissolved Hg(II) Species and Thiol-Bound Hg: Environmental Science & Technology, v. 44, no. 11, p. 4191–4197, doi: 10.1021/es100205t.

Wickham, S., Peters, M., 1990. An oxygen isotope discontinuity in high-grade rocks of the East Humboldt Range, Nevada. Nature 345, p. 150-153.

Wickham, S., Peters, M., Fricke, H., O'Neil, J., 1993. Identification of magmatic and meteoric fluid sources and upward- and downward-moving infiltration fronts in a metamorphic core complex. Geology 21, p. 81-84.

Wilson, T.H., 1989, Geophysical Studies of Large Blind Thrust, Valley and Ridge Province, Central Appalachians: AAPG Bulletin, v. 73, no. 3, p. 276–288.

Wilson, T.H., and Shumaker, R.C, 1992, Broad Top Thrust Sheet: An Extensive Blind Thrust in the Central Appalachains: AAPG Bulletin, v. 76, no. 3, .p. 1310-1324.

Wiltschko, D., and Dorr, J.A., 1983. Timing of deformation in overthrust belt and foreland of Idaho, Wyoming and Utah: AAPG Bulletin, v. 67, p. 1304–1322, doi: 10.1306/03B5B740-16D1-11D7-8645000102C1865D.

Wiltschko, D.V., Lambert, G.R., and Lamb, W., 2009, Conditions during syntectonic vein formation in the footwall of the Absaroka Thrust Fault, Idaho–Wyoming–Utah fold and thrust belt: Journal of Structural Geology, v. 31, no. 9, p. 1039–1057, doi: 10.1016/j.jsg.2009.03.009.

Wintsch, R.P., Sutter, J.F., Kunk, M.J., Aleinikoff, J.N., and Dorais, M.J., 1992, Contrasting P-T-t paths: Thermochronologic evidence for a Late Paleozoic final assembly of the Avalon Composite Terrane in the New England Appalachians: Tectonics, v. 11, no. 3, p. 672–689, doi: 10.1029/91TC02904.

Yangfen, J., Zonghua, W., Chunsheng, S., Jiazhen, W., and Hongren, Z., 1989, Earthquake prediction through the observation and measurement of mercury content variation in water: Journal of Geochemical Exploration, v. 33, no. 1-3, p. 195–202, doi: 10.1016/0375-6742(89)90029-0.

Yardley, B.W.D., and Bodnar, R.J., 2014, Fluids in the Continental Crust: Geochemical Perspectives, v. 3, no. 1, p. 1-127.

Yin, R., Feng, X., and Shi, W., 2010, Application of the stable-isotope system to the study of sources and fate of Hg in the environment: A review: Applied Geochemistry, v. 25, no. 10, p. 1467–1477, doi: 10.1016/j.apgeochem.2010.07.007.

Yonkee, W.A., Parry, W.T., Bruhn, R.L., Cashman, H., 1989, Thermal models of thrust faulting: Constraints from fluid-inclusion observations, Willard thrust sheet, Idaho–Utah–Wyoming thrust belt: Geological Society of America Bulletin, v. 101, p. 304–313, doi: 10.1130/0016-7606(1989)101<0304:TMOTFC>2.3.CO;2.

Yonkee, W.A., and Weil, A.B., 2015, Tectonic evolution of the Sevier and Laramide belts within the North American Cordillera orogenic system: Earth Science Reviews, v. 150, no. C, p. 531–593, doi: 10.1016/j.earscirev.2015.08.001.

York, D., 1968, Least squares fitting of a straight line with correlated errors: Earth and Planetary Science Letters, v. 5, p., 320-324.

Zachos, J., Pagani, M., Sloan, L., Thomas, E., and Billups, K., 2001, Trends, rhythms, and aberrations in global climate 65 Ma to present: Science, v. 292, no. 5517, p. 686-693

Zapata, T.R., and Allmendinger, R.W., 1996, Thrust front zone of the Precordillera, Argentina: A thick-skinned triangle zone: AAPG Bulletin, v. 80, no. 3, p. 359-381.

Zhang, G; Germaine, J.T., Martin, R.T, and Whittle, A.J., 2003, A simple sample-mounting method for random powder x-ray diffraction: Clays and Clay Minerals, v. 51, no. 2, p. 218–225, doi: 10.1346/CCMN.2003.0510212.

Zhang, L., Liu, Y., Guo, L., Yang, D., Fang, Z., Chen, T., and Ren, H., 2014, Isotope geochemistry of mercury and its relation to earthquake in the Wenchuan Earthquake Fault Scientific Drilling Project Hole-1 (WFSD-1): Tectonophysics, v. 619-620, p. 79–85, doi: 10.1016/j.tecto.2013.08.025.

Zheng, W., Foucher, D., and Hintelmann, H., 2007, Mercury isotope fractionation during volatilization of Hg(0) from solution into the gas phase: Journal of Analytical Atomic Spectrometry, v. 22, no. 9, p. 1097–1104, doi: 10.1039/B705677J.

Zoback, M.D., Hickman, S.H., Ellsworth, W., the SAFOD Science Team, 2011, Scientific Drilling Into the San Andreas Fault Zone: An Overview of SAFOD's First Five Years (H. C. Larsen & U. Harms, Eds.): Scientific Drilling, no. 11, p. 14–28, doi: 10.2204/iodp.sd.11.02.2011.

Zoback, M.D., and Townend, J., 2001, Implications of hydrostatic pore pressures and high crustal strength for the deformation of intraplate lithosphere: Tectonophysics, v. 336, no. 1-4, p. 19–30, doi: 10.1016/S0040-1951(01)00091-9.

Zwingmann, H., Clauer, N., and Gaupp, R., 1999, Structure-related geochemical (REE) and isotopic (K-Ar, Rb-Sr, $\delta^{18}O$) characteristics of clay minerals from Rotliegend sandstone reservoirs (Permian, northern Germany): Geochimica et Cosmochimica Acta, v. 63, no. 18, p. 2805–2823.